

# Single-Source-Precursor Containing Derived Transition Metal Compounds Carbon Hybrid Nanocomposites for Electrochemical Applications

Zur Erlangung des akademischen Grades Doktor der Ingenieurwissenschaften (Dr.-Ing.)

Genehmigte Dissertation von M.Sc. Yongchao Chen

Erstgutachter: Prof. Dr. Ralf Riedel

Zweitgutachter: Prof. Dr. Jan P. Hofmann

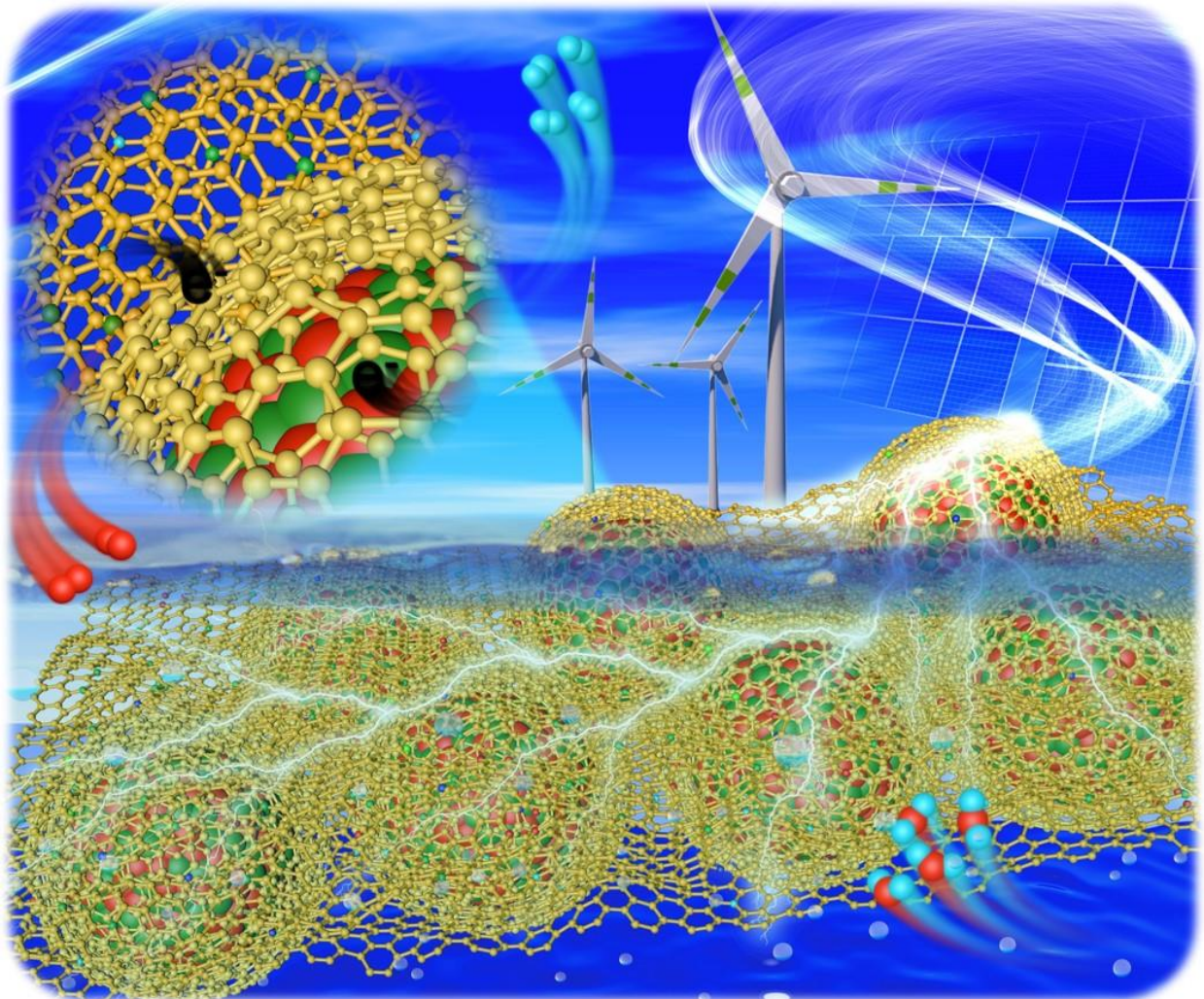
TU Darmstadt, FB 11 - Material- und Geowissenschaften

Fachgebiet Disperse Feststoffe

Darmstadt 2023



TECHNISCHE  
UNIVERSITÄT  
DARMSTADT



Single-Source-Precursor Containing Derived Transition Metal Compounds Carbon Hybrid  
Nanocomposites for Electrochemical Applications

Genehmigte kumulative Dissertation von M.Sc. Yongchao Chen aus Liaoning, China

Jahr der Veröffentlichung der Dissertation auf TUprints: 2023

URN: urn:nbn:de:tuda-tuprints-246244

Tag der Einreichung: 26 July 2023

Tag der mündlichen Prüfung: 18 September 2023

Veröffentlicht unter CC BY-NC 4.0 International

<https://creativecommons.org/licenses>

The chapters 3.1, 3.2 and 3.3 are copyright to Wiley and excluded from the Open Access licence

---

---

## Erklärung zur Dissertation

---

### **§8 Abs. 1 lit. c PromO**

Ich versichere hiermit, dass die elektronische Version meiner Dissertation mit der schriftlichen Version übereinstimmt.

### **§8 Abs. 1 lit. d PromO**

Ich versichere hiermit, dass zu einem vorherigen Zeitpunkt noch keine Promotion versucht wurde. In diesem Fall sind nähere Angaben über Zeitpunkt, Hochschule, Dissertationsthema und Ergebnis dieses Versuchs mitzuteilen.

### **§9 Abs. 1 PromO**

Ich versichere hiermit, dass die vorliegende Dissertation selbstständig und nur unter Verwendung der angegebenen Quellen verfasst wurde.

### **§9 Abs. 2 PromO**

Die Arbeit hat bisher noch nicht zu Prüfungszwecken gedient.

Darmstadt, den



---

(Yongchao Chen)

---



---

The present cumulative dissertation summarizes the essential scientific findings in the following peer-reviewed articles. Article reprints are enclosed in the Chapter *Publications* at the end of this dissertation.

- (I) Chen, Y., Tian, C., Jiang, T., Maheu, C., Hofmann, J. P., Molina-Luna, L., Riedel, R. & Yu, Z. Single-Source-Precursor Derived Transition Metal Alloys Embedded in Nitrogen-Doped Porous Carbons as Efficient Oxygen Evolution Electrocatalysts. *ChemPlusChem* 87, e202200338 (2022).
  - (II) Chen, Y., Jiang, T., Tian, C., Zhan, Y., Kempf, A., Molina-Luna, L., Hofmann, J. P., Riedel, R. & Yu, Z. Single-Source-Precursor Derived Binary FeNi Phosphide Nanoparticles Encapsulated in N, P Co-Doped Carbon as Electrocatalyst for HER and OER. *Energy Technology*, 2300233 (2023).
  - (III) Chen, Y., Jiang, T., Tian, C., Zhan, Y., Adabifiroozjaei, E., Kempf, A., Molina-Luna, L., Hofmann, J. P., Riedel, R. & Yu, Z. Molybdenum Phosphide Quantum Dots Encapsulated by P/N-Doped Carbon for Hydrogen Evolution Reaction in Acid and Alkaline. *ChemSusChem*, e202300479 (2023).
-



---

---

## Acknowledgments

---

Completing a PhD is no small feat, and I am grateful to many individuals who have supported me throughout my academic journey. Their guidance, encouragement, and support have been invaluable, and I would not have been able to achieve this milestone without them.

First and foremost, I would like to express my deepest appreciation to my first professor, Prof. Ralf Riedel, and my second professors, Prof. Jan Philipp Hofmann who have provided mentorship, rigorous feedback and constructive criticism have been critical to my success, and I am grateful for their support and guidance throughout my PhD journey. Their vast knowledge and expertise in their respective fields have been instrumental in shaping my PhD research. And I am grateful for the help and revision provided by Prof. Zhaoju Yu to support my research.

I would also like to express my sincere thanks to Prof. Leopoldo Molina-Luna who has collaborated with me on various aspects of my research. Their contributions have been essential to the success of my work, and I am grateful for their expertise, support, and guidance. And I would like to extend my thanks to other co-authors, Tianshu Jiang, Chuanmu Tian, Clément Maheu, Ying Zhan, and Alexander Kempf. I am grateful for their expertise, support and help to gain a deeper understanding and address the challenges.

I would like to take this opportunity to express my deepest gratitude to my former and current colleagues, Ying Zhan, Samuel Aeneas Kredel, Emmanuel III Ricohermoso, Wei Li, Alexander Kempf, Fangmu Qu, Dario De Carolis, and Honghong Tian, for the invaluable support and camaraderie that they have provided me throughout my PhD journey. It has been an absolute privilege to collaborate with them as a part of the Disperse Feststoffe group.

I am honored to have had the opportunity to be a part of such an exceptional group of individuals during my time in Darmstadt. To my friends Chen Shen, Mian Dai, Tianshu Jiang, Fei Liang, Ying Zhan, Wei Li, Tianshu Li, Kun Hu and Yixuan Zhang, I am grateful for the bond that we have shared and for the memories that we have created together. I feel privileged to have had such wonderful friends during my PhD study, and I will always cherish the time that we spent together. Thank you for making my studying in Darmstadt a truly unforgettable experience.

I am deeply appreciative of the support and encouragement that my friends from my homeland, Dongwei Yang, Yang Chen and Weiyue Kong, have shown me throughout my academic journey. Their unwavering belief in my abilities has been a constant source of motivation and inspiration. I feel fortunate to have such wonderful friends.

I would also like to extend my appreciation to all my teammates of Maida United Football Club and

---

---

---

Team Darmstadtium. Joining the football teams was a truly unforgettable experience that brought me incomparable joy and fulfillment that can only be found in the beautiful game of football. Their encouragement and support were not only indispensable in helping me to score goals but also in maintaining a healthy work-life balance. I feel grateful to have been a part of such supportive and welcoming teams.

Finally, I would like to express my heartfelt gratitude to my parents, Mr. Junwei Chen and Ms. Yanzhi Li, for their unwavering love, support, and encouragement throughout my past days. Their belief in me has been a constant source of inspiration for me to pursue my dreams. I am also deeply grateful to my elder sister, Zhichao Chen, for her unwavering support and guidance, which is instrumental in shaping my dream and personal growth. I am also thankful to my brother-in-law, Markus Maron, whose advice and help have been invaluable to me at the beginning of my PhD study. In addition, I would like to thank my two nephews, Leon Maron and Levi Maron, for their constant love and joy. Their presence during my study has brought me immense happiness and motivation. Lastly, I extend my thanks to my twin sister, Yongjie Chen, whose companionship have been a constant in my life since birth. Her encouragement, accompany, and feedback have been instrumental in my life and helping me to continuously improve myself. In addition, I would like to thank my girlfriend, Zehui Guo, for her constant support and encouragement during my studies. I would also like to wish you a lot of success in your upcoming PhD study.

This dissertation is dedicated to my beloved parents and sisters!

Yongchao Chen (陈永超)

Darmstadt, July 2023

---



---

---

## Abstract

---

Advanced catalysts for the electrocatalytic hydrogen evolution reaction (HER) and oxygen evolution reaction (OER) are required in the future to further develop an efficient and up-scalable water splitting process. Among all the potential candidates, carbon-supported transition metal-based nanomaterials are of great interest due to their low cost, high durability, and promising functional performance.

This dissertation presents an innovative and cost-effective approach to synthesize carbon shell-encapsulated transition metal alloys or phosphide nanoparticles supported on *in-situ* formed defective N-doped carbon/carbon nanotube hybrids, which are derived from novel single-source-precursors (SSPs). The precursor is synthesized by a facile one-pot reaction using cheap and environmentally friendly carbon and phosphorus sources. The obtained core-shell structured hybrids perform as highly active and durable electrocatalysts for HER and/or OER, benefiting from the following common features: (1) A synergistic electronic effect among transition metal compounds, heteroatom-doped carbon, and entangled carbon nanotubes. (2) Promotion of electrolyte penetration towards the active sites through the porous structure of the formed mesoporous carbon clusters. (3) The unique core-shell nanostructure of the hybrid material effectively curbs the degradation of the electrocatalyst by protecting the active nanoparticles from harsh electrolyte.

The present studies propose various strategies to enhance the electrocatalytic properties, utilizing both morphology-controlled and composition-controlled methods. Additionally, the studies also focus on the relationship between structure and property, which ultimately determines the electrocatalytic activity for the HER and OER. These findings may offer valuable insights for future applications in the field of electrochemical water splitting. Furthermore, the thesis aims to provide a cost-effective and straightforward approach for synthesizing hybrid materials comprised of transition metal compounds and carbon, with the goal of facilitating their potential utilization in energy storage and conversion applications.

---

---

---

## Zusammenfassung

---

Smarte Katalysatoren für die elektrokatalytische Wasserstoff-Evolution (HER) und Sauerstoff-Evolution (OER) sind in der Zukunft erforderlich, um einen effizienten und skalierbaren Wasserspaltungsprozess weiterzuentwickeln. Unter allen potenziellen Kandidaten sind kohlenstoffgestützte Übergangsmetall-basierte Nanomaterialien von großem Interesse aufgrund ihrer geringen Kosten, hohen Haltbarkeit und vielversprechenden funktionalen Eigenschaften.

Diese Dissertation präsentiert einen innovativen und kosteneffektiven Ansatz zur Synthese von kohlenstoffbeschichteten Übergangsmetall-Legierungen oder Phosphid-Nanopartikeln, die auf *in-situ* gebildeten defekten N-dotierten Kohlenstoff/Kohlenstoff-Nanoröhren-Hybriden unterstützt werden, die aus neuartigen Einkomponentenvorstufen (SSP) abgeleitet sind. Der Vorläufer wird durch eine einfache Eintopfreaktion unter Verwendung von günstigen und umweltfreundlichen Kohlenstoff- und Phosphorquellen hergestellt. Die erhaltenen Kern-Schale-strukturierten Hybride fungieren als hochaktive und langlebige Elektrokatalysatoren für HER- und/oder OER-Prozesse und profitierten von folgenden gemeinsamen Merkmalen: (1) Ein synergistischer elektronischer Effekt zwischen Übergangsmetallverbindungen, Heteroatom-dotiertem Kohlenstoff und verwickelten Kohlenstoffnanoröhren. (2) Förderung der Elektrolyt-Penetration zu den aktiven Stellen aufgrund der ausgebildeten mesoporösen Kohlenstoffcluster. (3) Die einzigartige Kern-Schale-Nanostruktur des Hybridmaterials verhindert effektiv den Abbau des Elektrokatalysators durch Schutz der aktiven Nanopartikel vor dem reaktiven Elektrolyt.

Die vorliegenden Studien schlagen verschiedene Strategien zur Verbesserung der elektrokatalytischen Eigenschaften vor, die sowohl morphologiekontrollierte als auch zusammensetzungskontrollierte Methoden nutzen. Darüber hinaus konzentrierten sich die Studien auch auf die Beziehung zwischen Struktur und Eigenschaft, die letztendlich die elektrokatalytische Aktivität für den HER- und OER-Prozess bestimmt. Die gewonnenen Erkenntnisse bieten wertvolle Einblicke für zukünftige Anwendungen in der elektrochemischen Wasserspaltung. Darüber hinaus zielt die Arbeit darauf ab, einen kosteneffektiven und unkomplizierten Ansatz zur Synthese von Hybridmaterialien aus Übergangsmetallverbindungen und Kohlenstoff bereitzustellen, um deren potenzielle Verwendung im Bereich der Energiespeicherung und Energieumwandlung zu erleichtern.

---

---

---

## Table of Contents

---

List of Abbreviations .....	i
List of Symbols .....	iii
List of Figures .....	v
List of Tables .....	ix
1 Introduction .....	1
2 Fundamentals.....	5
2.1 Electrocatalysis of water splitting.....	5
2.1.1 Electrocatalysis reaction mechanism .....	5
2.1.2 Evaluation parameters for HER and OER catalyst .....	8
2.2 Transition metal compounds/carbon hybrids as electrocatalyst.....	11
2.2.1 Transition metal alloy/carbon hybrid.....	12
2.2.2 Transition metal phosphide/carbon hybrid.....	13
2.3 Transition metal compounds/carbon hybrids fabrication .....	14
2.3.1 Traditional synthesis methods.....	15
2.3.2 Single-source-precursor method .....	17
2.4 Strategies for improving performance .....	17
2.4.1 Nanostructure engineering .....	17
2.4.2 Intrinsic activity improvement.....	20
3 Results and Discussion .....	23
3.1 Single-source-precursor derived transition metal alloys embedded in nitrogen-doped porous carbons as efficient oxygen evolution electrocatalysts.....	23
3.2 Single-source-precursor derived Fe/Ni phosphide nanoparticles encapsulated in P/N-co-doped carbon as bifunctional electrocatalyst for hydrogen evolution reaction and oxygen evolution reaction.....	36
3.3 Single-source-precursor derived molybdenum phosphide quantum dots encapsulated by P/N-co-doped carbon as electrocatalyst for hydrogen evolution reaction in acid and alkaline electrolytes .....	52
4 Conclusions and Outlook.....	69
5 References .....	71
Curriculum Vitae.....	I
Publications .....	III

---



---

---

## List of Abbreviations

---

BET	Brunauer-Emmett-Teller
BJH	Barrett–Joyner–Halenda
CA	Chronoamperometry
CNTs	Carbon nanotubes
CP	Chronopotentiometry
CV	Cyclic voltammetry
CVD	Chemical vapor deposition
DFT	Density functional theory
ECSA	Electrochemical active surface area
EDS	Energy dispersive X-ray spectroscopy
EIS	Electrochemical impedance spectroscopy
FE	Faradaic efficiency
FTIR	Fourier-transform infrared spectroscopy
GC	Gas chromatography
HER	Hydrogen evolution reaction
HRTEM	High-resolution transmission electron microscopy
LSV	Linear scan voltammetry
MOFs	Metal organic frameworks

---

NLDFT	Non-local density functional theory
OER	Oxygen evolution reaction
PA	Phytic acid
PEI	Polyethylenimine
QDs	Quantum dots
RHE	Reversible hydrogen electrode
SEM	Scanning electron microscopy
SSA	Specific surface area
SSPs	Single-source-precursors
TA	Tannic acid
TEM	Transmission electron microscopy
TMA <sub>s</sub>	Transition metal alloys
TMC <sub>s</sub>	Transition metal compounds
TMPI	Transition metal phosphate
TMP <sub>s</sub>	Transition metal phosphides
TMI <sub>s</sub>	Transition metal ions
XPS	X-ray photoelectron spectroscopy
XRD	X-ray diffraction

---

---

## List of Symbols

---

$\Delta G$	Gibbs free energy
$E_{op}$	Operating voltage
$E_a$	Overpotential of the anode
$E_c$	Overpotential of the cathode
$E_r$	Excess potential produced from electrolyte diffusion
$E$	Theoretical thermodynamic voltage for water splitting
*	Adsorbed active site
$\Delta G_{H^*}$	Hydrogen adsorption free energy
$R_s$	Solution resistance
$R_{ct}$	Charge transfer resistance
$E_p$	$iR$ -corrected potential
$i$	Measured current
$R$	Uncompensated resistance
$E_{RHE}$	Measured potential with respect to reversible hydrogen electrode
$\eta$	Overpotential
$j$	Current density
$b$	Tafel slope
$a$	Tafel constant

---

---

$Z_{re}$	Real impedance
$Z_{im}$	Imaginary impedance
$C_{dl}$	Double layer capacitance
$\Delta j$	Differential current density
$\eta_{HER}$	HER overpotential at a current density of $-10 \text{ mA cm}^{-2}$
$\eta_{OER}$	OER overpotential at a current density of $10 \text{ mA cm}^{-2}$
$i_0$	Polarized current
$\Delta\rho$	Differential charge density
$\Delta E$	Chemisorption energies



---

---

## List of Figures

---

Figure 2.1 (a) Schematic description of the energy diagram for the water splitting process and (b) illustration of a water splitting electrolyser cell. ....	5
Figure 2.2 Schematic illustration of the (a) HER and (b) OER mechanism in both acidic and alkaline media. ....	7
Figure 2.3 The illustrations of (a) the evaluation parameters of electrocatalysts, including overpotential and Tafel slope, and (b) Nyquist representation of electrochemical impedance spectroscopy. ....	8
Figure 2.4 Nanostructure choices of carbon species and potentially coupled TMCs as electrocatalysts for water splitting.....	12
Figure 2.5 Different TMCs/carbon hybrids fabrication method.....	15
Figure 2.6 Schematic illustration of synthetic route of the precursor and TMCs/carbon hybrid via single-source-precursors approach.....	17
Figure 2.7 (a) Gibbs free energy ( $\Delta G$ ) profile of the HER on various catalysts, (b) volcano plot of the polarized current ( $i_0$ ) versus $\Delta G(H^*)$ for CoNi cluster, CoNi@C, and N-doped graphene shell, and (c) redistribution of the electron densities after the CoNi clusters have covered by one to three layers of graphene. Adapted from Ref. [41] .....	18
Figure 2.8 Scheme of different synthesis methods of porous materials. ....	19
Figure 2.9 (a) $\Delta G_{H^*}$ diagram and chemisorption energies of $OH^*$ ( $\Delta E_{OH^*}$ ) of different catalyst configurations, (b) free energy diagram of the water dissociation step (inset: the atomic configurations of different states of pyridinic-N-MoP), and (c) the charge density differences in pyridinic-, pyrrolic- and graphitic-N-MoP interfaces, yellow and cyan regions represent electron accumulation and depletion, respectively. Adapted from Ref. [40].....	21
Figure 2.10 Schematic illustration of promotion effects originating from heterostructure engineering. ....	22
Figure 3.1 Schematic illustration of the synthetic route of the precursor and carbon shell encapsulated FeNi alloy nanoparticles supported on <i>in-situ</i> formed N-doped graphene/carbon nanotube hybrid. .	24
Figure 3.2 (a) Raman spectrum and (b) FT-IR spectra of FeCo@NC precursors, TA, and PEI. ....	25
Figure 3.3 XRD patterns of different synthesized metallic core-shell compounds.....	25
Figure 3.4 XRD patterns of the FeCo@NC precursor carbonized under different temperatures. ....	26
Figure 3.5 (a) Low-magnification FE-SEM images, (b) high-magnification FE-SEM image of sample FeNi@NC-900, (c-g) SEM-EDS images, and (h) EDS spectrum of sample FeNi@NC-900. ....	27
Figure 3.6 TEM and HRTEM images of sample FeNi@NC-900. ....	28
Figure 3.7 (a) Raman spectra of samples FeCo@NC-900, FeNi@NC-900 and CoNi@NC-900, and (b) the peaks fitting plot of FeNi@NC-900. ....	29
Figure 3.8 XPS data for sample FeNi@NC-900: (a) Survey spectrum, (b) C 1s, (c) N 1s, (d) Ni2p, and (e)	

Fe 2p region scans. ....	30
Figure 3.9 Nitrogen physisorption data: (a) isotherms and (b) pore size distribution of different samples. ....	30
Figure 3.10 The OER performance of the synthesized core-shell samples including (a) polarization curves and (b) Tafel plots. ....	31
Figure 3.11 (a) OER EIS spectra of different samples (recorded at 1.56 V vs. RHE) and (b) impedance spectra in the higher frequency range (Color code is same in both plots). ....	32
Figure 3.12 (a) Plots of the current density versus the scan rate of samples FeCo@NC-900, FeCo@NC-900 and CoNi@NC-900, and (b) Polarization curves before and after continuous 1000 CV cycles, the inset shows the chronoamperometric curve for sample FeNi@NC-900 at constant potentials. ....	33
Figure 3.13 Raman peaks fitting of FeNi@NC-900 (a) before and (b) after stability test (Samples are denoted as FeNi@NC-900-before and FeNi@NC-900-after). ....	34
Figure 3.14 TEM images with (a) lower and (b) higher magnification of cycled FeNi@NC-900 (Denoted as FeNi-NC-900-after). ....	34
Figure 3.15 Schematic illustration of the applied route of precursor synthesis and the final TMP-based electrocatalyst derived therefrom. ....	36
Figure 3.16 (a) FT-IR spectra of FeNiP@NPC precursors, TA, PA, and PEI, and (b) Raman spectrum of the FeNiP@NPC precursor. ....	37
Figure 3.17 Schematic illustration of possible reactions related to the SSPs fabrication. ....	37
Figure 3.18 (a) XRD patterns of FeNiP@NPC, FeP@NPC, NiP@NPC, and NPC, and (b) Raman spectra of FeNiP@NPC, FeP@NPC, and NiP@NPC, and (c and d) deconvoluted Raman peaks of FeNiP@NPC. ...	38
Figure 3.19 (a, b) SEM images of FeNiP@NPC with high and low magnification, and (c) EDS element mapping of FeNiP@NPC. ....	39
Figure 3.20 (a) TEM image and (b, c) HRTEM images of FeNiP@NPC, and (d) partially enlarged XRD patterns of TMP@NPC. ....	40
Figure 3.21 TEM-EDS mapping analysis of the FeNiP@NPC sample. ....	41
Figure 3.22 XPS spectra of FeNiP@NPC (a) full-scan spectrum, (b) Ni 2p, (c) Fe 2p, (d) N 1s, (e) P 2p, and (f) C 1s peaks. ....	42
Figure 3.23 (a) Nitrogen adsorption-desorption isotherms of samples FeP@NPC, NiP@NPC, and FeNiP@NPC, and (b) pore size distribution of the FeNiP@NPC sample. ....	43
Figure 3.24 SEM images of (a) NPC, (b) NiP@NPC, (c) FeP@NPC, and (d) FeNiP@NPC. ....	43
Figure 3.25 (a) Polarization curves of NPC, FeP@NPC, NiP@NPC, and FeNiP@NPC, (b) polarization curves of FeNiP@NPC annealed at different temperatures, (c) the corresponding Tafel plots of NPC, FeP@NPC, NiP@NPC, and FeNiP@NPC, (d) EIS spectra of NPC, FeP@NPC, NiP@NPC, and FeNiP@NPC in 0.5 M H <sub>2</sub> SO <sub>4</sub> solution. ....	44

Figure 3.26 SEM images of (a) FeNiP@NPC-700, (b) FeNiP@NPC-800, (c) FeNiP@NPC-900, and (d) FeNiP@NPC-1000.....	45
Figure 3.27 SEM images of (a) FeNiP@NPC-700, and (b) EDS points analysis spectroscopy of point a and b in image a. ....	46
Figure 3.28 (a) Plots of current densities versus various scanning rates of NPC, FeP@NPC, NiP@NPC, and FeNiP@NPC, (b) LSV curves of FeNiP@NPC before and after 1000 potential cycles, the inset chronoamperometry of FeNiP@NPC at the constant potential of 195 mV vs. RHE in 0.5 M H <sub>2</sub> SO <sub>4</sub> solution.....	47
Figure 3.29 (a) OER polarization curves of NPC, FeP@NPC, NiP@NPC, and FeNiP@NPC, (b) polarization curves of FeNiP@NPC annealed at different temperatures, (c) the corresponding Tafel plots of NPC, FeP@NPC, NiP@NPC, and FeNiP@NPC, (d) the EIS spectra of NPC, FeP@NPC, NiP@NPC, and FeNiP@NPC in 1 M KOH solution. ....	48
Figure 3.30 TEM images of (a) FeNiP@NPC-800, (b,d) FeNiP@NPC-900, (c,e) FeNiP@NPC-1000. ....	49
Figure 3.31 (a) Plots of current densities versus various scanning rates of NPC, FeP@NPC, NiP@NPC, and FeNiP@NPC, (b) LSV curves of FeNiP@NPC before and after 1000 potential cycles, the inset shows the chronoamperometry of FeNiP@NPC at the constant potential of 1.51 V vs. RHE in 1 M KOH solution. ....	50
Figure 3.32 Schematic illustration of the formation of single-source-precursor and derived MoP@NPC/CNT-900.....	52
Figure 3.33 (a) FT-IR spectra of MoP@NPC/CNT precursors (MoNPC), NPC/CNT precursors (NPC), TA, PA, and PEI, and X-ray photoelectron spectrum of (b) C 1s and (c) N 1s of MoP@NPC/CNT precursor. ....	53
Figure 3.34 (a) FTIR spectra of MoP@NPC/CNT precursors (MoNPC), NPC/CNT precursors (NPC), TA, PA, and PEI, and (b) Raman spectrum of MoP@NPC/CNT precursors and NPC/CNT precursors. ....	54
Figure 3.35 (a) XRD pattern of MoP@NPC/CNT-900, NPC/CNT-900, and MoP-900, and (b) Raman spectra of MoP@NPC/CNT-900 and NPC/CNT-900. ....	54
Figure 3.36 (a-c) SEM images, (d-g) elemental mapping images, and (h) the EDS spectrum analysis of MoP@NPC/CNT-900.....	55
Figure 3.37 SEM images of (a) bare MoP-900 sample and (b) NPC/CNT-900 sample. ....	56
Figure 3.38 (a) Low-magnification TEM image, (b-d) high-resolution TEM images, (e-i) TEM elemental mapping images of C, N, P, and Mo of MoP@NPC/CNT-900, and (j) the hexagonal structure of MoP QDs. ....	57
Figure 3.39 High-resolution X-ray photoelectron spectroscopy spectra of (a) survey spectrum, (b) Mo 3d, (c) P 2p, (d) C 1s, (e) N 1s, and (f) O 1s of MoP@NPC/CNT-900.....	58
Figure 3.40 N <sub>2</sub> adsorption–desorption isotherms of MoP-900, NPC/CNT-900, and MoP@NPC/CNT-900, pore size distribution curve and pore volume area curve of MoP@NPC/CNT-900.....	59

Figure 3.41 (a) Polarization curves and (b) Tafel plots of the samples annealed at 900 °C with various amounts of MoP, bare NPC/CNT, and bare MoP in 0.5 M H <sub>2</sub> SO <sub>4</sub> .	60
Figure 3.42 HR-TEM images of (a) 0.5MoP@NPC/CNT-900, (b) MoP@NPC/CNT-900, and (c) 1.5MoP@NPC/CNT-900.	60
Figure 3.43 XRD patterns of 0.5MoP@NPC/CNT-900, MoP@NPC/CNT-900, and 1.5MoP@NPC/CNT-900.	61
Figure 3.44 (a) EIS Nyquist plots (inset is the partially enlarged image) and (b) current as a function of scan rate of the samples annealed at 900 °C with varying amounts of molybdate salts, NPC/CNT-900, and MoP-900.	61
Figure 3.45 (a) XRD patterns and (b) Raman spectra of the MoP@NPC/CNT samples derived from different pyrolysis temperature, and (c) deconvolution of Raman spectra of samples MoP@NPC/CNT-600 and MoP@NPC/CNT-1100.	62
Figure 3.46 N <sub>2</sub> adsorption–desorption isotherms of MoP@NPC/CNT-700, MoP@NPC/CNT-900, and MoP@NPC/CNT-1100.	62
Figure 3.47 (a) Polarization curves and (b) Tafel plots of the MoP@NPC/CNT samples annealed at different temperatures in 0.5 M H <sub>2</sub> SO <sub>4</sub> electrolyte.	64
Figure 3.48 (a) EIS Nyquist plots (inset is the partially enlarged image) and (b) current as a function of scan rate the MoP@NPC/CNT samples annealed at different temperatures in 0.5 M H <sub>2</sub> SO <sub>4</sub> electrolyte.	64
Figure 3.49 (a) Polarization curves of MoP@NPC/CNT-900 samples initially and after 1000 cycles, and (b) the time-dependent overpotential at constant current density input for 20 h in 0.5 M H <sub>2</sub> SO <sub>4</sub> electrolyte.	65
Figure 3.50 (a) Polarization curves and (b) Tafel plots of the MoP@NPC/CNT samples annealed at different temperatures in 1 M KOH electrolyte.	66
Figure 3.51 (a) EIS Nyquist plots (inset is the partially enlarged image) and (b) capacitive current as a function of scan rate the MoP@NPC/CNT samples annealed at different temperatures in 1 M KOH electrolyte.	66
Figure 3.52 (a) Polarization curves of MoP@NPC/CNT-900 samples initially and after 1000 cycles, and (b) the time-dependent overpotential at constant current density input for 20 h in 1 M KOH electrolyte.	66
Figure 4.1 Comparative evaluations of our materials studied in above sections((a) Section 3.1, (b) Section 3.2, and (c) Section 3.3) with reported TMCs/carbon-based catalysts.	70

---

---

## List of Tables

---

Table 2.1 Summary of overpotentials and Tafel slopes of reported TMA/carbon hybrid catalysts.....	13
Table 2.2 Summary of overpotentials and Tafel slopes of reported TMP/carbon hybrid catalysts. ....	14
Table 3.1 Summary of OER performance of sample FeNi@NC-900 compared with previously reported FeNi-based catalysts. ....	31
Table 3.2 Summary of Raman peaks fitting parameters for FeNi@NC-900-before and FeNi@NC-900-after. ....	35
Table 3.3 Summary of HER and OER performance of reported TMP/carbon-based catalysts. ....	51
Table 3.4 Summary of HER overpotentials at $-10 \text{ mA cm}^{-2}$ of some reported MoP-based catalysts. ....	67



---

---

## 1 Introduction

---

Hydrogen energy stands at the forefront of efforts to mitigate the ongoing energy crisis and reduce reliance on traditional fossil fuels.<sup>1</sup> This remarkable form of energy holds the promise of a cleaner, more environmentally friendly future. Its potential lies not only in its ability to serve as a clean energy carrier but also as a key player in reducing greenhouse gas emissions and combatting climate change. In this exploration of hydrogen energy and its production methods, a journey was initiated that delves deep into the science, technology, and innovation driving the transition towards a hydrogen-based economy. One of the most promising methods for producing hydrogen on a mass scale is through the process of water-splitting.<sup>2</sup> This process, which occurs through the application of an electric current to water, effectively disassembles H<sub>2</sub>O molecules into their constituent elements: hydrogen and oxygen. Water-splitting has garnered widespread recognition for its potential to revolutionize the energy landscape by providing a sustainable source of hydrogen, a versatile energy carrier.

Within the heart of the water-splitting process, two half-electrochemical reactions unfold at distinct electrodes: the hydrogen evolution reaction (HER) takes place at the cathode, where hydrogen ions gain electrons and transform into molecular hydrogen gas (H<sub>2</sub>), while the oxygen evolution reaction (OER) unfolds at the anode, where oxygen molecules are liberated from water molecules. These reactions are the lifeblood of water-splitting, driving the conversion of water into its elemental constituents.<sup>3,4</sup> For hydrogen production to be efficient and scalable, the development of cathode and anode electrocatalyst materials with exceptional efficiency, stability, and cost-effectiveness is of paramount importance. Traditionally, noble metal-based catalysts, such as platinum (Pt) and iridium (Ir), have been the go-to choices for catalysing these reactions due to their outstanding electrocatalytic properties. Noble metals have the advantage of low overpotential ( $\eta$ ), meaning they can promote these reactions with minimal energy input. However, this reliance on noble metals presents a significant challenge: their limited reserves and concerns regarding their long-term durability hinder their widespread industrial adoption. This limitation has spurred a quest for alternative materials that can match or even surpass the performance of noble metals while offering sustainability and cost-effectiveness.<sup>5</sup>

In response to the need for efficient hydrogen and oxygen production, researchers have shifted their focus towards non-precious transition metals, particularly those that are abundant, and their multiple compounds. These materials have exhibited potential in the creation of electrochemically active nanostructures. Among the promising candidates are carbides, chalcogenides, nitrides, phosphides, and various metal alloys.<sup>6,7</sup> Their allure lies in their high catalytic activity, a trait validated by both theoretical predictions and experimental findings. Moreover, these materials hold the promise of relative affordability, making them attractive options for sustainable hydrogen production.

---


Nonetheless, significant challenges persist in unlocking the full potential of these transition metal compounds (TMCs). Two prominent issues are electronic conductivity and porosity. Poor electronic conductivity can hinder the efficient flow of electrons during catalytic reactions, reducing the overall catalytic activity. Inadequate porosity limits the exposure of active sites, diminishing the catalytic efficiency of these materials. Additionally, the electrochemical environment in which these materials operate, be it acidic or alkaline, presents a significant challenge. The harsh conditions can lead to heavy corrosion and a decline in catalyst activity over time. To address these obstacles and harness the full potential of non-precious TMCs, innovative strategies and methods are required, such as:

- i. Heteroatom-doping and vacancies engineering: One approach to enhancing catalytic activity involves optimizing the electronic structure of electrocatalysts through heteroatom-doping and vacancies engineering. This innovative technique can yield highly effective catalysts by fine-tuning their electronic properties.<sup>8</sup>
- ii. Heterostructure formation: Another promising avenue is the effective combination of different active compounds to fabricate heterostructures. These heterostructures enhance charge transfer between materials, promoting catalytic activity and overall efficiency.<sup>9</sup>
- iii. Morphological and nanostructural control: Precise control over the morphology and nanostructure of materials is essential. This control can increase porosity, expose more active sites, and provide protective mechanisms to enhance both activity and long-term durability. Proper morphological design is crucial for stability and performance.<sup>10</sup>

Amid these strategies, carbon-based materials have emerged as frontrunners for hosting active TMCs. The unique properties of carbon materials make them well-suited for this role. Carbon materials can expose more active sites, improve conductivity, ensure a higher active site density, and facilitate a synergistic effect between carbons and TMCs to enhance overall performance.<sup>11</sup> Within the realm of carbon materials, extensive efforts have been devoted to developing non-metal heteroatom (N, S, P, and B) doped carbon. These heteroatom-doped carbons introduce additional active sites for electrochemical processes by fostering synergistic effects between different types of atoms. Furthermore, the morphology of the synthesized material plays a pivotal role in its stability and activity. For instance, the construction of core-shell structured electrocatalysts serves a dual purpose: it effectively confines the growth of particles, preventing the corrosion of transition metal-based nanoparticles, and modifies the electronic and chemical configurations. This modification enhances electron transport between the core and shell, further improving catalytic performance and durability.<sup>12</sup>

Building upon these crucial principles, this dissertation represents a significant contribution to the field of electrocatalysis. It focuses on the exploration of TMCs encapsulated within carbon nanomaterials





---

doped with non-metal heteroatoms. These nanomaterials are synthesized through an innovative single-source-precursor pyrolysis method, a testament to the continuous evolution of materials science and chemistry. Through systematic investigation and experimentation, this research seeks to unlock the potential of these innovative materials and their application in electrocatalysis.



## 2 Fundamentals

The fundamentals related to all the studies in this dissertation are introduced in this chapter, including the theoretical background of water electrocatalysis and the state of the art in the development and improvement of electrocatalysts.

### 2.1 Electrocatalysis of water splitting

It is widely acknowledged that the process of electrolytic water splitting faces both thermodynamic and kinetic challenges. The uphill nature of the reaction is indicated by the positive Gibbs free energy ( $\Delta G$ ) value, as shown in Figure 2.1a. In addition, a significant kinetic barrier must be surmounted. Catalysts play an indispensable role in making this possible by lowering the kinetic barrier and facilitating the reaction.<sup>13</sup>

#### 2.1.1 Electrocatalysis reaction mechanism

The water splitting process can be divided into two distinct half-reactions: the cathodic HER and anodic OER, which occur in different electrolytes as shown in Equations (1)-(4) and depicted in the schematic illustration in Figure 2.1b. During the electrolytic water splitting process, different electrochemical reactions will occur on the anode and cathode, depending on the pH values of the electrolytes.

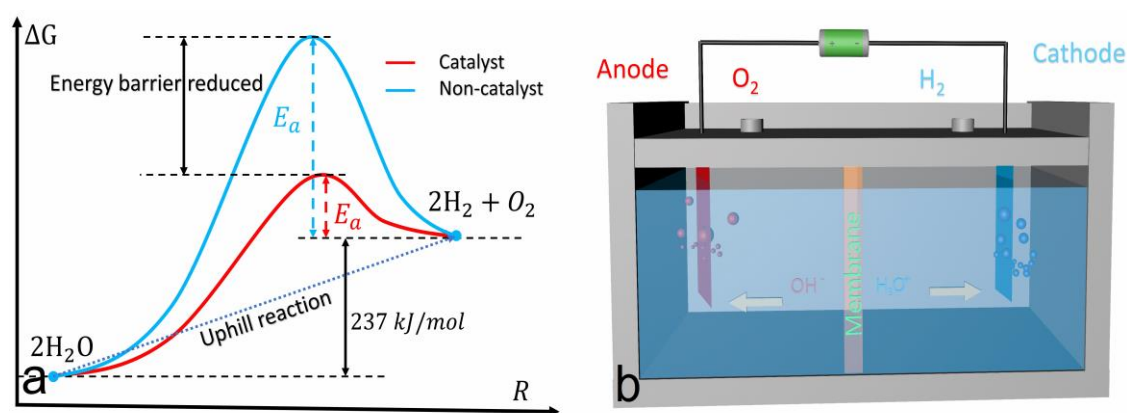
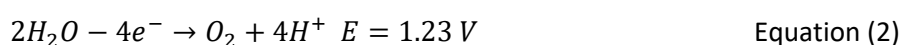
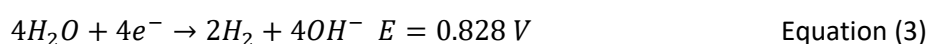


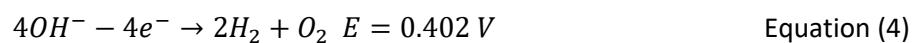
Figure 2.1 (a) Schematic description of the energy diagram for the water splitting process and (b) illustration of a water splitting electrolyser cell.

In an acidic electrolyte:



In an alkaline electrolyte:





Total reaction:



It has been established that the theoretical thermodynamic voltage ( $E$ ) for water splitting is 1.23 V under conditions of 298 K and 1 atm, in both acidic and alkaline electrolytes.<sup>3</sup> However, the actual operating voltage ( $E_{op}$ ) (Equation (6)) for water electrolysis is significantly greater than 1.23 V, typically around 1.5-2.0 V, requiring additional energy input. This excess potential is referred to as the overpotential, which results from inherent activation barriers in the process.<sup>14</sup>

$$E_{op} = E + E_a + E_c + E_r \quad \text{Equation (6)}$$

Where  $E_a$  is the overpotential of the anode for carrying out the OER,  $E_c$  is the overpotential of the cathode for performing the HER, and  $E_r$  is the excess potential produced from electrolyte diffusion, surface polarization (capacitance), and other sources of counter electromotive force all play a role in water splitting. However,  $E_a$  and  $E_c$  are particularly relevant to the activity of the electrocatalysts at the anode and cathode for OER and HER, respectively. As a result, the use of appropriate electrocatalysts as the anode and cathode materials can significantly decrease  $E_a$  and  $E_c$  and thus improve the electrocatalytic activity of water splitting for a more efficient outcome.

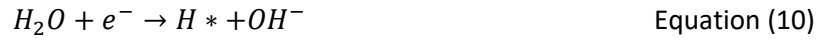
### Mechanism of cathodic HER

The HER process with a two-electron transfer is typically understood as an adsorption-desorption process of intermediates. In acidic media, a proton adsorbs onto the surface of the electrocatalyst, followed by the removal of one electron, resulting in the formation of the adsorbed intermediate  $H^*$  (Where  $*$  represents the adsorbed active site). This step is referred to as the Volmer step (Equation (7)). Subsequently, the adsorbed  $H^*$  combines with another  $H^+$  and loses another electron, leading to the generation of a hydrogen molecule, this step is called the Heyrovsky step (Equation (8)). Alternatively, under high coverage of surrounding  $H^*$ , the adsorbed  $H^*$  can combine with another  $H^*$  to form a hydrogen molecule, this step is known as the Tafel step (Equation (9)).<sup>15</sup>



Regardless of whether the Volmer-Heyrovsky or Volmer-Tafel mechanism is in play, the hydrogen adsorption free energy ( $\Delta G_{H^*}$ ) is widely accepted as the standard for hydrogen evolution activity.<sup>16</sup> Unlike the two-step process in acidic media, the HER process in alkaline media begins with the

dissociation of an adsorbed water molecule on the surface (Equation (10)), due to the absence of protons. As a result, hydrogen can be produced through the combination of  $H^*$  with a water molecule (Equation (11)) or the coupling of intermediates (Equation (9)), The reactions and intermediates involved in the HER are illustrated in Figure 2.2a.<sup>17</sup>



Therefore, it is crucial to find a balance between favoured water dissociation and moderate hydrogen adsorption energy, which means that the kinetics of HER are slowed down in alkaline conditions.

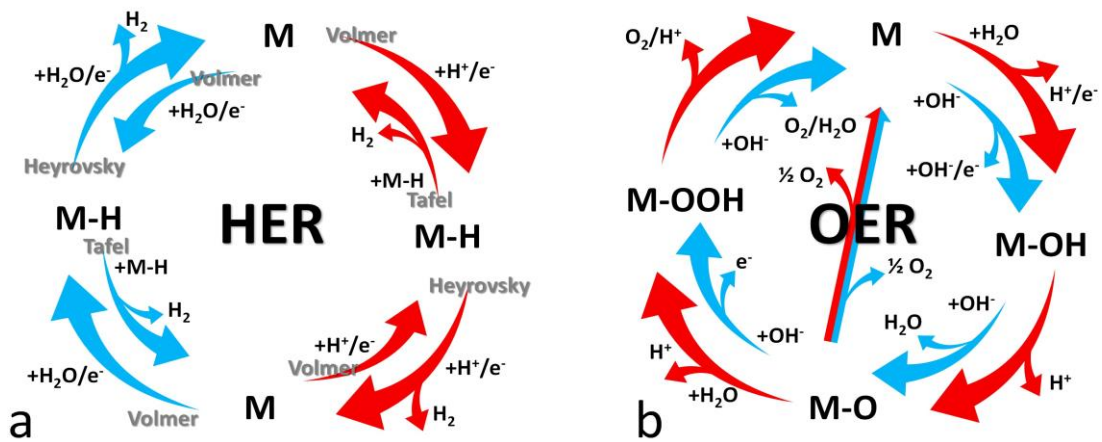
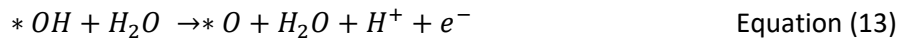


Figure 2.2 Schematic illustration of the (a) HER and (b) OER mechanism in both acidic and alkaline media.

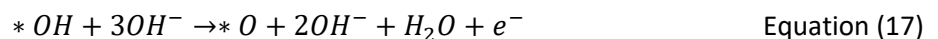
### Mechanism of anodic OER

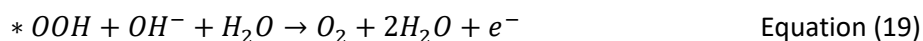
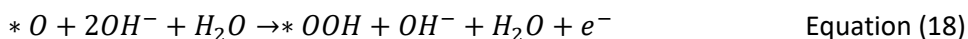
The schematic of OER is shown as Figure 2.2b, OER process undergoes four-electron transfer with multiple intermediates in both acidic and alkaline media as described in Equations (12)-(19).

In acidic media:



In alkaline media:





The total free energy change ( $\Delta G$ ) for the OER is calculated to be 4.92 eV, which can be divided equally among the four elemental steps involving different adsorbates ( $*OH$ ,  $*O$ ,  $*OOH$ ,  $O_2$ ) for a thermodynamically ideal electrocatalyst.<sup>18,19</sup> In this case, the equilibrium potential should be high enough to drive the OER. However, the constant adsorption free energy difference between  $*OH$  and  $*OOH$  is estimated to be 3.2 eV regardless the bonding sites. The optimal placement of  $*O$  between  $*OH$  and  $*OOH$  can minimize the free energy change as much as possible. As a result, the minimum overpotential value is estimated to be between 0.4-0.2 V, indicating that the dynamics of OER are much less favourable compared to HER.

### 2.1.2 Evaluation parameters for HER and OER catalyst

It's important to understand several parameters to evaluate the performance of the as-prepared catalysts, such as overpotential ( $\eta$ ), Tafel slope ( $b$ ), solution resistance ( $R_s$ ), charge transfer resistance ( $R_{ct}$ ), electrochemical active surface area (ECSA), Faradaic efficiency (FE), chronoamperometry (CA), and chronopotentiometry (CP).

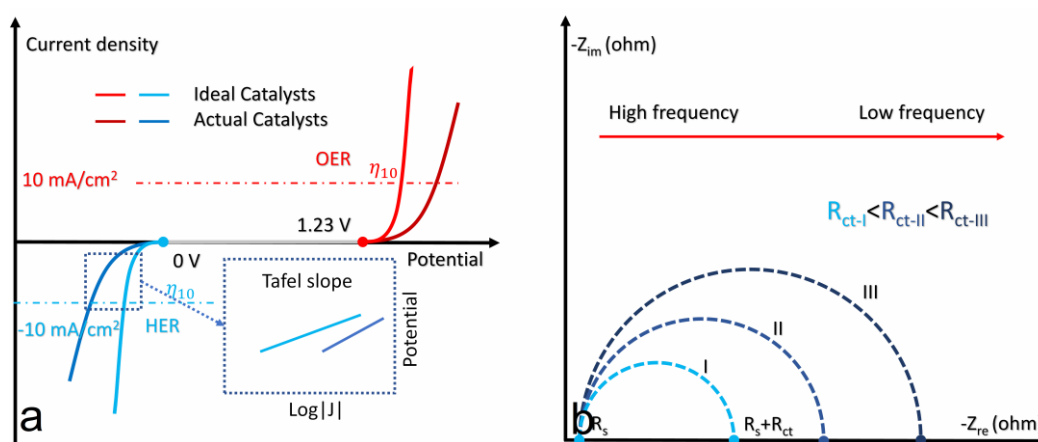


Figure 2.3 The illustrations of (a) the evaluation parameters of electrocatalysts, including overpotential and Tafel slope, and (b) Nyquist representation of electrochemical impedance spectroscopy.

### Overpotential

In practical electrocatalysis systems, an extra potential (Equation (20) and (21)) beyond the equilibrium potential (0 V vs RHE for HER and 1.23 V vs RHE for OER) is needed to initiate the HER and OER process because of the resistance, concentration, and activity polarization induced potential. Therefore, this extra potential is called overpotential ( $\eta$ ) (mentioned in section 2.1.1), which is highly correlated to the intrinsic activity of the electrocatalyst and used to evaluate the performance of potential electrocatalyst. Therefore, it is obvious that the aim for an electrocatalyst application is to

---

decrease the energy input. Proper electrocatalyst can effectively enhance the efficiency of electrocatalysis process as the diagram shown in Figure 2.3a. Potential ( $E_p$ ) can be measured by linear scan voltammetry (LSV) curves with an  $iR$  correction according to Equation (22).<sup>20</sup>

$$E_p = \eta + 0 V \quad \text{Equation (20)}$$

$$E_p = \eta + 1.23 V \quad \text{Equation (21)}$$

$$E_p = E_{RHE} - iR \quad \text{Equation (22)}$$

Where  $E_p$  is the  $iR$ -corrected potential,  $E_{RHE}$  is the measured potential with respect to reversible hydrogen electrode (RHE),  $i$  is the measured current, and  $R$  is the uncompensated resistance as determined by electrochemical impedance spectroscopy (EIS). Through temperature and agitation speed increasing can facilitate the ion diffusion to minimize the concentration overpotential. The overpotential at current density of  $10 \text{ mA cm}^{-2}$  is denoted as the most important reference for assessing the performance of electrocatalysts, corresponding to the approximate current density for a 10% efficient solar-to-fuels conversion under sun illumination.<sup>21</sup>

### Tafel slope

Tafel slope ( $b$ ), obtained from the linear extrapolation of LSV plots through the application of Tafel equation (Equation (23)),<sup>22</sup> serves as a crucial indicator of electrocatalytic performance.

$$\eta = a + b \log(j) \quad \text{Equation (23)}$$

Where  $\eta$  denotes the overpotential,  $j$  is the current density,  $b$  and  $a$  are Tafel slope and Tafel constant, respectively.  $b$  represents the rate of charge transfer, is inversely proportional to the overpotential, and a lower value of Tafel slope corresponds to a higher charge transfer ability. In order to obtain a reliable value of the Tafel slope, it is important to avoid the effects of concentration polarization by limiting the analysis to low overpotential ranges. Tafel slope is also a valuable indicator of the reaction pathway in HER. Through the determination of the Tafel slope, it is possible to identify the rate-limiting steps of the reaction and to distinguish between different pathways. An alternative method to obtain a more accurate value of the Tafel slope is through the use of EIS. In this approach, Nyquist plots are obtained at various overpotentials at fixed intervals, and the Tafel slope is determined by fitting the plot of  $\log(R_{ct})$  versus  $\eta$ , where  $R_{ct}$  represents the charge transfer resistance. This method allows for the exclusion of electron transfer resistance and provides a value of the Tafel slope that is more representative of the intrinsic charge transfer.

### Faradaic efficiency

Another parameter used to evaluate electrochemical reactions is the Faradaic efficiency (FE). This

---

measures how efficiently electrons are transferred during the desired reaction, such as HER or OER, compared to other side reactions in the system. To calculate the FE, the quantity of gas produced experimentally (H<sub>2</sub> or O<sub>2</sub>) is compared to the expected quantity based on theoretical calculations. Experimental production of H<sub>2</sub> and O<sub>2</sub> can be determined using gas chromatography (GC) or the water gas displacement method, while theoretical production can be obtained by integrating galvanostatic or potentiostatic electrolysis. Although the FE is critical for assessing the efficiency of electrochemical reactions, for most HER and OER catalysts it is close to 100%, so it is less critical for comparison purposes among reported catalysts.

### Charge transfer resistance

The  $R_{ct}$  is a measure of the resistance to electron transfer between two phases, and is directly proportional to the charge transfer ability of an electrocatalyst. This value can be obtained through the application of EIS by fitting a Nyquist plot (Figure 2.3b) to a suitable equivalent circuit.<sup>23</sup> The value of the charge transfer resistance is reflected in the diameter of the semicircle in the Nyquist plot, with larger diameters indicating higher resistance to electron transfer and vice versa. The relationship between the real impedance ( $Z_{re}$ ) and the imaginary impedance ( $Z_{im}$ ) is expressed in Equation (24) based on the principles of EIS theory,  $R_s$  is the resistance of the electrolyte solution.

$$(Z_{re} - R_s - \frac{R_{ct}}{2})^2 + Z_{im}^2 = (\frac{R_{ct}}{2})^2 \quad \text{Equation (24)}$$

### Electrochemical active surface area

In general, the electrochemical efficiency is determined by intrinsic activity of catalytic sites and the accessible number of active sites. Because of the different adsorbates and conditions of tests, the specific surface areas derived from the Brunauer-Emmett-Teller (BET) N<sub>2</sub>-adsorption test are not completely coincided with the ECSA which is the area mass and charge transfer happened during the electrocatalysis.<sup>24</sup> However, the BET surface area is the total area of surface, inside pore surface, and voids, some of the areas are not functional for the electrocatalysis process. Thus, the electrochemical active surface areas are generally evaluated by the positively-related double layer capacitance ( $C_{dl}$ ) to verify the catalytic efficiency of potential electrocatalyst.<sup>25</sup> The  $C_{dl}$  can be calculated from the CV curves measured under regular sweep speeds intervals in a non-Faradaic region. The  $\Delta j/2$  of the intermediate potential value is calculated, and the line is fitted with the scan speed as X-axis and the  $\Delta j/2$  as Y-axis, the larger slope value represents the higher  $C_{dl}$ , namely a higher ECSA.<sup>26</sup>

### Stability

Long-term stability is another significant indicator for the electrocatalysts application. It can be characterized by either dynamic continuous cyclic voltammetry (CV) or steady-state electrolysis



---

method by chronoamperometric and chronopotentiometry measurements.<sup>21</sup> The accelerated degradation CV test can be subjected the electrocatalyst to the CV cycling at high scan rate, which normally runs over thousands of cycles for HER and OER. The shift of the overpotential indicates the stability of the electrocatalyst. The smaller shift means the better stability. When applied chronoamperometric and chronopotentiometry measurements for stability test, it generally lasts for at least 10 h. The drop of the current density at a fixed potential or the increase of the overpotential at a fixed current density (normally at 10 mA cm<sup>-2</sup>) reflects the stability of the catalysts. The less change of current density or the overpotential indicates a better stability. Generally, the overpotential will increase from the LSV curves after numbers of cycles, due to the active material falling off and the consumption of the electrolyte during long-term test. In addition, the multistep chronoamperometric method can directly reflect the stability of the catalysts under different current densities.

## **2.2 Transition metal compounds/carbon hybrids as electrocatalyst**

To date, noble metal Pt-based and Ru -based are demonstrated as the state-of-the-art HER and OER electrocatalysts, respectively. However, their scarcity and high cost are major obstacles for the large-scale production and commercial application. Therefore, more efforts are focused on developing low-price but high-performance alternatives such as heteroatom doped nanocarbons and transition metal-based materials. Nanocarbon-based materials have become increasingly attractive due to their intrinsic excellent stability and conductivity, potential high specific surface area, and amazing mechanical strength. Additionally, they are abundant, low-cost and environmentally friendly. Thus, some of the carbon-based materials are expected to increase the catalytic performance after introducing heteroatoms, such as single heteroatom doping O, N, P, B, S, the co-doping of ON, BN, NP, NS, and heteroatom tri-doping into the carbon matrix, benefiting from the modulation of charge distribution to the nearby carbon atoms. For transition metal-based materials, much research has been focused on developing low-cost and efficient transition metal based electrocatalysts for the OER and HER. For example, carbides,<sup>27-29</sup> nitrides,<sup>30-32</sup> phosphides,<sup>33,34</sup> sulfides,<sup>35,36</sup> metal alloys.<sup>37-39</sup> and other derivatives are active for the HER or OER. However, to date, the TMCs are insufficient for large-scale and practical production obstructed their relatively low activity and poor stability.

Based on two main alternatives mentioned above, nanocarbon-TMCs hybrid materials have been proposed as high-performance electrocatalysts. Due to their multiple structures, intrinsic high conductivity, and chemical stability. Nanocarbon is also an attractive potential substrate for accommodating TMCs that are semiconductors or insulators. The presence of nanocarbon can effectively tune the  $\Delta G$  of intermediates adsorption, making the desorption of hydrogen for HER more facile. Moreover, nanocarbon can offer superior conductivity and expose more active sites to facilitate mass and charge transfers, leading to a significant enhancement in electrochemical activities.

Furthermore, theoretical density functional theory (DFT) calculations studies<sup>40,41</sup> have indicated the existence of synergistic effects between the carbon layer and the encapsulated inner TMCs to provide excellent catalytical performance. In addition, the formation of carbon layers has the potential to prevent direct contact between TMCs and harsh electrolytes, thereby enhancing corrosion resistance and improving long-term stability. Figure 2.4 highlights the potential choices for carbon species and TMCs. The following sections will discuss transition metal alloys (TMAs)/carbon and phosphides (TMPs)/carbon hybrids in detail.

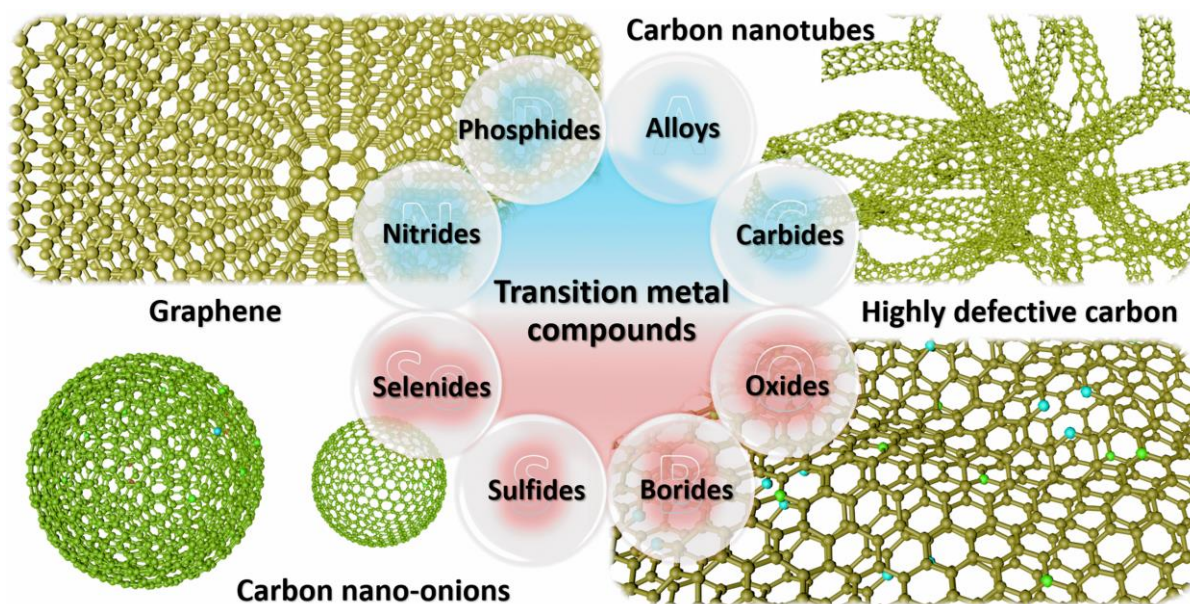


Figure 2.4 Nanostructure choices of carbon species and potentially coupled TMCs as electrocatalysts for water splitting.

### 2.2.1 Transition metal alloy/carbon hybrid

The combination of TMAs and nanocarbon species has been identified as a promising strategy for improving the activity and durability of electrocatalysts. This is due to the attractive crystallographic and electronic properties of transition metal alloys, which are composed of at least two transition metallic elements. Studies have demonstrated that heteroatom-doped carbon-encapsulated transition metals and transition metal alloys, particularly those containing Fe, Co, and Ni, exhibit exceptional performance in HER and OER.<sup>42-44</sup> The catalytic effect of Fe, Co, and Ni can also convert amorphous carbon into graphitized carbon on the surface of the transition metal or transition metal alloy particles during low-temperature pyrolysis, resulting in carbon layers with high conductivities. These carbon layers prevent direct contact between strong acid electrolytes and metal particles, thus enhancing the stability of the electrocatalyst as well. For instance, Lei et al.<sup>45</sup> synthesized  $\text{Fe}_1\text{Co}_2$  alloy nanoparticles embedded in N-doped carbon nanotubes/carbon nanosheets. The interaction of Fe and Co and the partially oxidized ionic state of cobalt and iron contribute to the enhanced intrinsic catalytic

activity of the material. The porous nanocarbon frameworks of the CNTs/CNSs also facilitate exposure of active sites and mass/charge transportation. Shah et al.<sup>46</sup> fabricated a FeNi@nitrogen-doped graphene dispersed in a nitrogen-doped carbon matrix. The fast electron transfer from the core FeNi alloy to the nitrogen-doped carbon shells and the long-term stability provided by the chemically stable shells result in outstanding OER performance. A summary of various reported TMA/carbon electrocatalysts for HER and/or OER is presented in Table 2.1.

Table 2.1 Summary of overpotentials and Tafel slopes of reported TMA/carbon hybrid catalysts.

TMA/carbon hybrid <sup>a</sup>	Tafel slopes (HER/OER)	$\eta_{HER}^b / \eta_{OER}^c$	Ref.
NiFe-NC/Me-NC	118 mV dec <sup>-1</sup> /44 mV dec <sup>-1</sup>	271 mV /231 mV	47
FeCo@NG	74 mV dec <sup>-1</sup> /-	262 mV /-	48
NiCoFe@N-CNFs	-/72 mV dec <sup>-1</sup>	-/270 mV	49
CoMo@NC	-/61 mV dec <sup>-1</sup>	-/143 mV	50
f-FeCo-CNT	-/101 mV dec <sup>-1</sup>	-/310 mV	51
FeCo@N-HC	-/91.9 mV dec <sup>-1</sup>	-/318 mV	52
Co <sub>0.95</sub> Cu <sub>0.05</sub> @CNWs	172 mV dec <sup>-1</sup> /92 mV dec <sup>-1</sup>	160 mV/285 mV	53
N-HPCS@CoCuFe NSs	73.7 mV dec <sup>-1</sup> /-	114 mV/-	54
Fe <sub>3</sub> Co <sub>7</sub> @PCNSs	-/53.16 mV dec <sup>-1</sup>	-/300 mV	55
CoFe@NC/NCHNSs	144 mV dec <sup>-1</sup> /39 mV dec <sup>-1</sup>	120 mV/285 mV	56
Co0.75Ni0.25/CC	100 mV dec <sup>-1</sup> /-	108 mV/-	57
CuNi-NC	72 mV dec <sup>-1</sup> /76 mV dec <sup>-1</sup>	169 mV/390 mV	58
NiFe@CC	85 mV dec <sup>-1</sup> /64 mV dec <sup>-1</sup>	256 mV/281 mV	59
C@NiCo12	106 mV dec <sup>-1</sup> /157 mV dec <sup>-1</sup>	104 mV/320 mV	60
CuNi/FTO	-/92 mV dec <sup>-1</sup>	-/294 mV	61

<sup>a</sup> Transition metal alloys/carbon complex material.

<sup>b</sup> HER overpotential at a current density of -10 mA cm<sup>-2</sup> (based on electrode geometric area).

<sup>c</sup> OER overpotential at a current density of 10 mA cm<sup>-2</sup> (based on electrode geometric area).

## 2.2.2 Transition metal phosphide/carbon hybrid

TMP is an important non-precious electrocatalyst as well, Rodriguez et al.<sup>62</sup> first reported that the potential application of Ni<sub>2</sub>P for HER by DFT calculations, as the (001) plane of Ni<sub>2</sub>P showed a high level of activity, even surpassing that of the Pt/C electrocatalyst, indicated that Ni<sub>2</sub>P's (001) plane indeed possessed exceptional HER activity. The performance is attributed to the phosphorus introduction, thereby weakening the strong hydrogen absorption of metallic Ni and facilitate the facile desorption of hydrogen from the Ni<sub>2</sub>P, which gives an important theoretical prediction for the metal phosphides application. Base on above background, the numerous TMPs/carbon hybrids, such as Fe<sub>2</sub>P, Ni<sub>2</sub>P and

CoP have been well investigated. Jiang et al.<sup>63</sup> synthesized hierarchical Fe<sub>2</sub>P@CNP/NPC nanocomposites comprising Fe<sub>2</sub>P crystal nanoparticles encapsulated by the N, P co-doped carbon shell, the excellent performance is resulted from the synergetic effect between heteroatom N and P co-doped carbon and well wrapped Fe<sub>2</sub>P nanoparticles. In another example, Peng et al.<sup>64</sup> designed a hybrid of nitrogen-doped carbon shell coated CoP nanocrystals encapsulated in porous nitrogen-doped carbon substrate, which exhibits promising electrocatalytic activity and durability toward HER and OER due to the synergistic effect between N-doped carbon and CoP nanoparticles. Moreover, some other transition metals phosphides including Mo, W, and bimetallic or trimetallic phosphides have also been successfully fabricated through various studies.<sup>65,66</sup> And compared with naked metal phosphides, both the activity and stability of the resulting carbon-encapsulated metal phosphides are greatly improved. The electrocatalytic activities of some reported TMPs/carbon hybrids are summarized in Table 2.2.

Table 2.2 Summary of overpotentials and Tafel slopes of reported TMP/carbon hybrid catalysts.

TMPs/carbon hybrid <sup>a</sup>	Tafel slopes (HER/OER)	$\eta_{HER}^b / \eta_{OER}^c$	Ref.
CoP@C nanocables	61 mV dec <sup>-1</sup> /-	170 mV /-	67
H-CoP@NC	71 mV dec <sup>-1</sup> /73 mV dec <sup>-1</sup>	200 mV/320 mV	68
Ni <sub>2</sub> P/N-doped rGO	59 mV dec <sup>-1</sup> /-	102 mV/-	69
NiCoP/C	-/96 mV dec <sup>-1</sup>	-/330 mV	70
CoP/rGO	57 mV dec <sup>-1</sup> /80 mV dec <sup>-1</sup>	120 mV/292 mV	71
Co-P@NC-800	74 mV dec <sup>-1</sup> /79 mV dec <sup>-1</sup>	98 mV /370 mV	72
Co <sub>2</sub> P/Ni <sub>2</sub> P/CNT	41.6 mV dec <sup>-1</sup> /-	151 mV/-	73
FeP NPs@NPC	67 mV dec <sup>-1</sup> /-	130 mV/-	74
MoP@NC	57 mV dec <sup>-1</sup> /-	135 mV/-	75
Ni <sub>2</sub> P/CNT	53 mV dec <sup>-1</sup> /-	124 mV/-	76
Co <sub>1</sub> Ni <sub>1</sub> -P@C	73 mV dec <sup>-1</sup> /-	169 mV/-	77
NiFeP@C	38.8 mV dec <sup>-1</sup> /75.8 mV dec <sup>-1</sup>	160 mV/260 mV	78
CoP@NPC	73 mV dec <sup>-1</sup> /61.3 mV dec <sup>-1</sup>	184 mV/303 mV	79
WP NPs@NC	102 mV dec <sup>-1</sup> /-	150 mV/-	80
NiCoFeP/C	108 mV dec <sup>-1</sup> /65 mV dec <sup>-1</sup>	149 mV/270 mV	81

<sup>a</sup> Transition metal phosphides/carbon complex material.

<sup>b</sup> HER overpotential at a current density of -10 mA cm<sup>-2</sup> (based on electrode geometric area).

<sup>c</sup> OER overpotential at a current density of 10 mA cm<sup>-2</sup> (based on electrode geometric area).

### 2.3 Transition metal compounds/carbon hybrids fabrication

Thus far, the commonly used strategies for fabrication of TMCs/carbon hybrids can be broadly

categorized into three methods: (i) Gas-phase synthesis, (ii) Liquid-phase synthesis, and (iii) Solid-phase synthesis as illustrate in Figure 2.5. In addition, an emerging facile high-temperature pyrolysis of single-source-precursors, precursors contain both metals and carbon source, (i.e. organic molecules and polymer), under specific atmosphere has been proposed. Single-source-precursor approach is the synthesis method utilized in present dissertation.

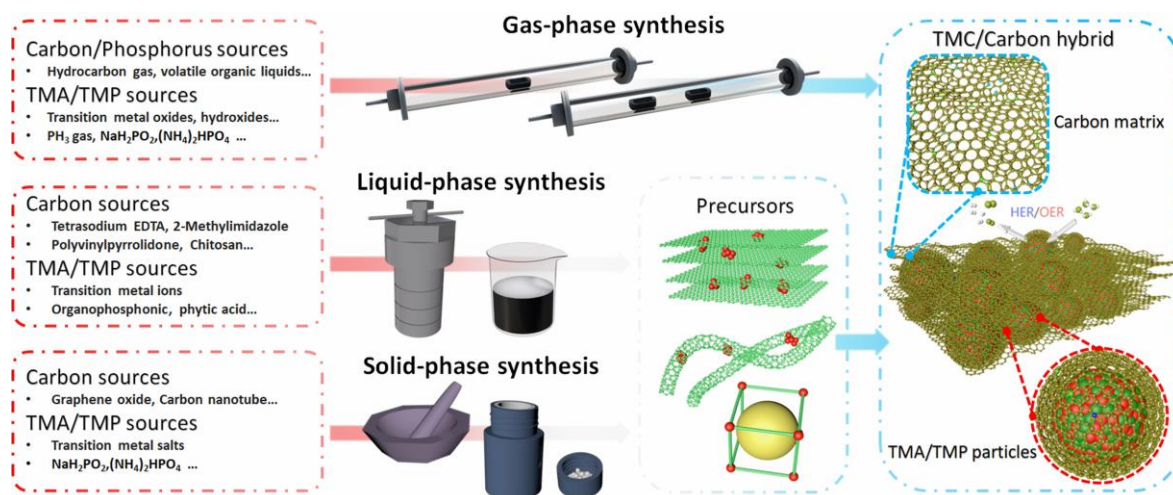


Figure 2.5 Different TMCs/carbon hybrids fabrication method.

### 2.3.1 Traditional synthesis methods

For the TMA/carbon hybrids synthesis, the chemical vapor deposition (CVD) route was utilized for preparing TMA/carbon hybrids with an encapsulating carbon shell as a representative gas-phase synthesis, which can also control over the carbon layers growth on the carbon shell. For example, Deng and co-workers successfully encapsulated FeCo alloy into nitrogen-doped carbon nanotubes (CNTs) via a simple CVD method. The nitrogen dopants amount could be easily tuned during the preparation the derived catalyst exhibited remarkable catalytic for the HER in acidic media. Furthermore, the obtained catalysts also showed an excellent long-term durability for 10000 cycles of accelerated degradation test.<sup>82</sup> Metal organic frameworks (MOFs) pyrolysis, as the representative of liquid-phase synthesis, has shown some distinct advantages such as structure inheritance, possible high specific surface area and porosity, which enable them to be promising candidate precursors to obtain transition metal compounds/carbon hybrids material. Chen and his co-workers reported a facile one-step annealing strategy of  $\text{Fe}_3[\text{Co}(\text{CN})_6]_2$  for synthesizing the FeCo alloy encapsulated in N-doped graphene layers which showed excellent activity for HER.<sup>83</sup> During annealing, the iron and cobalt were converted to metal alloy by carbon reduction effect, and the formed alloy nanoparticles were wrapped in carbon shells. The electronic state of carbon atoms could be adjusted by adjoining N atom to derive potential active sites and a better conductivity. Meanwhile, the dopants and the core-shell nanostructure optimized the free energy of hydrogen adsorption and improving the catalytic activity.<sup>48</sup> Solid phase

---

synthesis was utilized to fabricate multicomponent Co/Cu Composite by Zhang et al.,<sup>84</sup> through grinding the mixture of metal precursor and dicyandiamide to obtain the precursor, then followed by a pyrolysis process to convert the precursor to final material.

For the synthetic strategies of TMPs/carbon hybrid materials, it can not only be classified into three different types as above mentioned, but also can be categorized according to different adapted phosphorus sources, the inorganic P sources are commonly in some gas and solid-phase reactions like the post-phosphidation by  $\text{PH}_3$ , while the organic phosphorus often introduced into liquid-phase reactions to serve as the P source of TMPs.

The inorganic P sources including  $\text{NaH}_2\text{PO}_2$  and  $((\text{NH}_4)_2\text{HPO}_4)$  are commonly used to synthesize the TMPs/carbon hybrid.<sup>85</sup> The most well utilized route is resembling the transition metal/carbon precursors (oxides/carbon, alloys/carbon) by  $\text{PH}_3$  chemical vapor deposition. The precursors directly reacted with the inorganic P source generated  $\text{PH}_3$  to convert oxides and alloys into TMPs during the pyrolysis. It is worth mentioning that the morphology will mostly retain after the  $\text{PH}_3$  CVD process. In another route, white P was also employed for phosphorization processes, with this P source, the products could be regulated by the different reactant ratios, thereby, different TMPs are prepared in this way, such as MoP/C nanohybrids, but the aggregation happens during the long time and high temperature annealing.<sup>86</sup> Besides, rigorous operation and airtight reaction system are required to protect from the hypertoxic white P and phosphine produced during the synthesis. And another P source is phosphate, which can be reduced to phosphides in a  $\text{H}_2$  atmosphere through a gas reduction reaction.<sup>87</sup>

Although the inorganic P source is commonly involved in TMPs synthesis, the further development of other synthetic strategies is required to avoid the potential harmful influence of the dangerous P and the  $\text{PH}_3$ . A supermolecule of organophosphonic acid–polyaniline is fabricated as an organic phosphorization reagent,<sup>88</sup> which could form a cross-linked structure by coordinating with transition metals. Then, the TMPs/carbon hybrid was formed after the carbothermal reduction. In additionally, the phytic acid is also an emerging and efficient phosphorization reagent to prepare TMPs/carbon hybrids. Notably, these organic P sources are advantageous for the fabrication of TMPs/carbon hybrids because of the safety and nontoxicity considerations. And these carbonaceous P sources commonly could facilitate the formation of hybrids of TMPs encapsulated in P-doped carbon materials under one-step facile pyrolysis. The last route for preparing TMPs/carbon hybrid is the pyrolysis of the P-ligands containing MOFs. The MOFs display good compatibility of different TMPs via coordinating with one or more TMs at atomic level, which is responsible for the construction of homogenous TMPs/carbon materials.<sup>89</sup> It is noteworthy that this facile one-step pyrolysis process can greatly retain the morphology with further derived large specific surface area, highly porous structure, and desirable

chemical composition as well as excellent electrocatalytic performance.

### 2.3.2 Single-source-precursor method

In this dissertation, single-source-precursor (SSP) method will be applied to obtain our precursors to derive the final materials as depicted in Figure 2.6. SSPs, namely the molecular complexes contain all of the necessary elements required to make the specific inorganic material, which was originally developed for the CVD of semiconductor films and converted to the solution synthesis of nanomaterials by thermally induced decomposition reactions.<sup>90</sup> The SSP approach is especially advantageous for the synthesis of multiple nanomaterials, where the properties and the nanostructure can be tuned from the precursor design.<sup>91</sup> In addition, various of different nanostructures (nanotubes and nanoflowers) with different architectures have been also reported.<sup>92,93</sup> Further, most of SSPs are nontoxic and air-stable, making SSPs easier to convert into specific nanomaterials.<sup>94</sup>

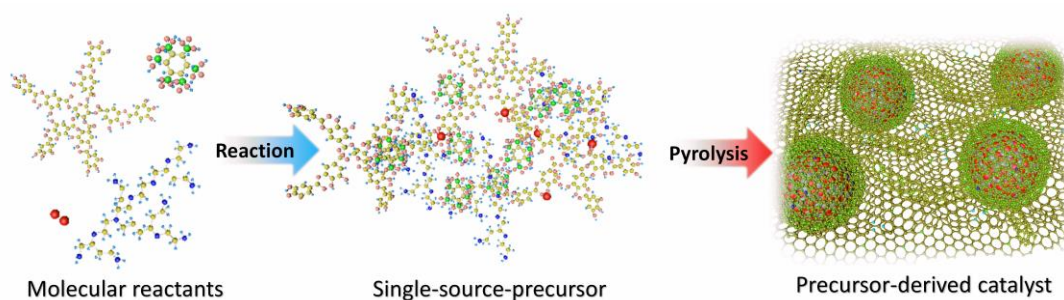


Figure 2.6 Schematic illustration of synthetic route of the precursor and TMCs/carbon hybrid via single-source-precursors approach.

## 2.4 Strategies for improving performance

Generally speaking, the strategies for improving electrocatalytic activity of the TMCs/carbon nanomaterials can be classified into two categories according to the different principals. The first one is to expose more available active sites on electrocatalyst surface through constructing special geometrical structure, which possesses a larger specific surface area. The other is to improve the intrinsic activity active species through composition regulation such as modulation of the electronic structure, tuning binding energy and desorption of intermediates, promotion the synergetic effects et al., which could further improve the catalytic activity and stability.

### 2.4.1 Nanostructure engineering

In recent years, various nanostructure engineering strategies, such as highly porous and core-shell structures, have been applied to improve the activity and stability of the electrocatalysts. In additionally, quantum dots (QDs) particles are fabricated to improve the atomic efficiency and interface area of transition metal compounds and enhance the performance of the electrocatalysts.

## Core-shell nanostructure design

Core-shell nanostructures are defined as composites consisting of cores (inner material) and shells (outer layer material) on the nanoscale. As electrocatalysts for water splitting, they require good conductivity, thus the carbon shell of such electrocatalysts is favourable for transition metals compounds, like alloys and phosphides in present dissertation. This outer carbon/graphene shell are typically *in-situ* formed during the high temperature pyrolysis, which can feasibly modify the electronic/chemical configurations of the interface. As shown in Figures 2,7a and 2.7b, the calculated  $\Delta G$  diagram and the dependence of  $\Delta G(H^*)$  on the measured current of different catalyst, indicating the CoNi alloy and the N-doped graphene shell exhibited low HER activity due to the excessively strong and weak adsorption of  $H^*$ , respectively. On the other hand, the graphene shells of CoNi@C demonstrated a high HER activity as the  $\Delta G(H^*)$  value is efficiently adjusted by the enclosed CoNi cluster.<sup>41</sup>

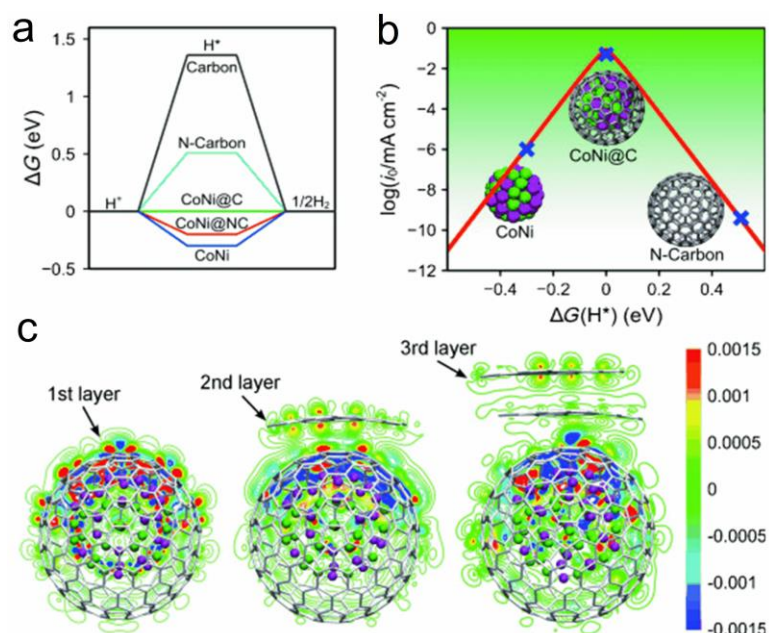


Figure 2.7 (a) Gibbs free energy ( $\Delta G$ ) profile of the HER on various catalysts, (b) volcano plot of the polarized current ( $i_0$ ) versus  $\Delta G(H^*)$  for CoNi cluster, CoNi@C, and N-doped graphene shell, and (c) redistribution of the electron densities after the CoNi clusters have covered by one to three layers of graphene. Adapted from Ref. [41]

Furthermore, engineering on core-shell nanostructures serve as the key to promote long-term durability in corrosive electrolytes. Studies have also indicated that the thickness of the carbon shell is crucial for the stability enhancement and activity improvement.<sup>41,95</sup> Further increases in the thickness of the carbon shell hinder the electron penetration effect between the inner CoNi and the carbon shell, leading to decreased activity. DFT calculations further reveal that the exceptional activity resulted from the heightened electronegativity of the graphene shell caused by electrons penetrating from the CoNi



core as shown in Figure 2.7c, which can reduce the H adsorption free energy of the graphene shell and promoted essential hydrogen adsorption for the HER further improve the performance.

### Porous structure engineering

The presence of a porous structure gives materials specific characteristics such as increased exposure of active sites and improved mass and charge transfer. Therefore, efforts are needed to design nanocarbons with excellent surface properties to host and facilitate the TMCs, enhancing the electrocatalytic performance. In recent years, carbons with hierarchical pores obtained by template-assisted methods have offered insights into designing and controlling porous nanocarbon materials for energy conversion applications.<sup>96</sup> For example, Tian and co-workers used an *in-situ* templates etching method to prepare three-dimensional interconnected Fe-N doped hierarchical porous carbon materials,<sup>97</sup> where Fe<sub>2</sub>O<sub>3</sub> nanoparticles served as templates to construct the hierarchical porous structure through an *in-situ* citric acid etching process. Apart from the template-assisted route, the carbonization of microporous MOFs is another promising method for preparing TM and porous carbon hybrids. Yin et al. synthesized a porous Co-N-C catalyst through the calcination of MOFs,<sup>98</sup> where the porous MOF was directly converted into porous N-doped carbon support for the TM compounds. Based on a similar mechanism, some other porous carbon-based electrocatalysts have also been developed through MOFs pyrolysis. The commonly used strategies for pore structure construction are shown in Figure 2.8.



Figure 2.8 Scheme of different synthesis methods of porous materials.

### Particle size controlling

Studies have shown that single atomic particles, clusters, and quantum dots with small sizes exhibit greater catalytic activity compared to their bulk counterparts. This is because reducing the size and thickness of particles increases the density of active edge sites and exposes more active surface atoms due to the small size effect of nanomaterials. For example, MoS<sub>2</sub> quantum dots have been found to

---

---

possess a greater number of active sites and exposed surface atoms compared to MoS<sub>2</sub> nanosheets, as demonstrated through research.<sup>99</sup> The presence of active corner and edge sites is responsible for reducing overpotential and increasing the current density of the electrocatalyst. Overall, a smaller size of a catalyst provides a number of advantages over its bulk counterpart, including increased surface area, greater electrolyte/catalyst contact area, and shorter electron transfer pathways, all of which can lead to improved catalytic performance. Studies suggest that the impact of size in electrocatalysis goes beyond simply considering the surface area.<sup>100,101</sup> Within the scientific framework, it is important to acknowledge that the size effect can be linked to the surface chemistry or electronic structure of electrocatalysts.

#### **2.4.2 Intrinsic activity improvement**

The intrinsic activity of electrocatalysts can be regulated by manipulating the atomic arrangements around active sites and optimizing the binding energies of adsorbate intermediates through changes in the electronic structures of active sites. As a result, activity can be improved. In this section, two local structure modification strategies, metallic/non-metallic heteroatom doping and heterostructure effect will be introduced.

##### **Metallic/non-metallic elements doping**

Doping engineering is a common technique used in the electrocatalytic water splitting process. It is mainly used to adjust the electronic structure, enhance electronic conductivity, and create more active sites. Metallic elements doping has studied in both theoretical and experimental way,<sup>102</sup> the surface modification of Mo and P on FeCo (110) caused the electronic hybridization and the relocation of the electrons of original FeCo, which can influence the H intermediates adsorption during HER process. Another research studied the influence of Mo incorporation of a NiMo solid solution, indicating a significantly improved HER activity originates from collective contribution of both phase and surface defects caused by Mo introduction.<sup>103</sup>

Furthermore, heteroatom-doped carbon materials have also been found to be efficient electrocatalysts. Non-metal elements such as N, P, S, and B are commonly used to modify the structural and electrical properties of nanocarbon materials. For example, N-doped carbon has been explored as an electrocatalyst, the introduction of N atoms into the carbon lattice can change the electronic configuration and electric conductivity of inert carbon. The different N species formed within the carbon matrix can improve electrocatalysis, particularly pyridinic N and pyrrolic N. There are also several studies that use DFT calculations(Figure 2.9a and 2.9b) to explain the positive effect of N species on active transition metal compounds,<sup>40</sup> confirming that the orbital hybridization between pyridinic N and MoP can provide a suitable electronic structure for capturing a hydrogen atom/proton.

The charge density differences diagrams (Figure 2.9c) show the MoP superlattice donates electrons to neighbouring pyridinic-, pyrrolic- and graphitic-N, resulting the charge density decrease of Mo atoms to facilitate the adsorption of H<sub>2</sub>O molecules. Compared to single-heteroatom doping, multiple-heteroatom doping can create more active sites and result in higher activity. Double heteroatom N, P and N, S are the most common multiple-heteroatom dopants used in most of the studies to alter the electrical and structural properties of carbon.<sup>104,105</sup>

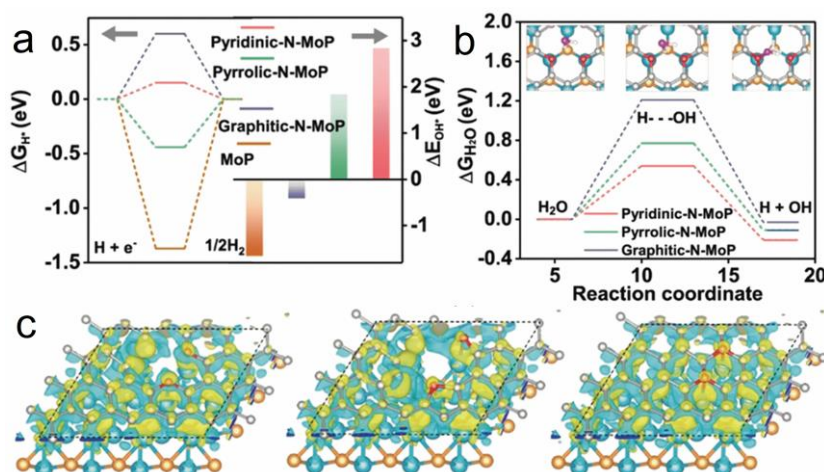


Figure 2.9 (a)  $\Delta G_{H^*}$  diagram and chemisorption energies of  $OH^*$  ( $\Delta E_{OH^*}$ ) of different catalyst configurations, (b) free energy diagram of the water dissociation step (inset: the atomic configurations of different states of pyridinic-N-MoP), and (c) the charge density differences in pyridinic-, pyrrolic- and graphitic-N-MoP interfaces, yellow and cyan regions represent electron accumulation and depletion, respectively. Adapted from Ref. [40]

## Heterostructure engineering

A heterostructure typically consists of two distinct components that are joined by interfaces. The most notable characteristic of these structures is the sudden change in chemical composition and crystal structure across the interface, which is responsible for many of the benefits of hetero-structured electrocatalysts. From a macroscopic viewpoint, the combination of different components at the interface can lead to electronic interactions and potential synergistic effects. On a microscopic level, the alteration in chemical composition and crystal structure leads to unique atomic coordination and lattice strains at the interface, opening up exciting possibilities for creating advanced hetero-structured electrocatalysts. Take TMCs/carbon hybrid materials as an example, the structural merits (Figure 2.10) of heterostructured catalysts are as follows:

- 1) Synergetic effect between highly active materials and conductive carbonaceous substrate can greatly improve the performance;<sup>106</sup>
- 2) Confinement effect can significantly mitigate the agglomeration issues of TMCs to increase the number of active sites and to preserve active sites during electrocatalysis;<sup>107</sup>

- 3) Interfacial bonding effect can modify the electronic structure of active sites and construct specific atom moieties such as Metal-N-C moieties;<sup>108</sup>
- 4) Strain effect between two phases can influence the binding energies of intermediates,<sup>109</sup>
- 5) Electronic interaction on the interface modulates the electron density around the active sites.<sup>110</sup>

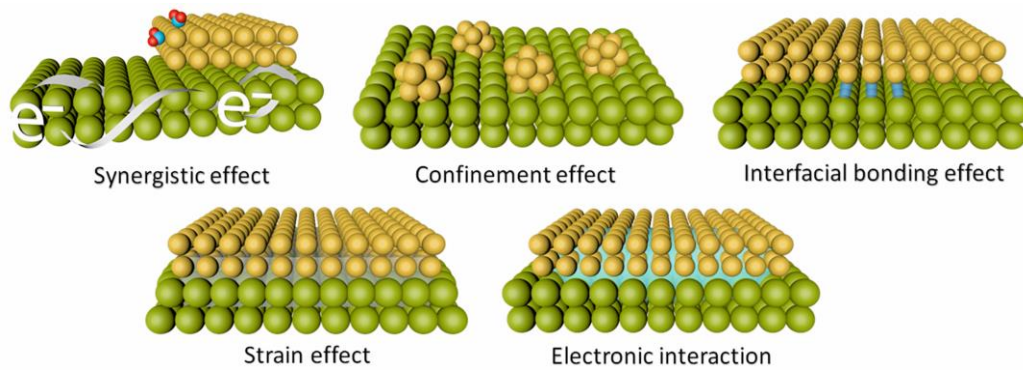


Figure 2.10 Schematic illustration of promotion effects originating from heterostructure engineering.

---

---

### 3 Results and Discussion

---

This chapter mainly summarizes and discusses scientific findings published in our research articles with the following three topics:

Topic 1: A highly active OER electrocatalyst comprised of defective carbon shell encapsulated metal (Fe, Co, Ni) nanoparticles and their alloys supported on *in-situ* formed N-doped graphene/carbon nanotube hybrid is synthesized from novel SSPs. The precursors are synthesized by a facile one-pot reaction of tannic acid with polyethylenimine and different metal ions. The further optimized catalyst shows excellent OER activity and stability performance.

Topic 2: Core-shell structured transition metal (Fe and/or Ni) phosphide nanoparticles dispersed and immobilized in a highly defective N and P co-doped carbon matrix are prepared via facile and cheap SSPs pyrolysis route and used as highly active and durable heterostructured electrocatalyst. The synthesized core-shell material displays promising electrocatalytic performance for both HER and OER.

Topic 3: By utilizing the facile and eco-friendly SSPs route, nanosized nitrogen/phosphorus co-doped carbon and CNTs encapsulated MoP quantum dots (QDs) hybrid material (MoP@NPC/CNT) is synthesized as high-performance electrocatalyst toward HER over a wide pH range. The physical characterization and electrochemical HER performances are demonstrated in this section.

#### 3.1 Single-source-precursor derived transition metal alloys embedded in nitrogen-doped porous carbons as efficient oxygen evolution electrocatalysts

The content of this chapter is published in:

**Chen, Y.,** Tian, C., Jiang, T., Maheu, C., Hofmann, J. P., Molina-Luna, L., Riedel, R. & Yu, Z. Single-Source-Precursor Derived Transition Metal Alloys Embedded in Nitrogen-Doped Porous Carbons as Efficient Oxygen Evolution Electrocatalysts. *ChemPlusChem* 87, e202200338 (2022). © Wiley

The overall synthesis procedure of the precursors and final nanomaterials is schematically shown in Figure 3.1. The precursors were fabricated by a one-pot self-assembly of tannic acid (TA), polyethylenimine (PEI) and transition metal ions (TMIs). TA provides polydentate ligands for different metal ions due to its luxuriant phenolic hydroxyl groups. The characteristic Raman lines of the chelated TA-metal ions in the as-prepared precursor are shown in Figure 3.2a. The peak located at  $523\text{ cm}^{-1}$  is attributed to the formation of the bidentate chelation between metal ions and phenolic oxygen of the catechol.<sup>111,112</sup> The peaks around  $1353$  and  $1487\text{ cm}^{-1}$  are assigned to catechol complex ring vibrations,<sup>113</sup> indicating that the metal ions are successfully coordinated by TA. Moreover, the chemical reaction between the catechol groups in TA and the amine groups in PEI through Michael addition and/or Schiff base reaction was expected to occur for *in-situ* introducing nitrogen heteroatoms into

the carbon-based precursors in the present study.<sup>114,115</sup> Therefore, Fourier-transform infrared spectroscopy (FTIR) was used to characterize the chemical structures of the as-prepared precursors and the typical bands for TA and PEI are denoted and shown in Figure 3.2b.<sup>116,117</sup> The broadness and distortion of the peak around  $1716\text{ cm}^{-1}$  assigned to TA quinone groups strongly suggest the formation of Schiff base products which were generated by Schiff base reaction through the catechol functional group of TA and amino groups from PEI.<sup>114,115</sup> And the absorption peak at  $1486$  and  $1585\text{ cm}^{-1}$  corresponding to C-N and C=N stretching further evidences the occurrence of Michael addition and Schiff base reaction between catechol functional group and amino groups.<sup>118</sup> In these cases of above-mentioned reactions, the possible bonding structure of the prepared precursor was show in Figure 3.1.

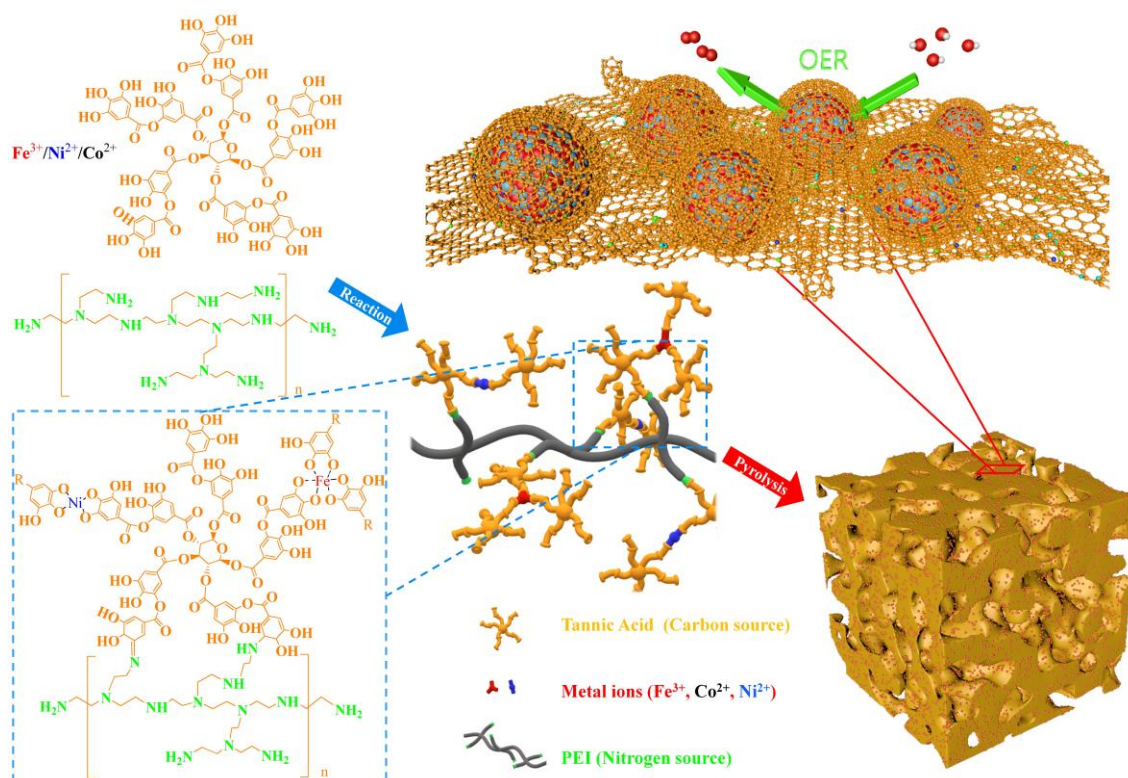


Figure 3.1 Schematic illustration of the synthetic route of the precursor and carbon shell encapsulated FeNi alloy nanoparticles supported on *in-situ* formed N-doped graphene/carbon nanotube hybrid.

Subsequently, the metal alloy nanoparticles encapsulated by nitrogen-doped carbon, namely FeCo@NC, FeNi@NC, and CoNi@NC were obtained by carbonization of the precursors in argon atmosphere at different temperatures for 3 h. For comparison, the single metal samples Fe@NC, Ni@NC and Co@NC were also prepared under the same condition. During the cross-linking process, different metal ions and PEI were evenly bonded by the catechol groups from TA, which effectively hinders the metallic particles from heavily aggregation during the pyrolysis. Various characterization methods were applied to verify the uniform presence of nitrogen and well-dispersed metal alloy nanoparticles in the supporting carbon substrates.

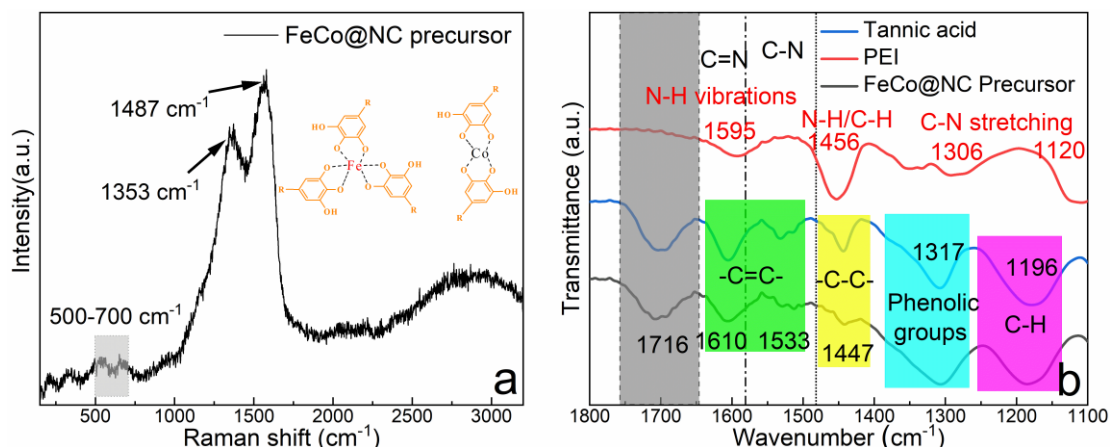


Figure 3.2 (a) Raman spectrum and (b) FT-IR spectra of FeCo@NC precursors, TA, and PEI.

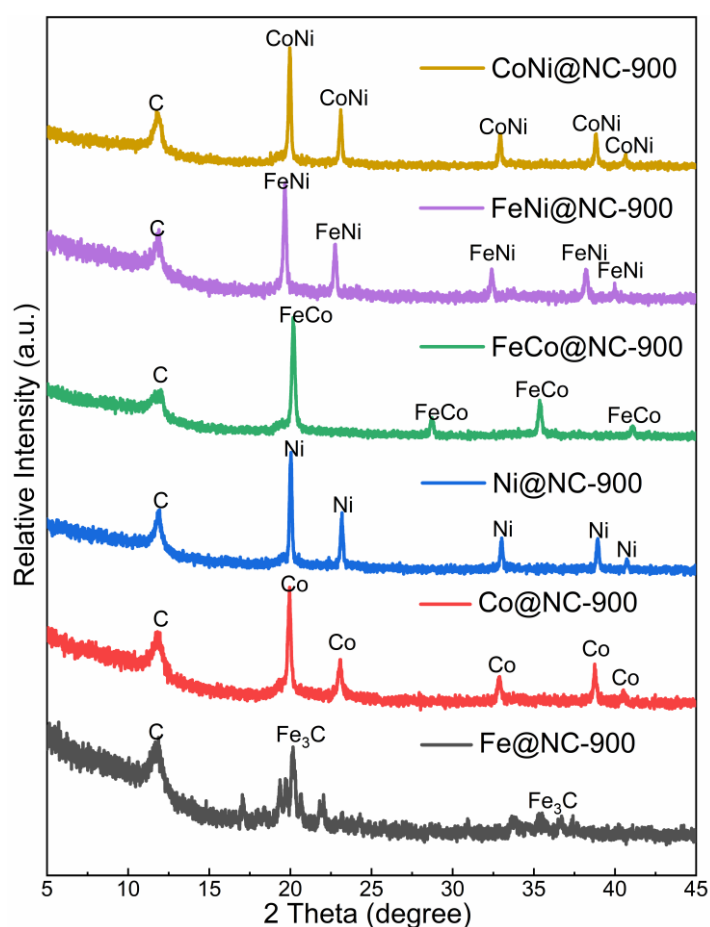


Figure 3.3 XRD patterns of different synthesized metallic core-shell compounds.

The powder X-ray diffraction (XRD) patterns of different samples (Fe@NC-900, Co@NC-900, Ni@NC-900, FeCo@NC-900, FeNi@NC-900, CoNi@NC-900) are shown in Figure 3.3. Characteristic reflections of different metal alloys are identified. The XRD patterns of FeNi@NC-900 display diffraction peaks at  $19.6^\circ$ ,  $22.7^\circ$ , and  $32.4^\circ$ , indexed to (111), (200), and (220) planes of the FeNi alloy (JCPDS No. 47-1417). The broad peak at around  $12.2^\circ$  for all the samples is attributed to the (002) crystal plane of graphitic

carbon, which is broadened and slightly shifted to lower angle due to the presence of nitrogen heteroatom and different carbon morphologies. The carbon derived from the organic precursors coexists in different morphologies such as graphitic carbon, carbon nanotubes and amorphous carbon, which can be manifested by Raman spectroscopy and by high-resolution transmission electron microscopy (HR-TEM) results as well. In the case of the synthesized FeCo@NC-900 and CoNi@NC-900 core-shell materials, the FeCo and CoNi alloys are also identified by their characteristic diffraction peaks. In addition, Fe<sub>3</sub>C and metallic Ni and Co are found in the XRD pattern as single metal encapsulated in the carbon support, which is consistent with the HRTEM results discussed below.

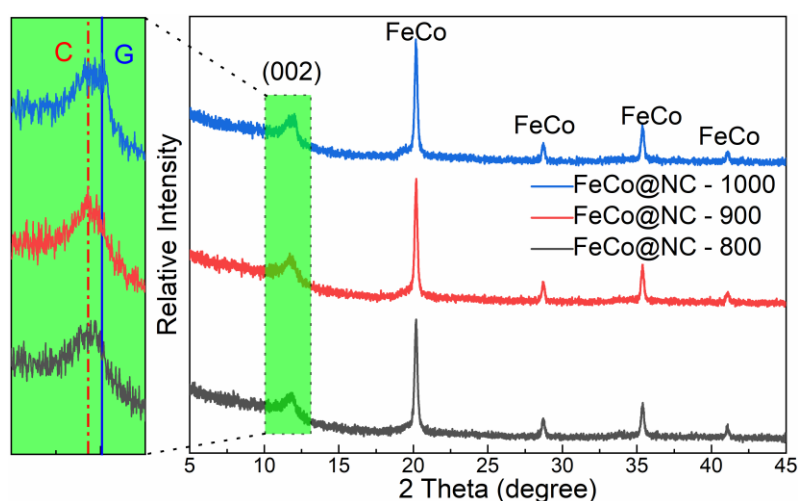


Figure 3.4 XRD patterns of the FeCo@NC precursor carbonized under different temperatures.

The carbonization temperature is considered as a key factor for the precursor pyrolysis. As an example, the XRD patterns of FeCo@NC obtained at different carbonization temperatures are shown in Figure 3.4. The intensity of the carbon (002) diffraction peak increases gradually with the increase of the temperature from 800 to 1000 °C, suggesting that the sample prepared at higher temperature undergoes increasing structural ordering. However, there is negligible influence on the metallic compounds with increasing carbonization temperature. Noteworthily, those samples containing nickel exhibit a sharp carbon peak, which relates to the stronger catalytic effect of Ni on the pyrolysis of the carbon precursor as compared with that of Fe and Co.<sup>119</sup>

The morphology of the carbonized materials was characterized by field emission scanning electron microscopy (FE-SEM) and HR-TEM as shown in Figure 3.5. Taking the sample FeNi@NC-900 as a reference, the FE-SEM images show rough surfaces with pores. And from the enlarged images of sample FeNi@NC-900, a large amount of highly exposed and homogeneously dispersed nanoparticles with bright contrast are found all around the surface of the carbon matrix with a similar diameter, which are indexed as FeNi alloy. The average size of the particles is around 50 nm without obvious aggregation, which is greatly hindered by the pyrolysis of the as-prepared single-source-precursor



derived from the facile molecular reaction between metal ions and tannic acid. The well-dispersed nanostructures have a positive effect on the electrocatalysis due to a high charge and mass transfer between electrolyte and active sites of the metal alloy. Furthermore, the energy dispersive X-ray spectroscopy (EDS) elemental mapping images show a uniform distribution of Fe and Ni in the carbon support without any phase segregation and with uniform distribution of nitrogen. The presence of nitrogen in carbon introduces defects and modifies the electronic structure of the carbon matrix. Besides, EDS patterns for the sample FeNi@NC-900 are shown in Figure 3.5h. The atomic percentage of the elements in the samples is calculated from the relative intensities of the peaks corresponding to C, N, Fe and Ni in the EDS spectra, and the results indicate that the compositions of Fe and Ni are in good agreement with the theoretical value 1:1. The FeNi content of sample FeNi@NC-900 was measured by ICP-OES, which amounts to 10.23 wt.%. The average atomic ratio of Fe and Ni is 0.995, which is accordant with the value obtained by SEM-EDS analysis.

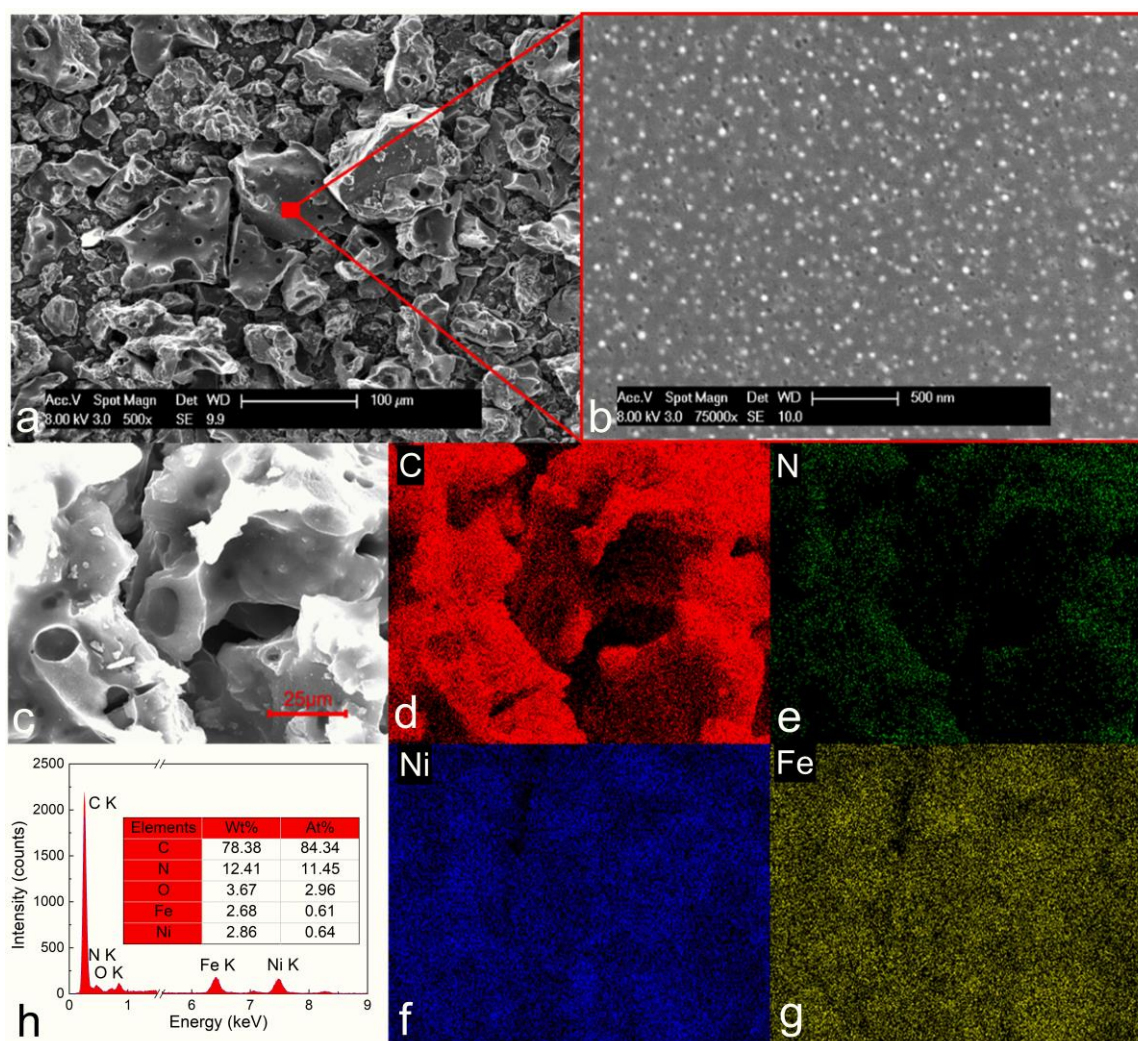


Figure 3.5 (a) Low-magnification FE-SEM images, (b) high-magnification FE-SEM image of sample FeNi@NC-900, (c-g) SEM-EDS images, and (h) EDS spectrum of sample FeNi@NC-900.

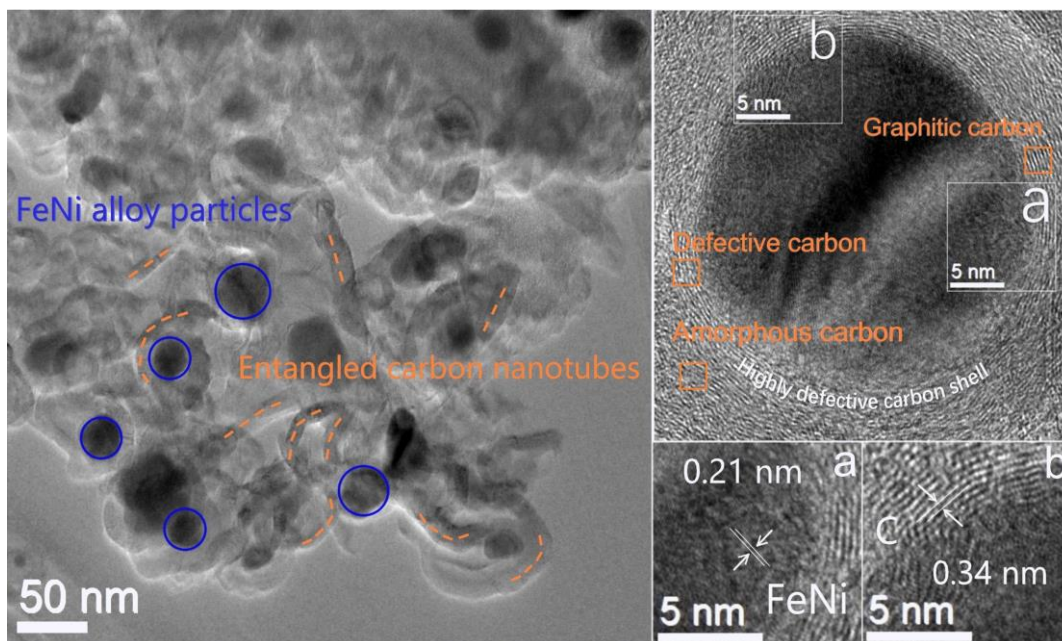


Figure 3.6 TEM and HRTEM images of sample FeNi@NC-900.

The detailed microstructure of sample FeNi@NC-900 was also characterized by TEM as shown in Figure 3.6. The clusters are composed of different carbon morphologies such as highly defective carbon, amorphous carbon and graphitic carbon. The images show that the darker alloy nanoparticles are well encapsulated by a highly defective carbon shell and wrapped by CNTs. The observed lattice spacings are 0.21 nm and 0.34 nm, corresponding to FeNi alloy and carbon, respectively.<sup>120</sup> It is noteworthy that numerous bent CNTs entangle with each other in the cluster and attach to the metallic particles, formed during pyrolysis of the organic precursors by their catalytic activity. It is well-accepted that CNTs are *in-situ* formed in the presence of the catalysis of metallic nanoparticles.<sup>121</sup> The yield of sample FeNi@NC-900 is about 56.4%, which is the highest one compared with those of samples FeCo@NC-900 (47.6%) and NiCo@NC-900 (54.6%). This may be caused by the superior catalytic effect of FeNi alloy on organic carbon species capture and conversion during pyrolysis. Interestingly, the size of the nanoparticle has an influence on the formation of the CNTs, and a metallic particle size lower than 50 nm is capable to catalyze CNTs growth but do not simply deposit on the surface.<sup>122</sup> Owing to the *in-situ* formed nanotubes, rapid electron transfer between the carbon matrix and alloy nanoparticles is promoted, which is expected to manifest the elevated activity of the catalyst. The TEM images clearly show that the diameter of the nanoparticles is around 50 nm which is also evidenced by the SEM image (see Figure 3.5b). It can be taken from the HR-TEM images (Figure 3.6), that the nanoparticles are well-protected by a defective carbon shell. Such a morphology and structure configuration can not only speed up the reactants transfer but also ensure a better electronic conduction throughout the support. Based on the above analysis, the results indicate that the transition metal FeNi alloy nanoparticles are strongly coupled with nitrogen-doped carbon shells together with entangled carbon nanotubes, which

are advantageous to induce enhanced activity for catalytic reactions.

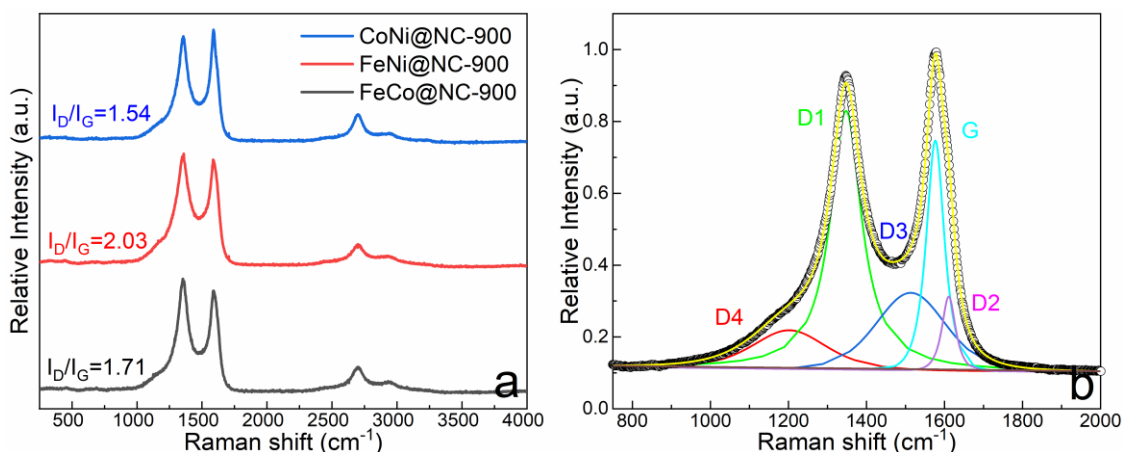


Figure 3.7 (a) Raman spectra of samples FeCo@NC-900, FeNi@NC-900 and CoNi@NC-900, and (b) the peaks fitting plot of FeNi@NC-900.

To further gain insight into the carbonaceous material, Raman spectroscopy was employed. As shown in Figure 3.7, the observed peaks located at 1340 and 1591 cm<sup>-1</sup> are clearly present in all the different samples, corresponding to the D and G bands of carbon.<sup>123,124</sup> Compared with different metal combinations, the FeNi@NC-900 sample has the highest ID/IG ratio up to 2.03, indicating the highest disordering of carbon. And Lorentzian–Gaussian function curve fitting was done for the FeNi@NC-900. According to the fitting results, clear D4, D3 and D2 bands are superimposed in the peaks, which are caused by impurity, amorphous carbon and structure disordering, respectively.<sup>125</sup> Based on the ratios of ID/IG, the FeNi@NC-900 possesses a highly defective graphitic structure, which results from the heteroatom nitrogen in carbon. Compared to the FeCo@NC-900 and CoNi@NC-900 samples, the highly defective structure in the FeNi@NC-900 are conducive for charge transfer and may expose more accessible catalytically active sites. Thus, an enhanced electrocatalytic performance is expected for the FeNi@NC-900 sample.

The chemical states of Fe, Co, Ni, C, and N were investigated by X-ray photoelectron spectroscopy (XPS). The full XPS survey spectrum shown in Figure 3.8 clearly reveals the coexistence of all the mentioned elements in the as-prepared materials, which agrees well with the EDS mapping results. According to the high-resolution N 1s XP spectrum, four types of N species are deconvoluted from the spectrum, including pyridinic-N (398.7 eV), pyrrolic-N (400.0 eV), graphitic-N (401.2 eV), and pyridine oxidized-N (403.3 eV). It is generally accepted that an improvement of the OER catalytic performance results from high-density electron-withdrawing functional groups like pyridinic motifs,<sup>126,127</sup> moreover, pyridinic N and pyrrolic N play a key role to coordinate Fe ions to form M-N-C species,<sup>128,129</sup> which is a potential electrocatalytic alternative to OER owing to satisfactory physical and chemical characteristics. The chemical states of Fe and Ni species in the catalyst FeNi@NC-900 are shown in Figure 3.8. The Fe 2p

spectrum shows a major rough peak at a low combining energy of around 706 eV, corresponding to  $\text{Fe}^0$ . The other bands centred at 710, 713, 725 and 727 eV can be assigned to  $\text{Fe}^{2+}$  and  $\text{Fe}^{3+}$  species, which are probably due to the surface oxidation of the metallic alloys. It is worth mentioning that the bonding energy of metallic zero-valent Fe is shifting to lower energy. Likewise, two rough peaks in Figure 3.8d with binding energies of about 855 eV is correlated with the di-valent state of Ni, which are also ascribed to the surface oxidation of the metallic nanoparticles. The formation of  $\text{Ni}^0$  in sample  $\text{FeNi@NC-900}$  can be also confirmed by the peaks located around 853 eV.<sup>127,130</sup> The shift of the bonding energy of  $\text{Fe}^0$  and  $\text{Ni}^0$  evidences the change of the electronic structure by alloying Fe with Ni,<sup>131,132</sup> which results in more active sites for the electrochemical process.

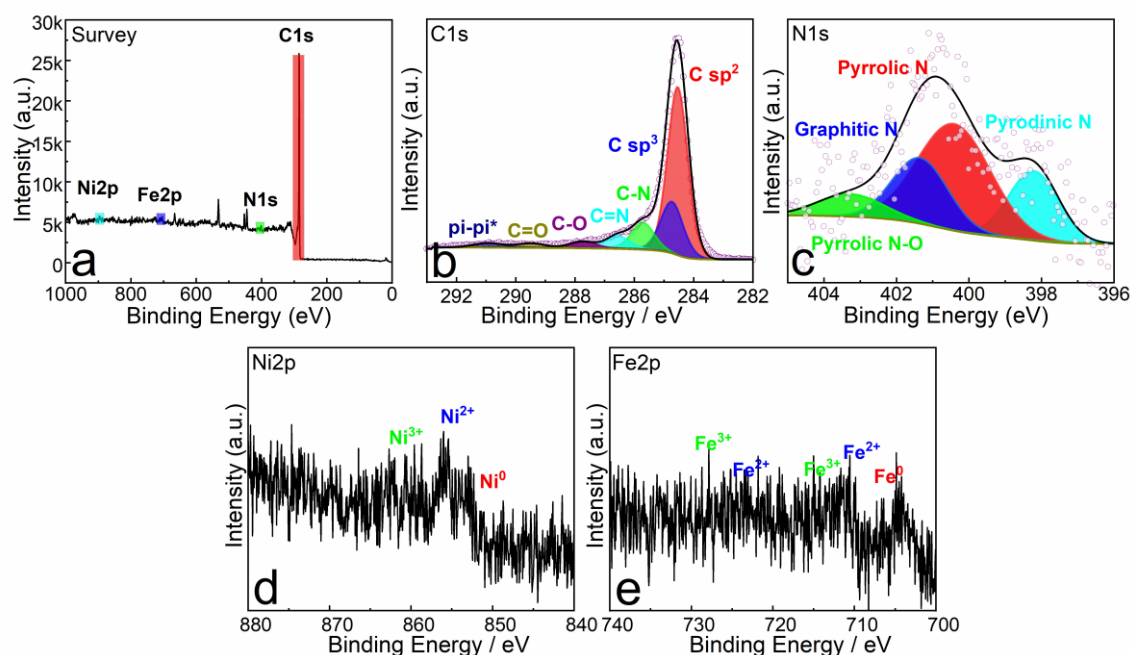


Figure 3.8 XPS data for sample  $\text{FeNi@NC-900}$ : (a) Survey spectrum, (b) C 1s, (c) N 1s, (d) Ni 2p, and (e) Fe 2p region scans.

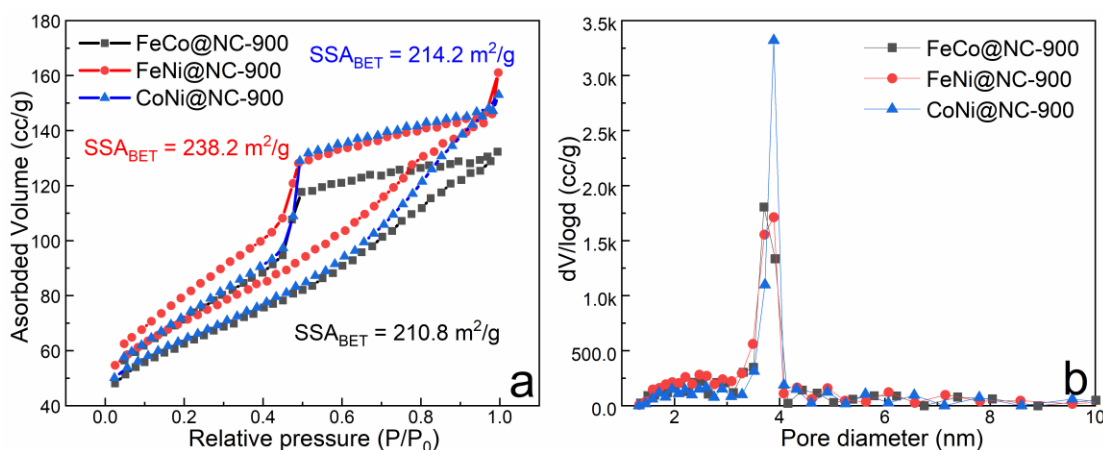


Figure 3.9 Nitrogen physisorption data: (a) isotherms and (b) pore size distribution of different samples.

Figure 3.9 reveals the N<sub>2</sub> adsorption–desorption isotherms showing the specific surface areas and pore structure of all samples. Type-IV adsorption isotherms are analyzed for all the samples, which are a typical feature of a mesoporous structure. The FeNi@NC-900 possesses the biggest BET specific surface area (SSA) around 238.2 m<sup>2</sup> g<sup>-1</sup>. And the pore size is mainly centred at around 4 nm. The measured SSAs of the FeCo@NC-900, FeNi@NC-900, and CoNi@NC-900 amount 210.8, 238.2, and 214.2 m<sup>2</sup> g<sup>-1</sup>, respectively. Such high SSAs are advantageous for interfacial reactions and mass transport, which is favoured for accessing more active sites towards electrocatalytic reaction.

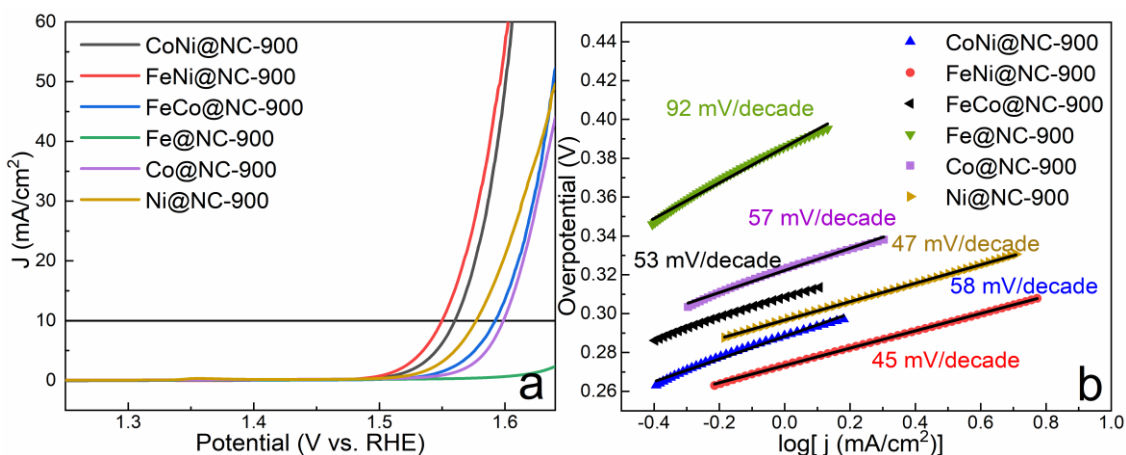


Figure 3.10 The OER performance of the synthesized core-shell samples including (a) polarization curves and (b) Tafel plots.

Table 3.1 Summary of OER performance of sample FeNi@NC-900 compared with previously reported FeNi-based catalysts.

Material	Electrolyte	Loading amount	Potential <sup>a</sup> (V vs. RHE)
FeNi/NC <sup>133</sup>	1 M KOH	0.566 mg cm <sup>-2</sup>	1.58 V
FeNi/NCNT <sup>133</sup>	1 M KOH	0.566 mg cm <sup>-2</sup>	1.62 V
FeNi-NCF-800 <sup>130</sup>	1M KOH	0.225 mg cm <sup>-2</sup>	1.547 V
FeNi@N-CNT/NCSS <sup>120</sup>	1 M KOH	>0.25 mg cm <sup>-2</sup>	1.54 V
FeNi@NC-NG <sup>134</sup>	1 M KOH	0.5 mg cm <sup>-2</sup>	1.50 V
FeNiNCFs <sup>130</sup>	1 M KOH	0.255 mg cm <sup>-2</sup>	1.547 V
FeNi/NC <sup>135</sup>	1 M KOH	0.337 mg cm <sup>-2</sup>	1.528 V
fd-FeNi/C <sup>136</sup>	1 M KOH	0.382 mg cm <sup>-2</sup>	1.531 V
FeNiP/NPCS <sup>137</sup>	1 M KOH	0.25 mg cm <sup>-2</sup>	1.548 V
FeNi@CNTs <sup>138</sup>	1 M KOH	0.354 mg cm <sup>-2</sup>	1.549 V
<b>FeNi@NC-900<sup>our work</sup></b>	<b>1 M KOH</b>	<b>0.225 mg cm<sup>-2</sup></b>	<b>1.54 V</b>

<sup>a</sup> Potential at a current density of 10 mA cm<sup>-2</sup> (based on electrode geometric area).

The OER electrocatalytic activities of different samples carbonized at 900 °C were first evaluated by LSV in 1 M KOH aqueous solution. Figure 3.10a shows the corresponding LSV curves of the as-prepared working electrodes loaded with different catalysts at 5 mV s<sup>-1</sup>. It clearly displays that the FeNi@NC-900 exhibits the lowest overpotential of 310 mV at 10 mA cm<sup>-2</sup> (after *iR* correction), which is smaller than that of the other two different samples, namely FeCo@NC-900 (350 mV) and CoNi@NC-900 (330 mV). The results show that the sample FeNi@NC-900 exhibits the best OER performance. Different single metallic nanoparticles samples supported by carbon are also characterized, indicating that the order of electrocatalytic activity is as follows: Ni@NC-900 > Co@NC-900 > Fe@NC-900. In general, the samples containing alloys of the abovementioned metals possess improved activities than that of the single metallic ones based on the order of FeNi@NC-900 > Fe@NC-900/Ni@NC-900, CoNi@NC-900 > Ni@NC-900/Co@NC-900 and FeCo@NC-900 > Fe@NC-900/Co@NC-900. Besides, a comparison of the electrocatalytic activity between the present sample and other FeNi-based composite materials reported in the literature is shown in Table 3.1. The present FeNi@NC-900 sample exhibits most superior OER performance compared to recently reported FeNi-based electrocatalysts with a lower loading amount, suggesting a high application potential for electrocatalytic OER. It is assumed that the strong coupling between FeNi alloy and the different carbon morphologies including the CNTs and defective carbon shells are responsible for enhancing the electron and mass transfer, resulting in an excellent catalytic activity towards OER.

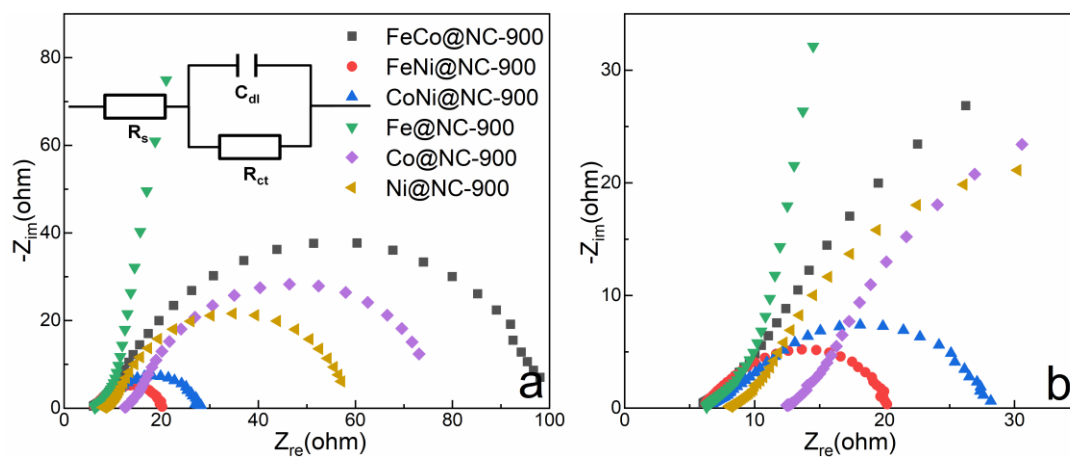


Figure 3.11 (a) OER EIS spectra of different samples (recorded at 1.56 V vs. RHE) and (b) impedance spectra in the higher frequency range (Color code is same in both plots).

Furthermore, Tafel plots were derived from LSV data given above to investigate the OER reaction kinetics and the results are shown in Figure 3.10b. The slope values of samples FeCo@NC-900 and CoNi@NC-900 are higher than that of sample FeNi@NC-900 (45 mV dec<sup>-1</sup>). Due to the fact that a smaller Tafel slope corresponds to a higher catalytic activity, the superiority of sample FeNi@NC-900 with the lowest Tafel slope is again confirmed among the other samples. And it is worth noting that

the significantly increased OER activity of sample FeNi@NC-900 in comparison with that of the Ni@NC-900 and Fe@NC-900 again indicates the positive role of the FeNi alloy for the electrocatalytic activity of the metal/carbon core shell samples.

The EIS study was conducted to further explore the interfacial charge transfer properties of different electrode reactions. Generally speaking, a smaller semicircle suggests a faster charge transfer kinetics. The Nyquist data are fitted by the equivalent circuit (inset of Figure 3.11a). The  $R_{ct}$  represents the charge transfer resistance in the OER process. The FeNi@NC-900 sample has the lowest charge transfer resistance comparing with our other samples which is consistent with the results of the Tafel plots. According to the literature,<sup>139</sup> the improved charge transfer ability is related to the higher electric conductivity of the hybrid material alloy@NC. It is assumed that the alloy nanoparticles encapsulated by the nitrogen doped carbon accelerate the electron transfer rate during the reaction process.

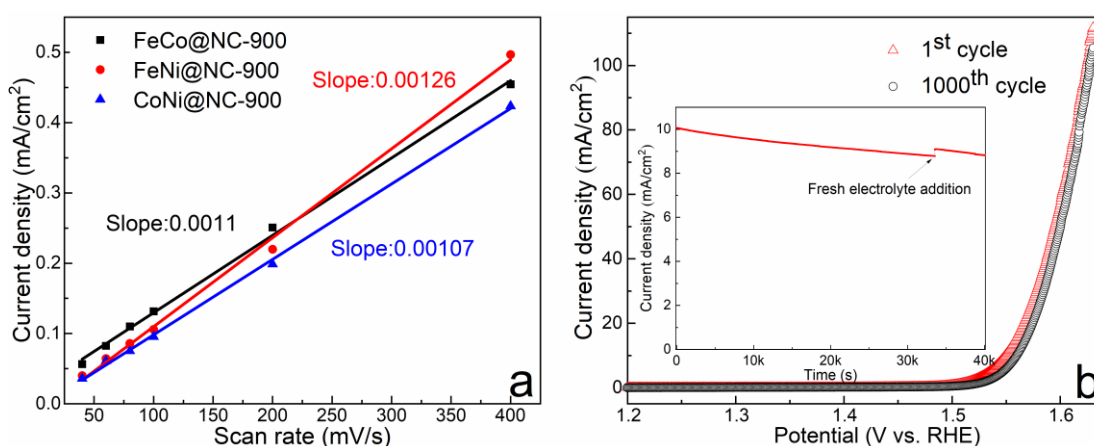


Figure 3.12 (a) Plots of the current density versus the scan rate of samples FeCo@NC-900, FeCo@NC-900 and CoNi@NC-900, and (b) Polarization curves before and after continuous 1000 CV cycles, the inset shows the chronoamperometric curve for sample FeNi@NC-900 at constant potentials.

Since the ECSA is generally proportional to the electrochemical  $C_{dl}$  of the electrocatalysts, the cyclic voltammetry measurements were carried out in non-Faradaic region to evaluate the ECSA. The  $C_{dl}$  values are shown in Figure 3.12a. The  $C_{dl}$  values of FeNi@NC-900, CoNi@NC-900, FeCo@NC-900 are 1.26, 1.10, and 1.07 mF cm<sup>-2</sup>, respectively. The FeNi alloy catalyst exhibits a higher ECSA than all the other alloy containing samples, suggesting a slightly higher electrocatalyst–electrolyte contact interface area than that of the other prepared catalysts. The indistinguishable difference in ECSAs of the compared samples are also consistent with the negligible difference of the BET surface area. Thus, the significant difference in catalytic performance of the prepared catalysts result from the different active sites and active components, suggesting that FeNi alloy has a better synergistic effect with the nitrogen containing carbon shell as compared with that of the other alloy@NC samples. And according with the literatures,<sup>140,141</sup> the surface electronic structure was positively altered by the combination of

FeNi alloys and N-doped carbon, which optimized the oxygen adsorption/activation energy for the OER.

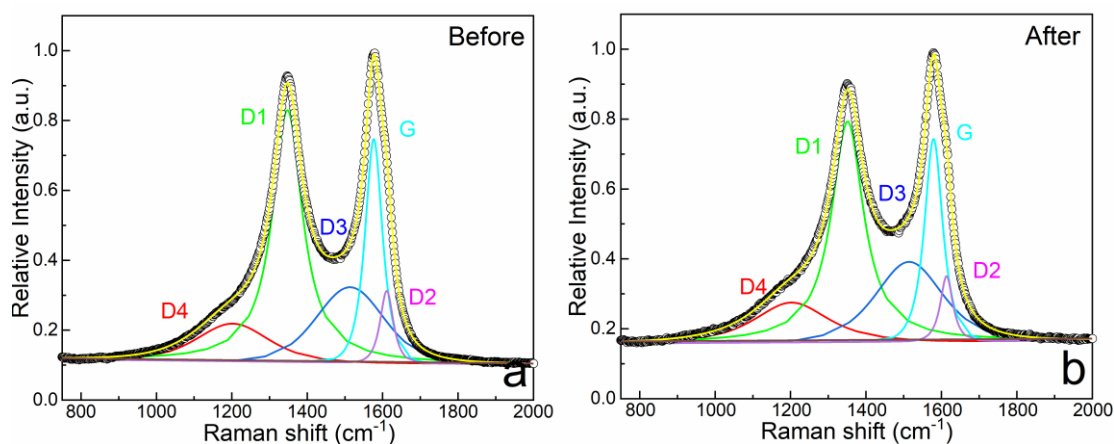


Figure 3.13 Raman peaks fitting of FeNi@NC-900 (a) before and (b) after stability test (Samples are denoted as FeNi@NC-900-before and FeNi@NC-900-after).

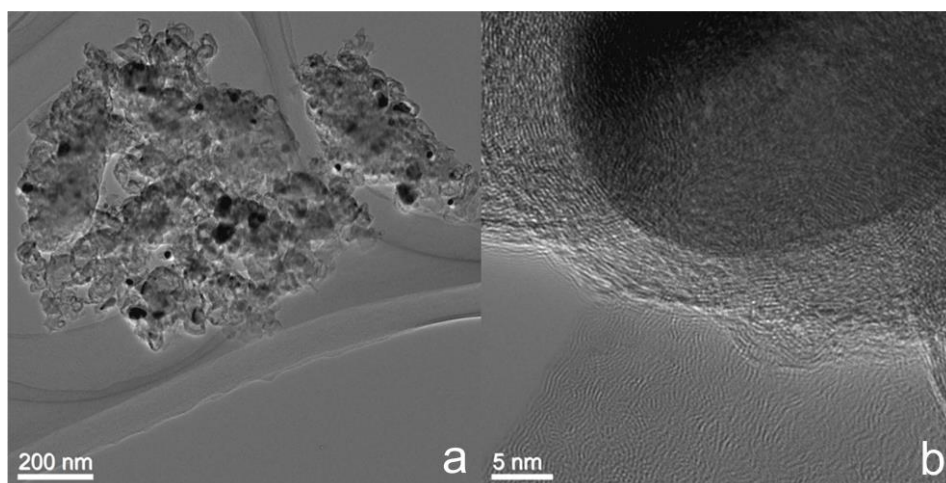


Figure 3.14 TEM images with (a) lower and (b) higher magnification of cycled FeNi@NC-900 (Denoted as FeNi-NC-900-after).

In addition to the superior electrocatalytic performance, the stability is another key factor for utilization of electrocatalysts. The stability of the as-prepared FeNi@NC-900 electrocatalyst was characterized by comparing the LSV curves before and after 1000 cyclic voltammetry measurements at a scan rate of  $100 \text{ mV s}^{-1}$  and the results are shown in Figure 3.12b. The overpotential shows slight change since only about 15 mV more is needed to drive  $10 \text{ mA cm}^{-2}$  compared with the initial curve. And it is noticeable that the difference is getting smaller and smaller at the region of high current density, suggesting stability of the FeNi@NC-900 sample. Minor corrosion of the active compounds and catalyst falling off can explain the slight increase of the overpotential after degradation test. Similarly, chronoamperometric tests were also carried out for measuring the stability of FeNi@NC-900 for more than 10 h. As shown in Figure 3.12b, a minor decay occurs after the test, indicating again an



excellent stability of the sample. The concentration decrease of the electrolyte is also responsible for the decrease of the current density during long-term durability test. The results suggest that the well encapsulated FeNi@NC-900 hybrids maintain superior catalytic activity for at least 10 h without serious decay.

The cycled catalyst was further characterized by TEM and Raman as shown in Figures 3.13 and 3.14, the core-shell structure of FeNi@NC-900-after is well-retained after stability test. Compared with the FeNi@NC-900-before, some changes of FeNi@NC-900-After were detected by Raman characterization, which is also fitted into five Lorentzian–Gaussian functions. The related fitting parameters and values for both FeNi@NC-900-before and FeNi@NC-900-after samples are listed in Table 3.2. The percentage of disordered carbon is slightly increased after test, indicating the decreasing areas proportion of peak G. Thus, it comes to conclusion that the nanomorphology of FeNi@NC-900 is highly retained, but undergoes a tiny increase of disordered carbon content after the stability test.

Table 3.2 Summary of Raman peaks fitting parameters for FeNi@NC-900-before and FeNi@NC-900-after.

Material	Adj. R-Square	Peak	FWHM	Area
<b>FeNi@NC-900-before</b>	0.999553	D4	222.04275	11.6019
		D1	96.5084	44.3317
		D3	209.12002	21.4315
		G	54.29695	18.2492
		D2	40.68583	4.38569
<b>FeNi@NC-900-after</b>	0.999534	D4	229.31913	13.28221
		D1	103.22025	41.83253
		D3	208.48006	23.42331
		G	56.69483	17.4917
		D2	39.0422	3.97024

### 3.2 Single-source-precursor derived Fe/Ni phosphide nanoparticles encapsulated in P/N-co-doped carbon as bifunctional electrocatalyst for hydrogen evolution reaction and oxygen evolution reaction

The content of this chapter is published in:

**Chen, Y.,** Jiang, T., Tian, C., Zhan, Y., Kempf, A., Molina-Luna, L., Hofmann, J. P., Riedel, R. & Yu, Z. Single-Source-Precursor Derived Binary FeNi Phosphide Nanoparticles Encapsulated in N, P Co-Doped Carbon as Electrocatalyst for HER and OER. *Energy Technology*, 2300233 (2023). © Wiley

The proposed preparation route of the SSPs and further derived TMPs encapsulated in nitrogen/phosphorus doped carbon with core-shell structure is presented in Figure 3.15. Firstly, the SSPs were fabricated via a one-pot reaction. Subsequently, the obtained SSPs were carbonized at 900 °C under Ar atmosphere to convert the transition metal ions and organic ligands into core-shell structured TMPs and corresponding N/P doped carbon matrix, respectively.

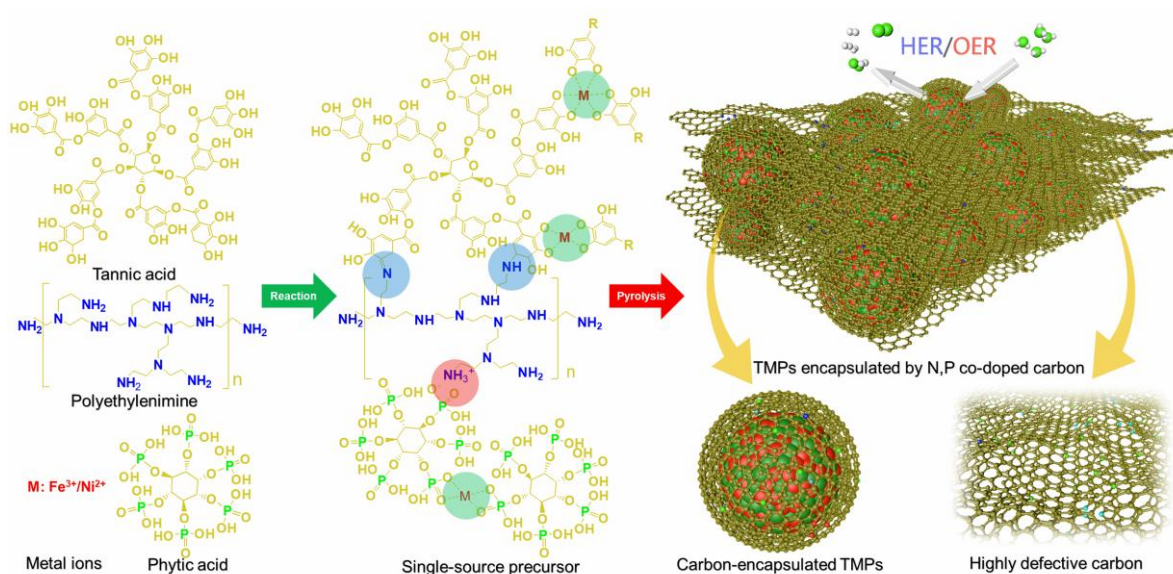


Figure 3.15 Schematic illustration of the applied route of precursor synthesis and the final TMP-based electrocatalyst derived therefrom.

During the reaction process, different reactions/interactions were involved, as follows: (i) Michael addition or/and Schiff base reaction between the amine group in PEI and the catechol units in TA,<sup>142</sup> which was proven by FTIR analysis of the FeNiP@NPC precursor shown in Figure 3.16a. The broadness and distortion of the peak around 1700 cm<sup>-1</sup> and the peaks at 1486 and 1585 cm<sup>-1</sup> indicate C-N and C=N stretching.<sup>114,115,118</sup> (ii) The absorption peaks centred at 965 and 1057 cm<sup>-1</sup> are assigned to the stretching of phytate anion linked with -NH<sub>3</sub><sup>+</sup>, originating from the ionic chelation between positively charged PEI and negatively charged phytic acid (PA).<sup>143</sup> (iii) The broad band at around 3000-3500 cm<sup>-1</sup> of the precursor becomes weaker and broader as compared with bare PA, suggesting the formation of

hydrogen bonding between PA and PEI.<sup>144</sup> (iv) The red shift from 1061 to 1024  $\text{cm}^{-1}$  is attributed to coordination interaction between transition metal ions and PA.<sup>145</sup> (v) Transition metal ions chelating with TA was proven by Raman spectra as shown in Figure 3.16b either in form of bidentate chelation or tridentate chelation.<sup>111,113,146</sup> Based on the above spectroscopic analysis, the SSP was successfully synthesised as shown in Figure 3.15. The details of mentioned reactions and bonding of SSPs fabrication are shown in Figure 3.17.

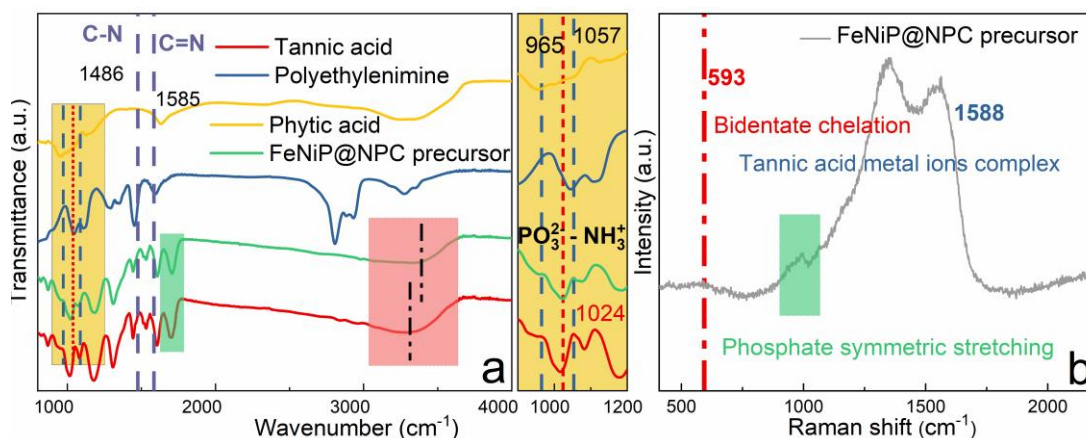


Figure 3.16 (a) FT-IR spectra of FeNiP@NPC precursors, TA, PA, and PEI, and (b) Raman spectrum of the FeNiP@NPC precursor.

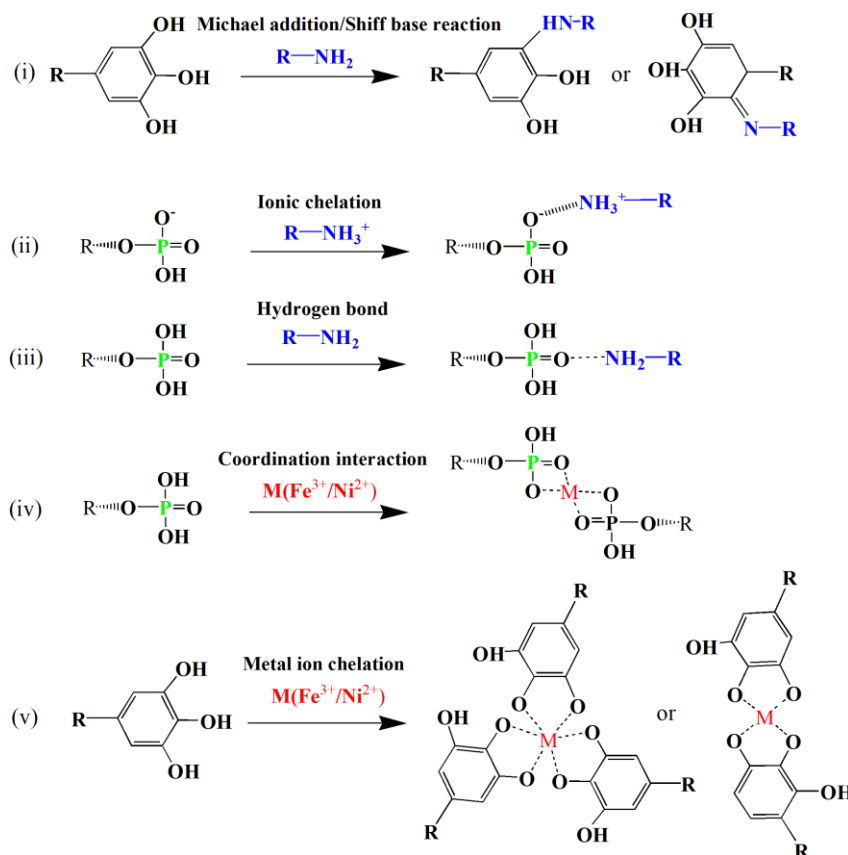


Figure 3.17 Schematic illustration of possible reactions related to the SSPs fabrication.

For a more in-depth comparison of the phase composition, the XRD pattern was used to characterize the FeP@NPC, NiP@NPC and FeNiP@NPC samples as shown in Figure 3.18a. The XRD pattern of FeP@NPC is comprised of the mixed-phase FeP and Fe<sub>2</sub>P as shown by the distinct characteristic reflections of hexagonal Fe<sub>2</sub>P (JCPDS#33-0670) and FeP (JCPDS#39-0809). The diffraction peaks of NiP@NPC are in good accordance with hexagonal Ni<sub>2</sub>P (JCPDS#03-0953). All the reflections of FeNiP@NPC are in consistence with both Ni<sub>2</sub>P (JCPDS#03-0953) and Fe<sub>2</sub>P (JCPDS#33-0670), indicating the presence (Ni<sub>x</sub>Fe<sub>1-x</sub>)<sub>2</sub>P solid solution or/and Ni<sub>2</sub>P/Fe<sub>2</sub>P mixture. From the literature,<sup>147</sup> the presence of Ni supresses the formation of orthorhombic FeP but facilitates the formation of (Ni<sub>x</sub>Fe<sub>1-x</sub>)<sub>2</sub>P solid solution, which is accordance with our results that there are no orthorhombic FeP peaks but only hexagonal Ni<sub>2</sub>P and Fe<sub>2</sub>P peaks found in the patterns of FeNiP@NPC. However, the same hexagonal crystal structure types of Ni<sub>2</sub>P and Fe<sub>2</sub>P facilitate the formation of (Ni<sub>x</sub>Fe<sub>1-x</sub>)<sub>2</sub>P. Therefore, the formation of the solid solution (Ni<sub>x</sub>Fe<sub>1-x</sub>)<sub>2</sub>P is expected in our study.<sup>148</sup> Besides the reflections from TMPs, a weak and broad peak at around 10.09° is found for all the XRD patterns, corresponding to carbon (002) with a relatively low graphitization degree. The peak position of the carbon (002) plane shifts to lower 2 Theta values due to the heteroatom P and N doping.<sup>149,150</sup>

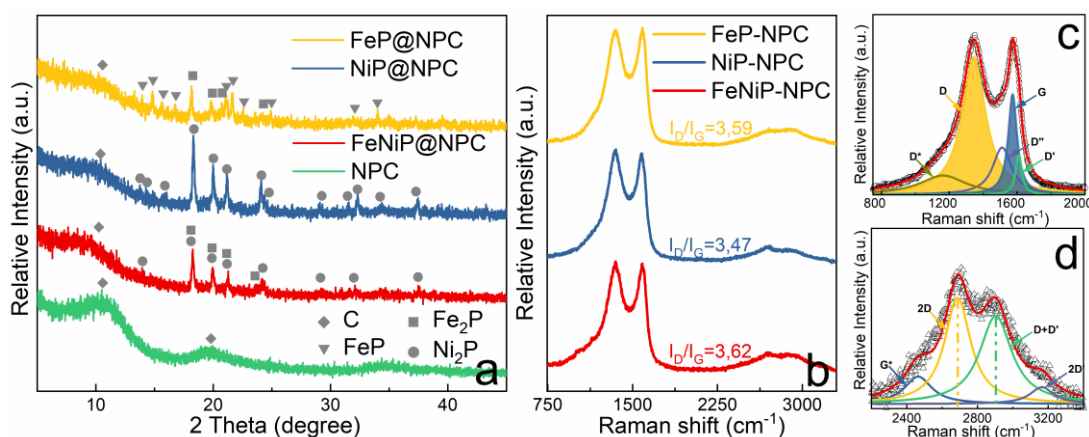


Figure 3.18 (a) XRD patterns of FeNiP@NPC, FeP@NPC, NiP@NPC, and NPC, and (b) Raman spectra of FeNiP@NPC, FeP@NPC, and NiP@NPC, and (c and d) deconvoluted Raman peaks of FeNiP@NPC.

The presence of dopants in carbon is also confirmed by Raman spectroscopy as shown in Figure 3.18b. All of the spectra present typical D band and G band at about 1350 and 1580 cm<sup>-1</sup>, respectively. And a second-order band is located at ~2800 cm<sup>-1</sup>. From the deconvoluted spectrum of FeNiP@NPC shown in Figure 3.18b, the shoulder between D and G band is interpreted as the D'' peaks centred around 1500 cm<sup>-1</sup>, which is related to amorphous carbon.<sup>151</sup> In addition, the D\* as another shoulder of the D peaks is linked with the disordered graphitic lattice and D' is related to defects in the carbon lattice. The second order spectrum is processed by fitting into four peaks (G\*, 2D, D+D' and 2D'),<sup>152</sup> and D+D' as a defect related peak can be clearly found in all samples. Based on the above-mentioned analysis,

the ID/IG ratio is calculated to evaluate the defects or disordered sites. It is worth mentioning that the FeNiP@NPC has the highest ratio value ( $\sim 3.62$ ), resulting from the N/P dopants and TMPs hybridization, which are greatly favoured by the electrochemistry process.

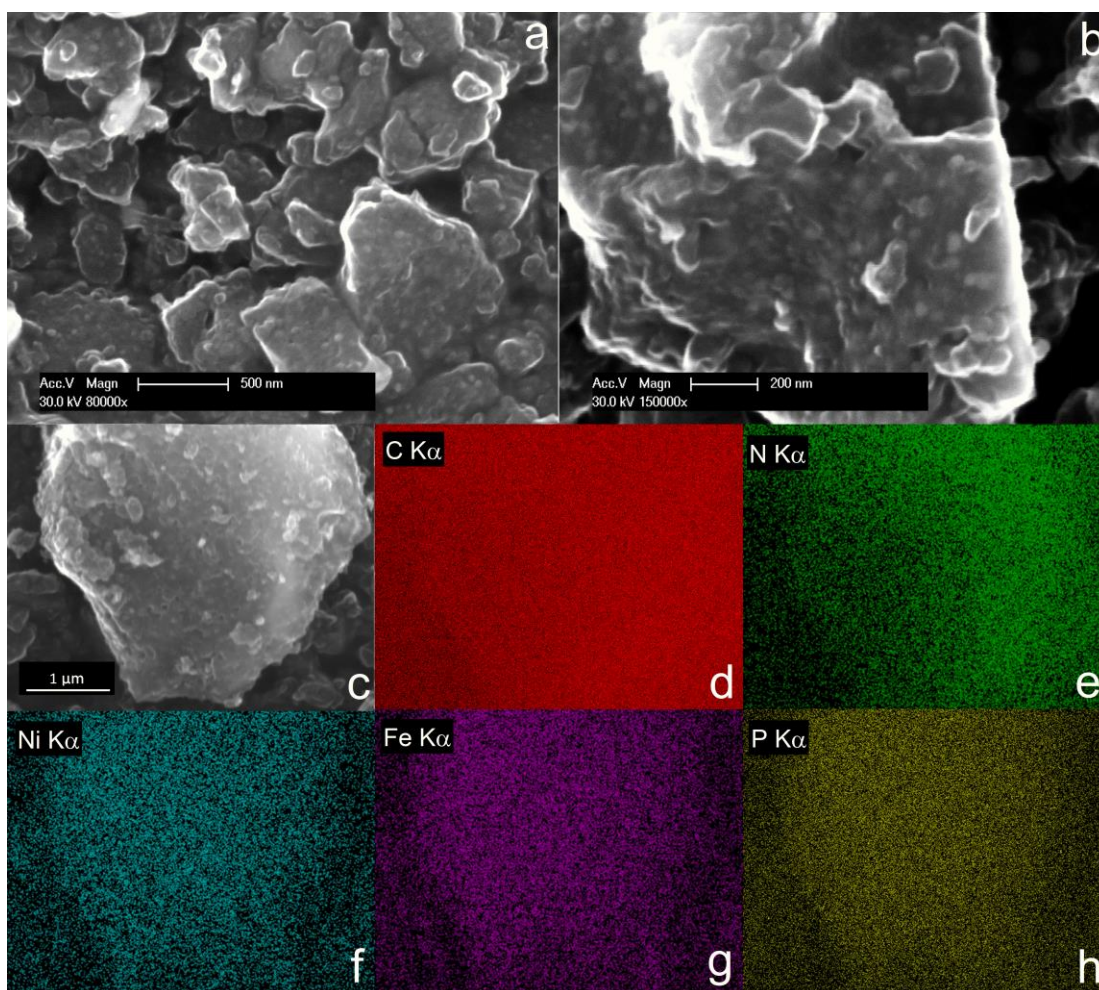


Figure 3.19 (a, b) SEM images of FeNiP@NPC with high and low magnification, and (c) EDS element mapping of FeNiP@NPC.

The morphologies and microstructures were studied by FE-SEM and TEM. As displayed in Figures 3.19a and 3.19b, the light round particles embedded in the carbon matrix are denoted as the TMPs particles. The rough and porous surface of TMPs particles not only ensures an enlarged SSA, but also provides the way for inner active sites thus facilitating a faster mass transfer. In Figure 3.19d to 3.19h, the EDS element mapping of FeNiP@NPC further illustrates the distribution of the involved elements. The homogeneous distribution of Ni, Fe, P, N, and C confirms the uniformly dispersed TMPs in the N and P co-doped carbon matrix.

The detailed nanostructure of FeNiP@NPC was further observed by TEM and the results are as shown in Figure 3.20. Figure 3.20a shows that the TMPs particles with a size of 30-50 nm are homogeneously dispersed in the carbon matrix. Figures 3.20b and 3.20c reveal a unique core-shell structure, namely,

TMP serves as the core and carbon as the shell. Along with a magnification, the carbon shell is analyzed with  $\sim 2$  nm thickness protecting the core TMPs. Interestingly, the feature of the carbon shell is totally different from that of the disordered and defective-rich carbon matrix, which is discussed in terms of the better catalysis effect of transition metal compounds for crystalline carbon precipitation out of the TMPs.<sup>153-155</sup> Most importantly, the attached carbon shell layers could be greatly beneficial for the conductivity and stability improvement of the hybrid nanomaterials. And from Figure 3.20c, the N/P successfully doped carbon displays different morphologies such as irregular graphite layers, amorphous carbon and some hole defects.<sup>156</sup> Besides, the uniformly wrapped TMPs nanoparticles distributed in the carbon matrix may also provide heterostructure interfacial activity sites to facilitate the catalytic performance.<sup>147</sup> The lattice structures of FeNiP@NPC are shown in the HR-TEM images. Lattice fringes of the core part are about 0.22 nm, which is possibly indexed to the 111 lattice plane of Fe<sub>2</sub>P (0.223 nm) and Ni<sub>2</sub>P (0.221 nm).<sup>157,158</sup> Simultaneously, from the partially enlarged XRD patterns of FeP@NPC, NiP@NPC and FeNiP@NPC displayed in Figure 3.20d, the typical diffraction peaks of FeNiP@NPC are located between Ni<sub>2</sub>P and Fe<sub>2</sub>P, confirming the presence of binary FeNi phosphide solid solution.

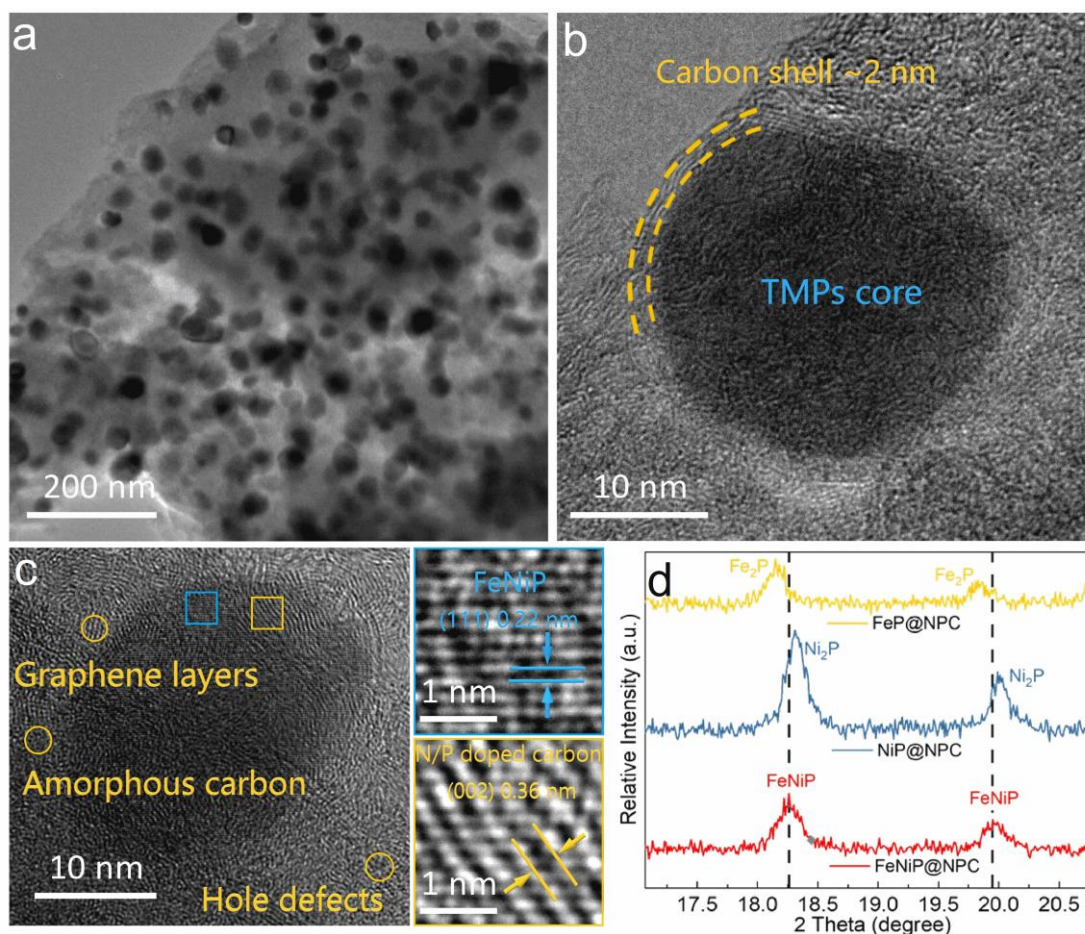


Figure 3.20 (a) TEM image and (b, c) HRTEM images of FeNiP@NPC, and (d) partially enlarged XRD patterns of TMP@NPC.

For a clearer observation of the elemental distribution in a more precise scale, the TEM-EDS mapping was also performed and the results are shown in Figure 3.21. The uniform distribution of Fe, Ni and P in the particles confirms the formation of the binary NiFeP phase, which possesses higher intrinsic activity and positive electronic interaction effect for electrocatalytic processes.<sup>159-161</sup> Besides the core part, the carbon shell and carbon matrix show  $\sim 0.36$  nm lattice fringes, which corresponds to the (002) lattice spacing of graphite. Noteworthily, the enlarged lattice spacing is attributed to the large-radius heteroatom P dopants, which is also coincided with the above-mentioned XRD peak shifting to lower angles.<sup>162</sup> Such a plentiful nanostructure of the hybrid material FeNiP@NPC is considered as the basis for greatly enhanced electrocatalytic properties derived from the heteroatom doping induced high conductivity and synergistic effects, and interfacial effects together with a core-shell protective morphology.

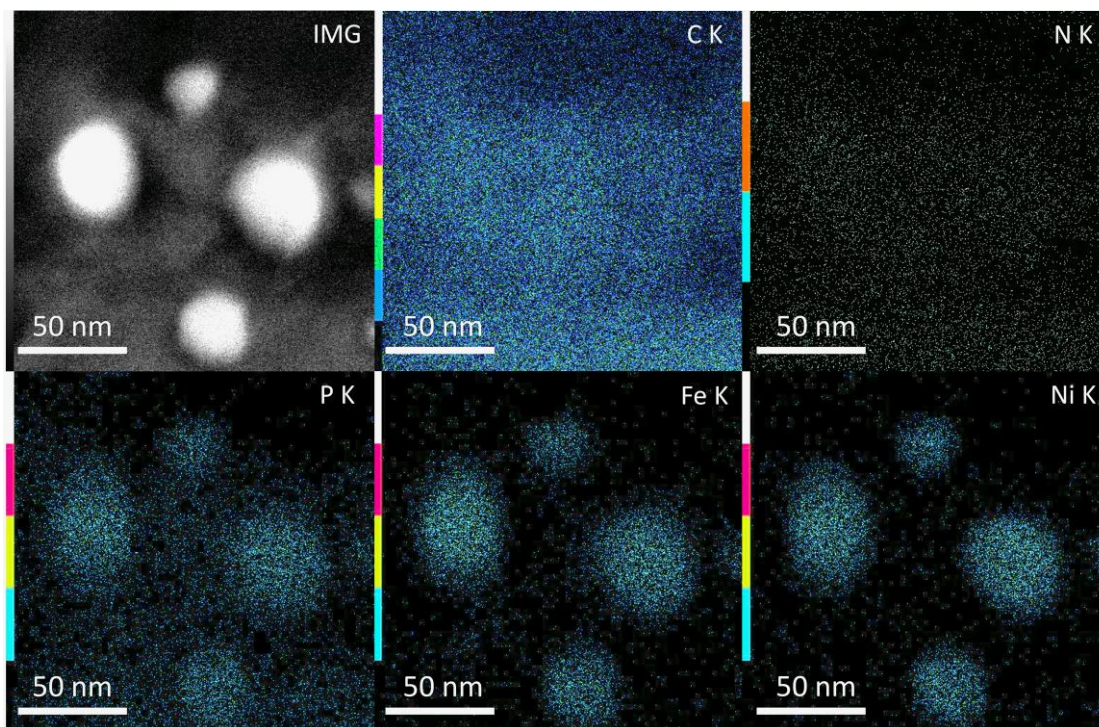


Figure 3.21 TEM-EDS mapping analysis of the FeNiP@NPC sample.

To further analyze the surface chemical compositions and whether the P and N have been doped into carbon matrix of FeNiP@NPC, XPS measurements were conducted. The survey spectrum is shown in Figure 3.22a, which confirms the presence of P, C, N, Fe, and Ni elements. In the deconvoluted pattern of Ni 2p (Figure 3.22b), the peaks located at around 853.1 and 873.6 eV are related to Ni-P species. And the doublet peaks centred at 856.1 and 875.7 eV are indexed to the Ni-O bond of Ni 2p<sub>3/2</sub> and Ni 2p<sub>1/2</sub> resulting from a partially surface oxidation. The shake-up satellite peaks are centred at about 862.1 and 880.3 eV.<sup>163</sup> As shown in Figure 3.22c, the Fe 2p spectrum is fitted into six peaks. The peaks at 706.2 and 720.2 eV are assigned to Fe-P bond in TMPs and other four peaks are related to Fe-O

bond due to air exposure and satellite peaks.<sup>163</sup> Figure 3.22d shows that the pattern of N 1s is deconvoluted into three different types of N species such as graphitic N, and pyrrolic N and pyridinic N corresponding to the peaks at 400.9, 399.5 and 398.3 eV, respectively.<sup>150,164</sup> In the P 2p spectrum (Figure 3.22e), the band is fitted into six peaks, including two peaks located at 129.6 and 130.8 eV assigned to P 2p<sub>3/2</sub> and P2p<sub>1/2</sub> originated from transition metal phosphides, and the peaks with higher binding energy are attributed to the P-C and P-O bonds.<sup>89,165,166</sup> This confirms that some exposed TMPs undergo oxidation to derive phosphate species under air. In addition, the analysis of the C 1s spectra shown in Figure 3.22f confirm the presence of P-C (285.4 eV) and C-N (286.0 eV) bonds in the carbon matrix.<sup>167</sup> In general, the XPS results indicate that N and P are doped into carbon matrix by replacing C atoms, where the electronic structure and surface polarity will be positively tuned for an improvement of electrocatalytic performance. As a result, an enhanced electronic interaction is expected to further improve the catalytic performance.

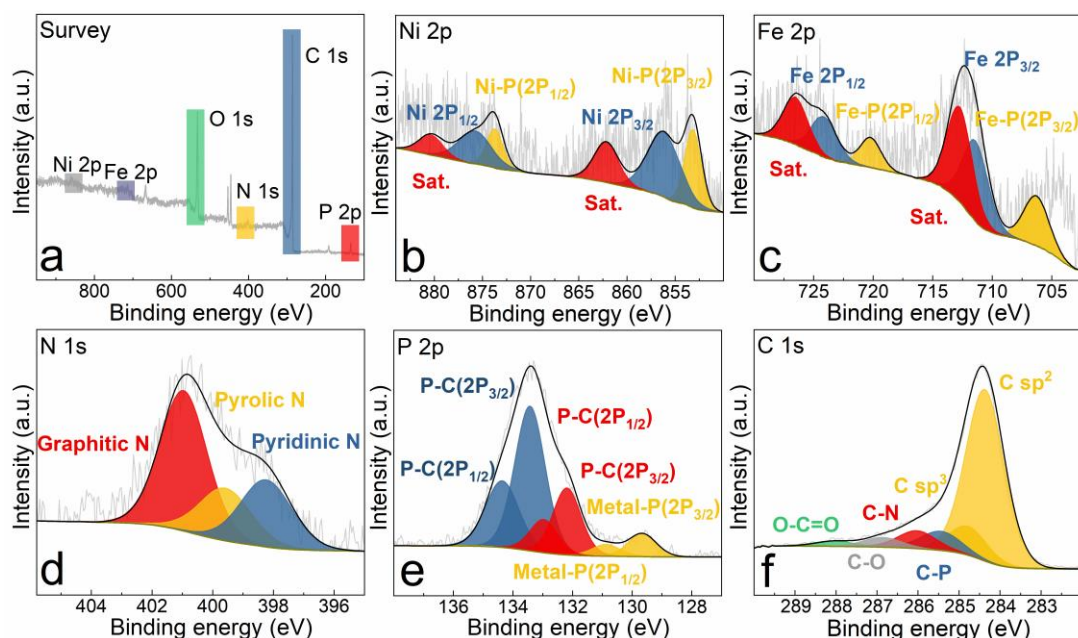


Figure 3.22 XPS spectra of FeNiP@NPC (a) full-scan spectrum, (b) Ni 2p, (c) Fe 2p, (d) N 1s, (e) P 2p, and (f) C 1s peaks.

Moreover, the surface area and pore size distribution for samples NPC, FeP@NPC, NiP@NPC, and FeNiP@NPC were characterized by BET N<sub>2</sub> adsorption and desorption test. As shown in Figure 3.23a, the N<sub>2</sub> sorption isotherms show a type-IV feature and hysteresis loop features, indicating a mesoporous structure. In addition, the pore size distribution of FeNiP@NPC shown in Figure 3.23b demonstrates that the dominant diameter of the mesopores is below 50 nm, coinciding with the type-IV isotherm plots and HRTEM results. Compared with the lowest BET SSA of NPC (98 m<sup>2</sup> g<sup>-1</sup>), the BET SSAs of FeNiP@NPC (420 m<sup>2</sup> g<sup>-1</sup>), NiP@NPC (421 m<sup>2</sup> g<sup>-1</sup>) and FeP@NPC (477 m<sup>2</sup> g<sup>-1</sup>) are greatly increased. Generally speaking, the metal-containing samples possess considerable surface area and



porosity in the hybrid-material microstructure, especially in the FeP@NPC with the highest SSA, which is in accordance with observed morphologies of different samples as displayed in Figure 3.24. Thus, the highly increased BET surface areas of metal-containing samples compared with bare NPC, provides additional transport channels and abundant reaction active sites.

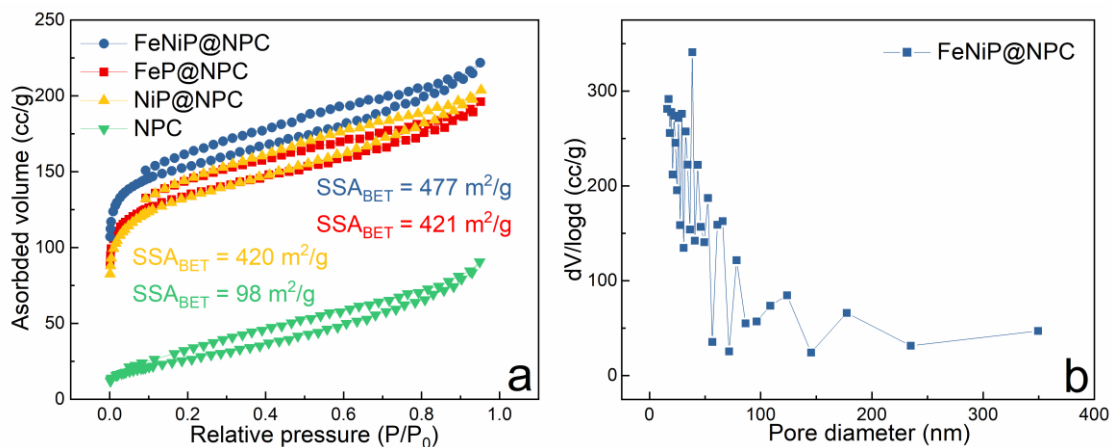


Figure 3.23 (a) Nitrogen adsorption-desorption isotherms of samples FeP@NPC, NiP@NPC, and FeNiP@NPC, and (b) pore size distribution of the FeNiP@NPC sample.

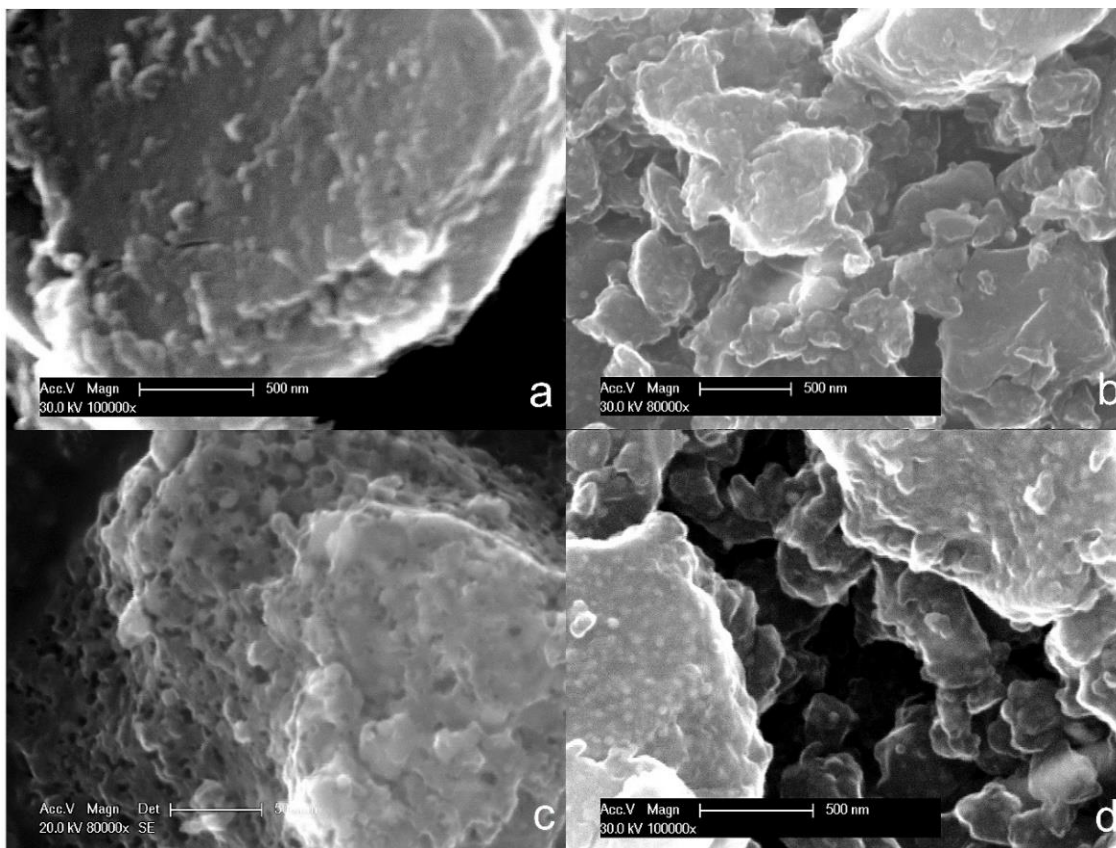


Figure 3.24 SEM images of (a) NPC, (b) NiP@NPC, (c) FeP@NPC, and (d) FeNiP@NPC.

In order to assess the electrochemical performances of the as-prepared hybrid nanomaterials, the HER

activity test was carried out under a standard three-electrode setup in 0.5 M H<sub>2</sub>SO<sub>4</sub> solution. For the HER performance, the bare NPC, FeNiP@NPC, FeP@NPC, and NiP@NPC electrodes were tested for comparison. The polarization curves with iR correction are shown in Figure 3.25, and the LSV curves reveal that the bare NPC displays poor activity. Impressively, the TMPs@NPC electrodes exhibit a dramatically enhanced electrochemical performance. For monometallic phosphides supported samples, FeP@NPC and NiP@NPC have much lower overpotentials of only 218 mV and 242 mV, respectively, to reach a current density of 10 mA cm<sup>-2</sup> compared with bare NPC (more than 600 mV). This result clearly indicates that the incorporation of TMPs nanoparticles promotes the electrocatalytic activity. And the overpotential of the binary metal phosphide FeNiP@NPC is further reduced to 191 mV comparing with that of the monometallic phosphides.

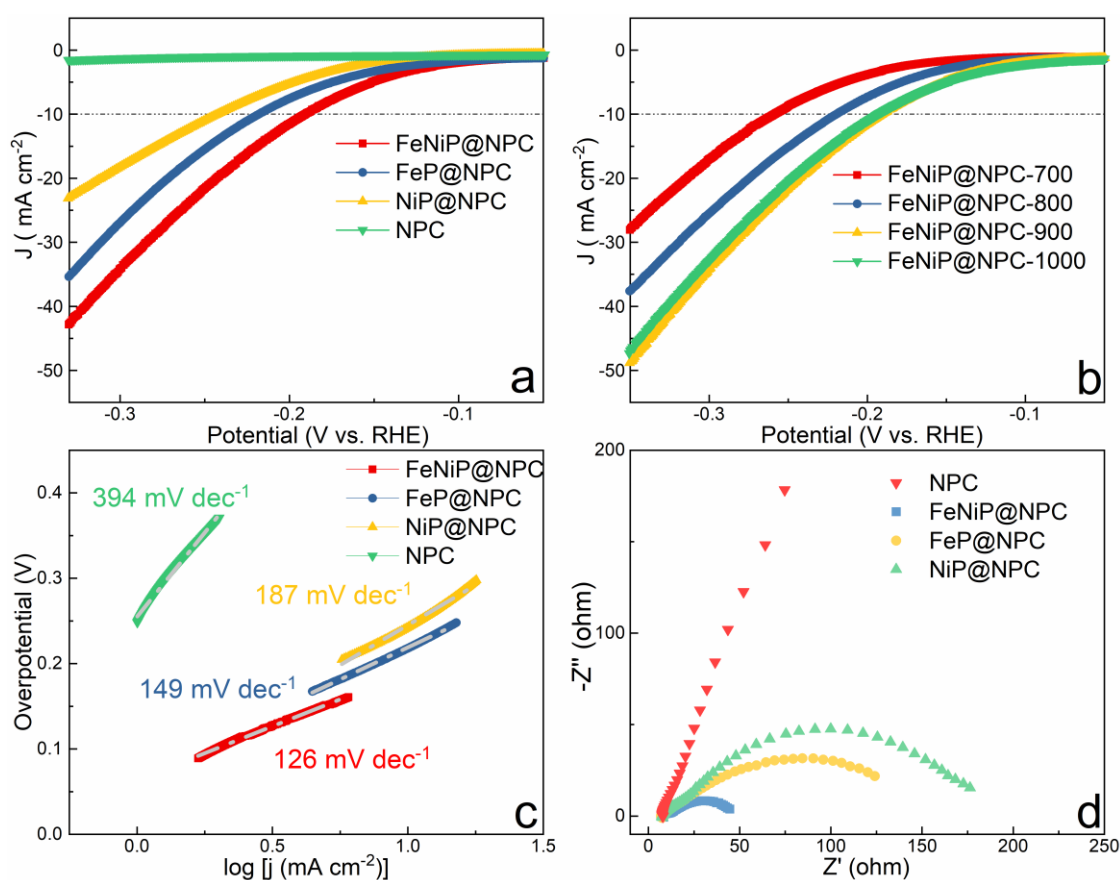


Figure 3.25 (a) Polarization curves of NPC, FeP@NPC, NiP@NPC, and FeNiP@NPC, (b) polarization curves of FeNiP@NPC annealed at different temperatures, (c) the corresponding Tafel plots of NPC, FeP@NPC, NiP@NPC, and FeNiP@NPC, (d) EIS spectra of NPC, FeP@NPC, NiP@NPC, and FeNiP@NPC in 0.5 M H<sub>2</sub>SO<sub>4</sub> solution.

This obviously enhanced HER performance is attributed to the enhanced intrinsic active component of NiFeP, and the interface effect between NiFeP and heteroatom doped carbon species. The insight into the enhanced performance of the FeNiP@NPC can be elucidated by various reported studies based on first-principles density functional theory simulation, and possible moderate  $\Delta G(H^*)$  of FeNiP@NPC is

essential for an efficient electrocatalyst to lower the reaction barriers in the adsorption and desorption stages, leading to efficient evolution of hydrogen molecules during the HER process.

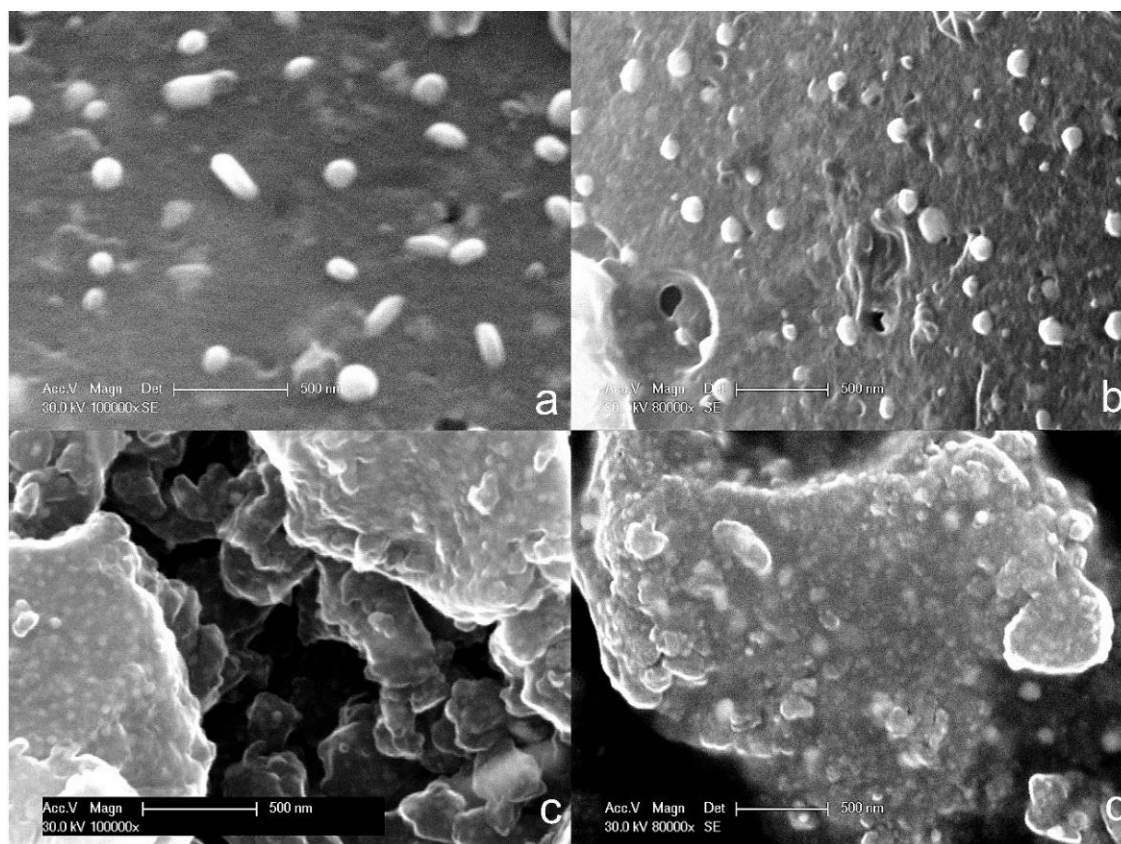


Figure 3.26 SEM images of (a) FeNiP@NPC-700, (b) FeNiP@NPC-800, (c) FeNiP@NPC-900, and (d) FeNiP@NPC-1000.

The HER performance of FeNiP@NPC samples obtained at different carbonization temperatures were evaluated to further explore the relationship between the nanostructures and HER activities. The LSV curves of FeNiP@NPC samples obtained at 700 °C, 800 °C and 1000 °C are shown in Figure 3.25b, indicating that the FeNiP@NPC-900 exhibits the most promising HER activity. For the FeNiP@NPC-700, FeNiP@NPC-800 and FeNiP@NPC-1000, the overpotentials to drive a current density of  $10 \text{ mA cm}^{-2}$  are 259 mV, 219 mV and 193 mV, respectively.

These results can be elucidated well by the different metal components and morphology of the FeNiP@NPC samples shown in Figures 3.26 and 3.27. The FeNiP@NPC-700 has some rod-like particles attached on the surface of the nanocomposites (Figure 3.26), which was investigated by the EDS point analysis (Figure 3.27). As can be seen from Figure 3.27, the nickel and oxygen contents of the rod-like particles (point b) are higher than that of the matrix (point a), suggesting that the particles are composed of transition metal phosphates (TMPi) rather than active TMP. For the sample FeNiP@NPC-800, the size of particles on the surface is significantly reduced due to partial reduction of the TMPi,

which agrees well with the reported studies that the formation of TMPs occurred at temperatures between 600 °C and 800 °C under the reduction of volatile phosphorus species.<sup>168</sup> Along with the further temperature increasing, most of the particles are buried under the carbon matrix for samples FeNiP@NPC-900 and FeNiP@NPC-1000, suggesting that a higher carbonization temperature is beneficial to accelerate the deoxidation of the transition metal phosphates to form active TMPs,<sup>169</sup> simultaneously ensuring a better carbon encapsulation for the TMPs and a better charge transfer ability.<sup>170</sup> As a result, a more stable core-shell structure and active heterointerfaces between defective-rich carbon and the TMPs are generated.

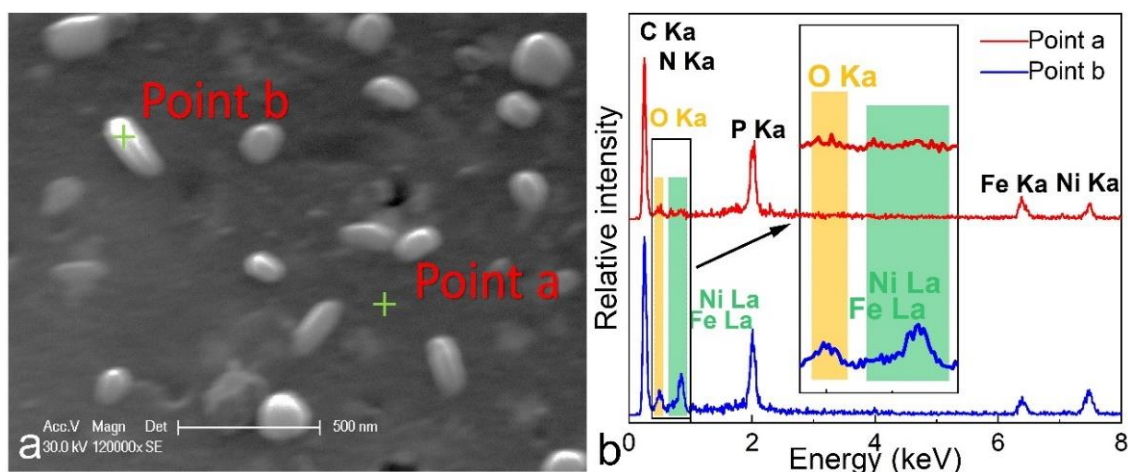


Figure 3.27 SEM images of (a) FeNiP@NPC-700, and (b) EDS points analysis spectroscopy of point a and b in image a.

The Tafel slope determined from the LSV curve was evaluated for an insight into the kinetics of HER, which demonstrates the elementary steps involved in the HER processes to elucidate the understanding of the enhanced activity of FeNiP@NPC. As shown in Figure 3.25c, the Tafel slope of FeNiP@NPC ( $126 \text{ mV dec}^{-1}$ ) is lower than those of FeP@NPC ( $150 \text{ mV dec}^{-1}$ ) and NiP@NPC ( $187 \text{ mV dec}^{-1}$ ), whereas the bare NPC shows the highest Tafel slope of  $394 \text{ mV dec}^{-1}$ . A smaller Tafel slope can ensure faster catalytic kinetics and preferred reaction mechanism. The results suggest that the FeNiP@NPC has the fastest reaction kinetics with initial proton adsorption step (Volmer step) as the rate-determining step.<sup>171</sup> Compared with the bare NPC, the encapsulated TMPs samples greatly enhanced the capability to adsorb protons during HER, accelerating the reaction kinetics.<sup>172</sup>

Meanwhile, the electrode kinetics and the electrical conductivity of the as-synthesized samples were investigated by EIS. It is well-known, the charge transfer resistance is an important parameter to uncover the electron transfer ability between electrolyte and electrocatalyst. According to the Nyquist plots shown in Figure 3.25d, the diameter of the arc notes as the  $R_{ct}$ . The  $R_{ct}$  of FeNiP@NPC is obviously lower than those of FeP@NPC, NiP@NPC, and bare NPC, which further suggests an excellent

conductivity and ability of charge transfer and favourable HER kinetics at the interface between FeNiP@NPC and electrolyte.

In general, the electrochemical efficiency is determined by intrinsic activity of catalytic sites and the accessible number of active sites. Because of the different adsorbates and conditions of tests, the BET surface areas not completely coincide with the electrochemical active surface areas. Thus, the ECSAs are evaluated by the  $C_{dl}$  to verify the catalytic efficiency, which was investigated using the CV technique in the non-Faradaic potential region at varying scan rates. All the current densities are in linear relationship with scan rates, and the slopes of the fitting plots correspond to the value of  $C_{dl}$  of each sample. As shown in Figure 3.28a, the  $C_{dl}$  of FeNiP@NPC ( $31.4 \text{ mF cm}^{-2}$ ) is much larger than those of FeP@NPC ( $15.4 \text{ mF cm}^{-2}$ ), NiP@NPC ( $9.4 \text{ mF cm}^{-2}$ ) and the bare NPC ( $2.2 \text{ mF cm}^{-2}$ ). The results indicate that the FeNiP@NPC has the highest ECSAs among all the samples, leading to more accessible active sites for an enhanced HER activity. The highest ECSAs of FeNiP@NPC are not consistent with the result of the BET surface area of FeNiP@NPC, suggesting that the higher activity of FeNiP@NPC mainly resulted from the synergistic effect and interface effect between TMPs and carbon matrix, and from an additional effect of high contact area between the electrolyte and exposed active sites.

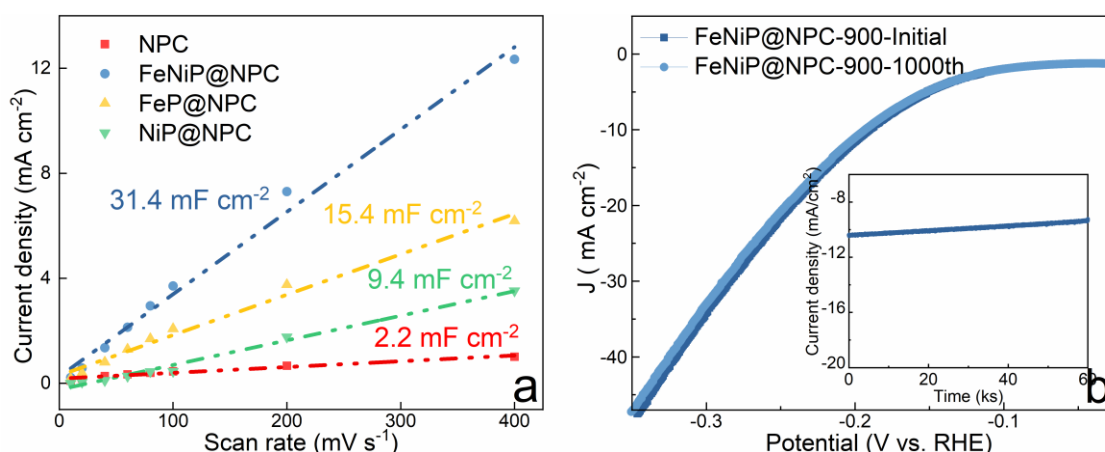


Figure 3.28 (a) Plots of current densities versus various scanning rates of NPC, FeP@NPC, NiP@NPC, and FeNiP@NPC, (b) LSV curves of FeNiP@NPC before and after 1000 potential cycles, the inset chronoamperometry of FeNiP@NPC at the constant potential of 195 mV vs. RHE in 0.5 M  $\text{H}_2\text{SO}_4$  solution.

Apart from the HER activities, the durability is another critical factor to evaluate the potential application of catalysts. In Figure 3.28b, the successive polarization curves analysis is measured for FeNiP@NPC with a scan rate of  $100 \text{ mV s}^{-1}$  for 1000 cycles in the acid electrolyte. After the continuous 1000 CV process, the LSV curves are remained nearly unchanged, demonstrating the outstanding HER stability of FeNiP@NPC. Moreover, the chronoamperometry test was also carried out at the constant potential of 195 mV vs. RHE displayed in Figure 3.28b. The result shows 91.5% retention of activity after 16 h cathodic treatment. The linear degradation in chronoamperometry testing maybe attributed

to two distinct factors. The first factor is related to the detachment of electrocatalysts, which is often caused by the bubbling of H<sub>2</sub>. The second factor is the consumption of electrolyte, which can also contribute to the observed degradation. The findings of both successive polarization curves analysis and chronoamperometry test prove an acceptable long-term durability of FeNiP@NPC and endorse a potential application for HER.

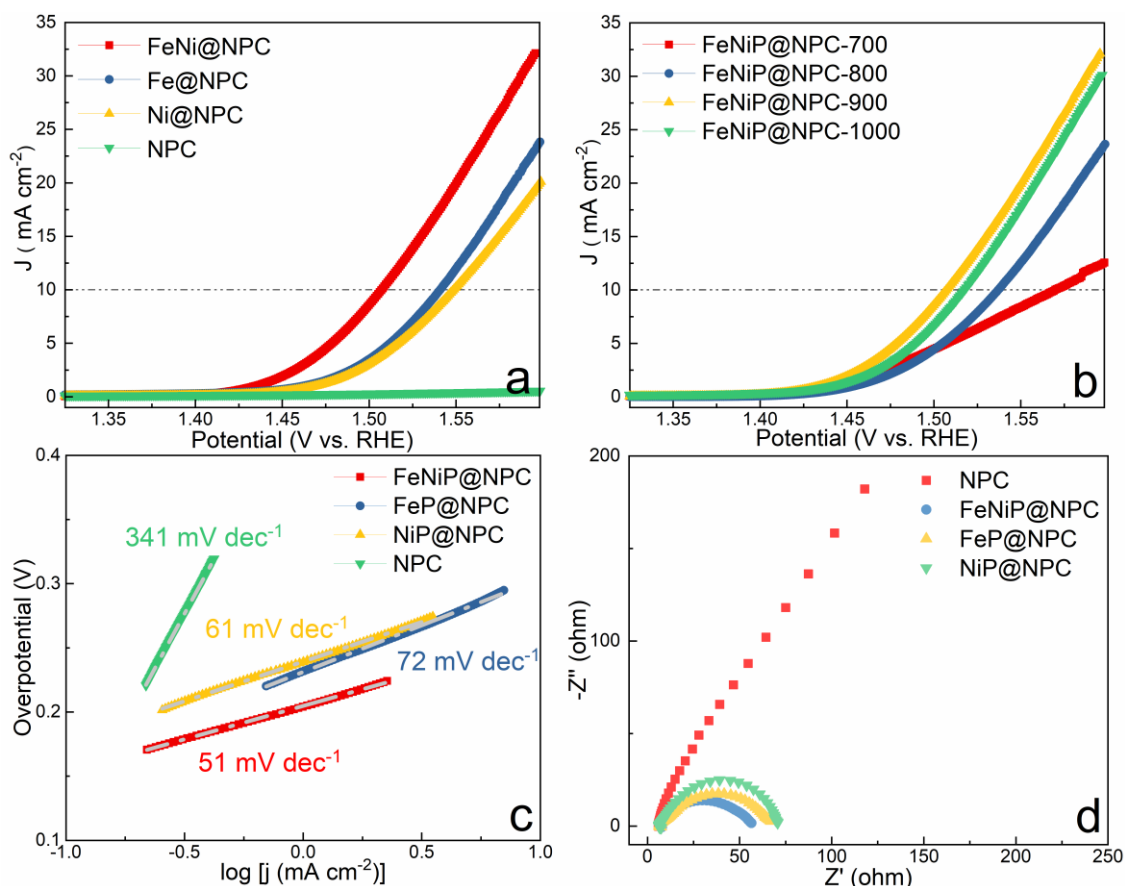


Figure 3.29 (a) OER polarization curves of NPC, FeP@NPC, NiP@NPC, and FeNiP@NPC, (b) polarization curves of FeNiP@NPC annealed at different temperatures, (c) the corresponding Tafel plots of NPC, FeP@NPC, NiP@NPC, and FeNiP@NPC, (d) the EIS spectra of NPC, FeP@NPC, NiP@NPC, and FeNiP@NPC in 1 M KOH solution.

The OER catalytic activities of as prepared catalyst were evaluated in 1 M KOH electrolyte. As shown in Figure 3.29a, the bare NPC based electrodes were tested for comparison, which exhibits the highest overpotentials of all the samples referring to an inferior OER efficiency. Whereas, facilitating with the embedded TMPs nanoparticles and the porous and core-shell structure formed after the TMPs loading, the OER catalytic efficiencies of FeP@NPC and NiP@NPC electrodes, which have overpotentials of 311 mV and 319 mV, respectively, to reach a current density of 10 mA cm<sup>-2</sup>, are significantly enhanced compared to that of the bare NPC electrode. Moreover, the overpotential required for FeNiP@NPC to reach a current density of 10 mA cm<sup>-2</sup> is further decreased to 278 mV, indicating a significant enhancement in OER catalytic activity attributed to the hetero-nanostructure engineering between

the carbon shell and FeNiP. The bimetallic FeNiP composite can facilitate electronic interactions and the electron transfer process, while the carbon provides a conductive channel for composite catalysts. Figure 3.29b presents the polarization curves of FeNiP@NPC samples derived from different carbonization temperatures. It reveals that the overpotentials decrease first from 700 °C to 900 °C, and then increase at 1000 °C synthesis temperature. The results are in accordance with the variation of the HER polarization curves, which not only resulted from the incomplete transformation from phosphate to phosphide, but also from the nanostructure difference caused by the different carbonization temperature. As shown in the HR-TEM images (Figure 3.30) of catalysts obtained from different carbonization temperatures, the carbon shell thickness increases with increasing synthesis temperature, which has a great influence on the electrochemical activity.<sup>173</sup> More layers of carbon in the shell slow down the charge transfer from the active core to the shell and species transport, thereby influencing the kinetics and HER/OER activity. In the present case, the optimized temperature is 900 °C, which ensures an appropriate number of carbon layers for encapsulating TMPs.<sup>82</sup>

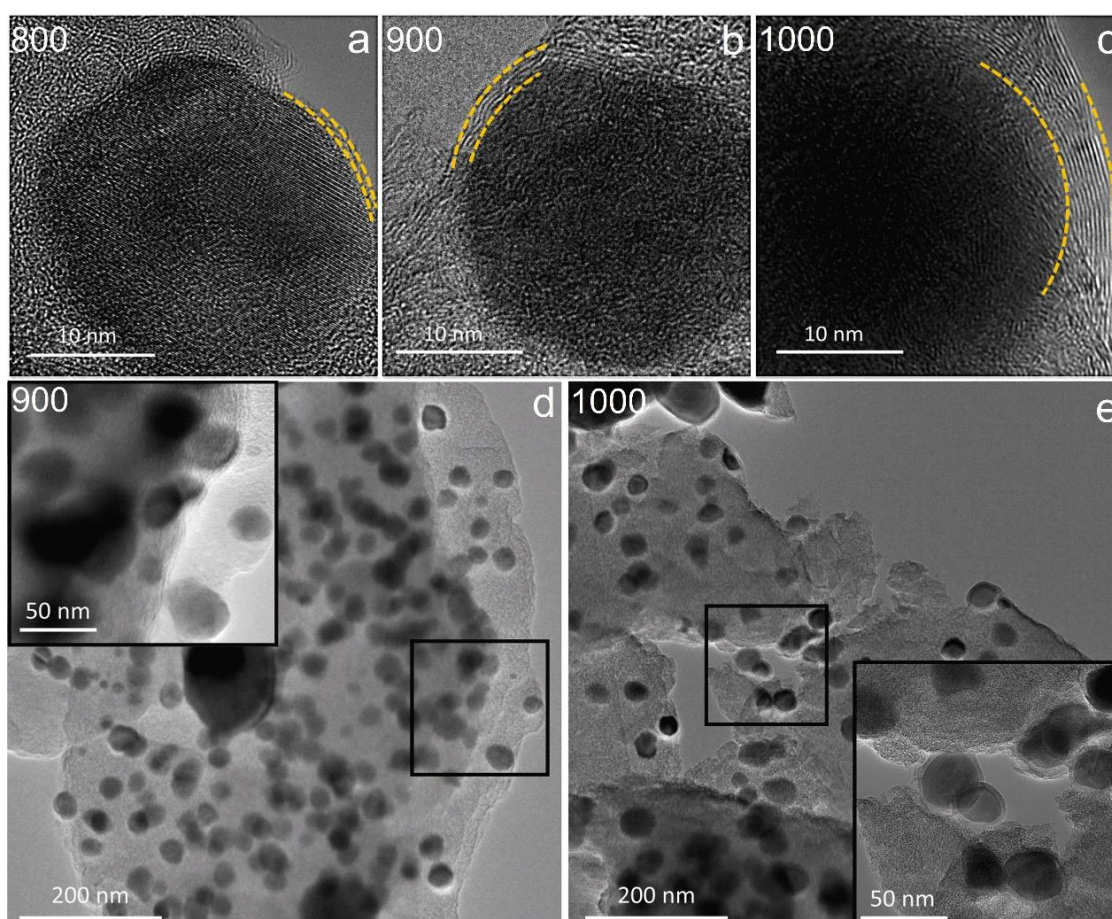


Figure 3.30 TEM images of (a) FeNiP@NPC-800, (b,d) FeNiP@NPC-900, (c,e) FeNiP@NPC-1000.

The OER kinetics were also investigated by Tafel plots as shown in Figure 3.29c. The FeNiP@NPC displays a very small Tafel slope of 52 mV dec<sup>-1</sup>, which is lower than those of FeP@NPC (73 mV dec<sup>-1</sup>),

NiP@NPC ( $62 \text{ mV dec}^{-1}$ ), and NPC ( $341 \text{ mV dec}^{-1}$ ), implying the fastest and most prominent charge transfer at the catalyst surface, corresponding to the best OER catalytic efficiency of FeNiP@NPC. The  $R_{ct}$  of the different catalysts are also measured, which reflect the charge transfer efficiency and ability of the OER process, as shown in Figure 3.29d. The lowest  $R_{ct}$  further manifests the most rapid charge transfer and result in an enhanced OER electrocatalytic activity of the FeNiP@NPC nanomaterial.

$C_{dl}$  values were used to evaluate the ECSAs of OER as well. The current density versus potential scan rate plots calculated from CVs within a non-faradic region. As displayed in Figure 3.31a, the measured  $C_{dl}$ s are 3.7, 2.0, 1.5 and  $0.4 \text{ mF cm}^{-2}$  for FeNiP@NPC, FeP@NPC, NiP@NPC, and bare NPC, respectively. The order in  $C_{dl}$  completely coincides with the results of the HER, implying that the FeNiP@NPC has a highest surface area (see Figure 3.23a) to expose reactive sites for chemisorption of the reactants, intermediate species and electron transfer through the electrolyte-catalyst interface.

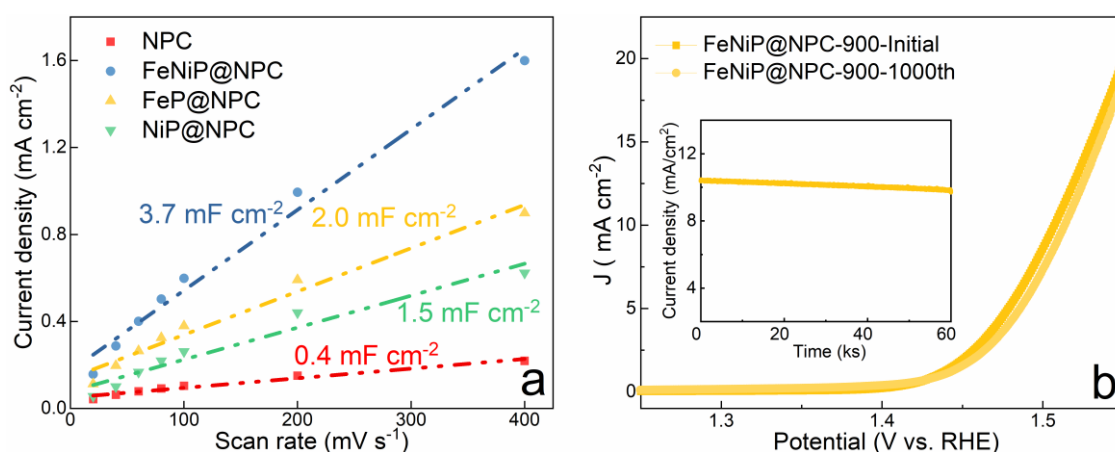


Figure 3.31 (a) Plots of current densities versus various scanning rates of NPC, FeP@NPC, NiP@NPC, and FeNiP@NPC, (b) LSV curves of FeNiP@NPC before and after 1000 potential cycles, the inset shows the chronoamperometry of FeNiP@NPC at the constant potential of 1.51 V vs. RHE in 1 M KOH solution.

Successive CV method was utilized to evaluate the stability of FeNiP@NPC for OER in 1M KOH electrolyte. As demonstrated in Figure 3.31b, the overpotential at  $10 \text{ mA cm}^{-2}$  with a slight increase from 273 to 300 mV after 1000 cycles reveals the satisfying OER stability. Meanwhile, the durability was also demonstrated by the chronoamperometric technique as shown in Figure 3.31b, since a stable current density output with 6.6% loss was observed for more than 16 h. Thus, it can be further concluded that the FeNiP@NPC catalyst has an excellent activity and application prospect in electrocatalysis for OER as well.

Overall, the FeNiP@NPC-900 catalyst exhibits overpotentials for both the HER and OER that are comparable to those reported for other catalysts listed in Table 3.3 of the Supporting Information, indicating its potential for practical water splitting applications. The activity and stability performance



of FeNiP@NPC-900 leads to improved efficiency and lower costs in practical water splitting processes. Additionally, the facile and cost-effective preparation method of FeNiP@NPC-900 makes it an attractive option for large-scale and low-cost production.

Table 3.3 Summary of HER and OER performance of reported TMP/carbon-based catalysts.

Catalysts	Overpotential of HER <sup>a</sup>	Overpotential of OER <sup>b</sup>	Ref.
FeNiP@N-CFs	-	300 mV	161
Ni <sub>2</sub> P@C/G	-	285 mV	174
NFP@NC	-319 mV	295 mV	175
FeNi <sub>3</sub> /Ni <sub>2</sub> P@CN	-	298 mV	176
CoP/PNC	-	300 mV	64
Ni <sub>2</sub> P@NC	-138 mV	320 mV	177
NiCoPCF	-254 mV	340 mV	178
CoP@NPC	-184.35 mV	303 mV	179
CoP@NC	-257 mV	-	180
FeP@NC	-194 mV	-	180
H-CoP@NC	-	320 mV	68
Fe <sub>2</sub> P@Fe <sub>4</sub> N@C-800	-232 mV	164 mV	181
FeP@NPCs	-	300 mV	182
0.75-NC-FexP	-193 mV	302 mV	183
FeNiP/NPC	-277 mV	-	184
<b>FeNiP@NPC-900</b>	<b>-191 mV</b>	<b>278 mV</b>	<b>[Our work]</b>

<sup>a</sup> HER overpotential at a current density of -10 mA cm<sup>-2</sup> (based on electrode geometric area).

<sup>b</sup> OER overpotential at a current density of 10 mA cm<sup>-2</sup> (based on electrode geometric area).

### 3.3 Single-source-precursor derived molybdenum phosphide quantum dots encapsulated by P/N-co-doped carbon as electrocatalyst for hydrogen evolution reaction in acid and alkaline electrolytes

The content of this chapter is published in:

**Chen, Y.,** Jiang, T., Tian, C., Zhan, Y., Adabifiroozjaei, E., Kempf, A., Molina-Luna, L., Hofmann, J. P., Riedel, R. & Yu, Z. Molybdenum Phosphide Quantum Dots Encapsulated by P/N-Doped Carbon for Hydrogen Evolution Reaction in Acid and Alkaline. *ChemsusChem*, e202300479 (2023). © Wiley

The process to synthesize MoP@NPC/CNT-900 nanocomposite powders is schematically depicted in Figure 3.32. In detail, the SSP is first fabricated by a facile self-assembly reaction of TA, CNTs, PA, PEI, and molybdate anions ( $\text{MoO}_4^{2-}$ ). Subsequently, MoP@NPC/CNT-900 nanomaterials are obtained *in-situ* by the synergistic carbonization and phosphidation process in which PA serves as the P source of MoP QDs and heteroatom P dopants in the carbon shell and matrix and PEI is the initiator of the self-assembly and source of N dopants. The Mo-grafted TA effectively are converted into the carbon substrate and protective shell for well-dispersed ultra-small MoP QDs.

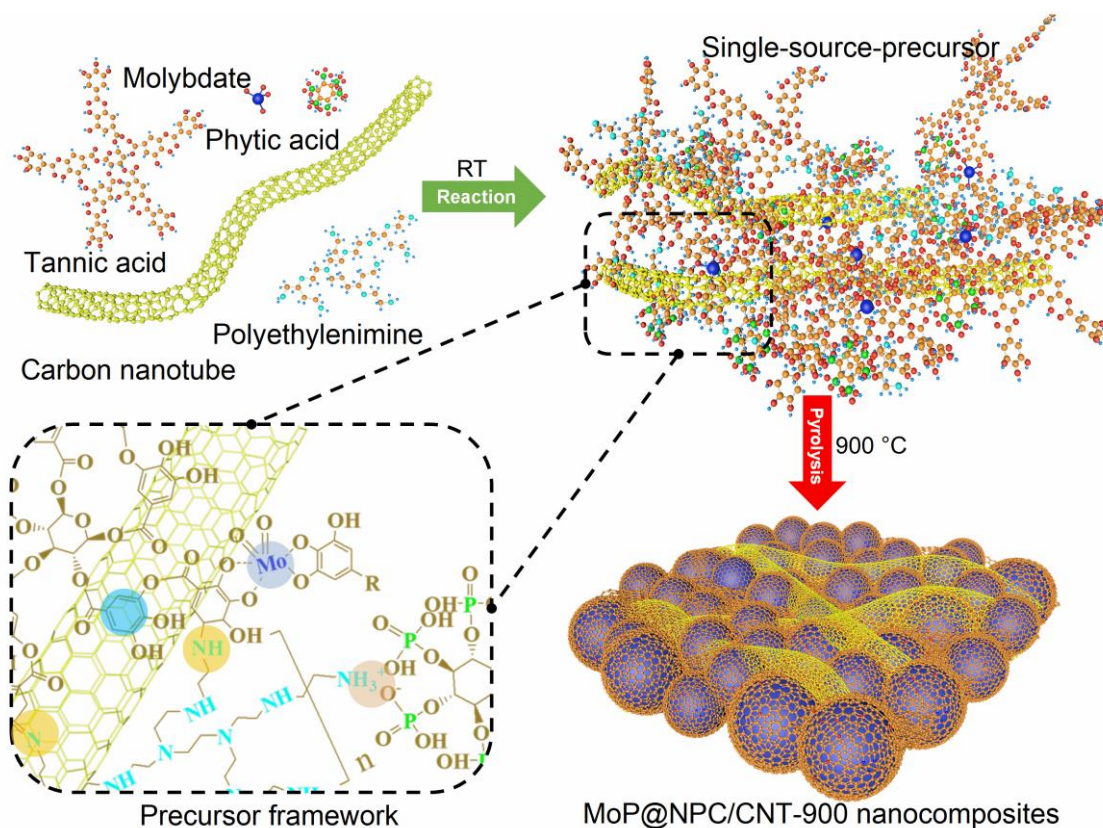


Figure 3.32 Schematic illustration of the formation of single-source-precursor and derived MoP@NPC/CNT-900.

For the SSP fabrication, the following reactions/interactions are involved: (i) The catechol-rich TA provides the active binding sites to coordinate molybdate anions to form molybdate-catechol

complexes as reported in the literature.<sup>185-188</sup> (ii) TA molecules with benzene rings are anchored to the surface carbon rings of CNTs via  $\pi$ - $\pi$  interactions.<sup>189-191</sup> (iii) The amine group in PEI and the highly active quinone in TA are condensed by Schiff base reaction and/or Michael addition,<sup>115,192,193</sup> as proved by FTIR and XPS analysis of the MoP@NPC/CNT single-source-precursor (MoNPC) shown in Figure 3.33a and 3.33b. Since the broadness and distortion of the IR peak around 1700  $\text{cm}^{-1}$  and the new peaks at 1486 and 1585  $\text{cm}^{-1}$  correspond to C-N and C=N stretching,<sup>114,115</sup> and the deconvolution of the C1s spectrum further confirmed the bonding between TA and PEI.<sup>114,143,194</sup> (iv) The firmly ionic chelation between positively charged PEI ( $-\text{NH}_3^+$ ) and negatively charged PA is not only validated by the absorption peaks centred at 965 and 1057  $\text{cm}^{-1}$  in the FTIR spectrum but also by the XPS characterization of the protonated amine groups in the precursor.<sup>195</sup> (v) The broad band at around 3000-3500  $\text{cm}^{-1}$  of precursor becomes weaker and wider compared with those of TA and PA as shown in Figure 3.34a, suggesting the formation of hydrogen bond between PA and PEI.<sup>144,196</sup> The Raman spectra results of the precursors are shown in Figure 3.34b, indicating that the Mo-O and M=O stretching vibrations are clearly identified.<sup>197</sup>

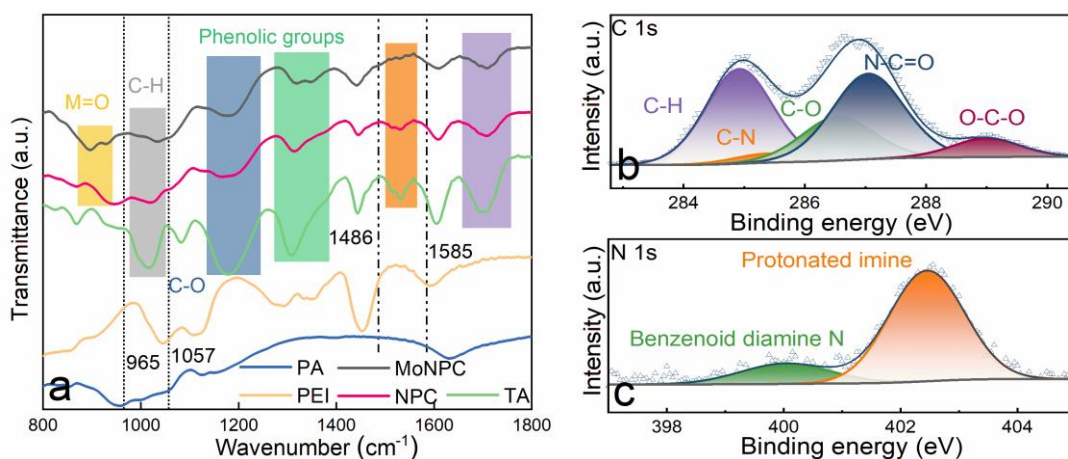


Figure 3.33 (a) FT-IR spectra of MoP@NPC/CNT precursors (MoNPC), NPC/CNT precursors (NPC), TA, PA, and PEI, and X-ray photoelectron spectrum of (b) C 1s and (c) N 1s of MoP@NPC/CNT precursor.

The X-ray diffraction (XRD) measurements were implemented to confirm the crystalline phases of the as-synthesized samples. In Figure 3.35a, the XRD pattern of MoP@NPC/CNT-900 marked blue, shows that all the diffraction peaks match well with the hexagonal MoP (PDF#24-0771) crystalline phase, where the diffraction peaks centred at around 12.75°, 14.60°, and 19.45° are assigned to the (001), (100), and (101) lattice planes of MoP (PDF#24-0771) and no other crystalline reflections are identified besides the amorphous and highly defective carbon peak at around 12.5° of the (002) plane. In contrast, the bare NPC/CNT-900 and MoP-900 sample were prepared under the same conditions without molybdate ions and TA addition. The XRD pattern of the NPC/CNT-900 sample exhibits two broad peaks at around 12.5° and 20.0° corresponding to the (002) and (101) planes of carbon, and the

detected shift of the carbon reflections are caused by the doping of carbon with nitrogen and phosphorus. However, the XRD pattern of MoP-900 marked in red identifies as a mixture of MoP and MoP<sub>2</sub>O<sub>7</sub> phases instead of MoP single crystalline phase, which validated the crucial reduction of the TA for the formation of MoP without the use of other reductants like H<sub>2</sub> and PH<sub>3</sub> as previously reported literature.<sup>198,199</sup> These observations suggest the successful conversion of the MoP@NPC/CNT SSPs into carbon substrate anchored MoP QDs hybrid material.

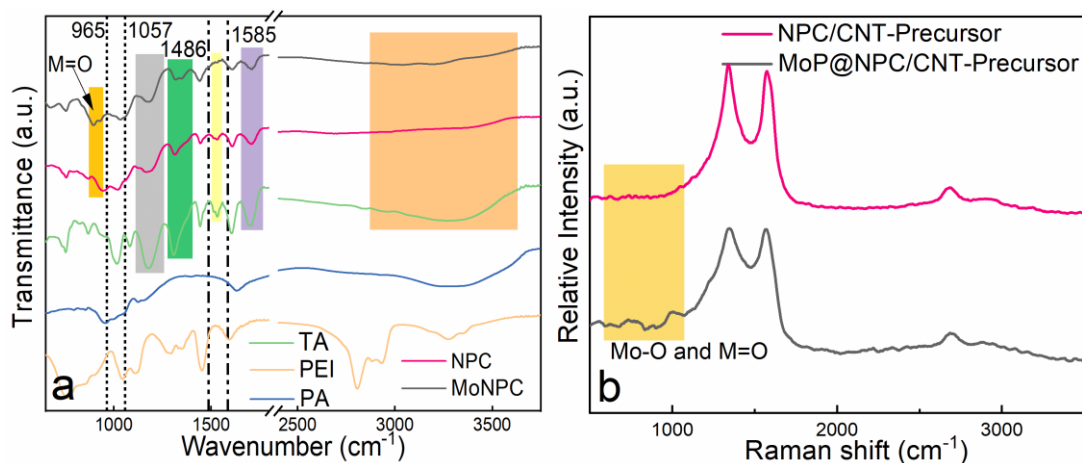


Figure 3.34 (a) FTIR spectra of MoP@NPC/CNT precursors (MoNPC), NPC/CNT precursors (NPC), TA, PA, and PEI, and (b) Raman spectrum of MoP@NPC/CNT precursors and NPC/CNT precursors.

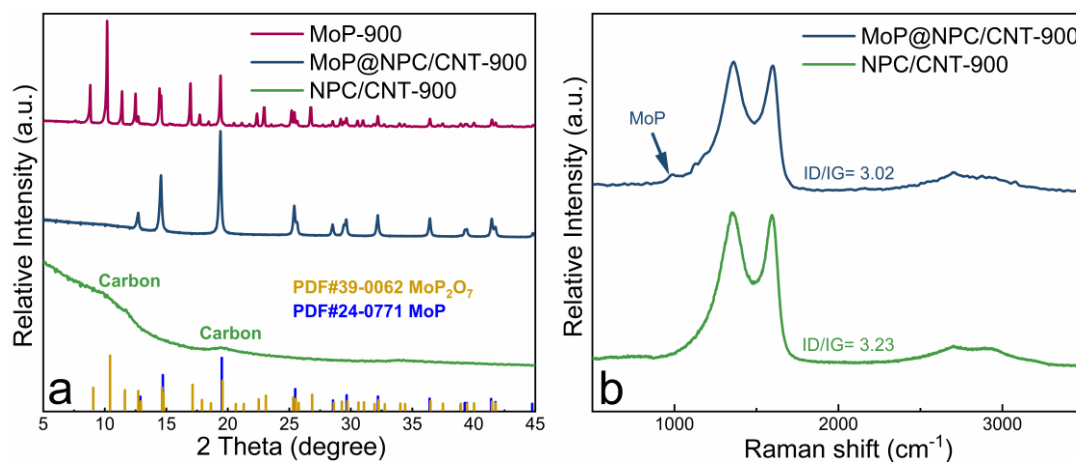


Figure 3.35 (a) XRD pattern of MoP@NPC/CNT-900, NPC/CNT-900, and MoP-900, and (b) Raman spectra of MoP@NPC/CNT-900 and NPC/CNT-900.

Furthermore, the Raman spectra displayed in Figure 3.35b illustrate the composition and the graphitization degree of each sample. The MoP@NPC/CNT-900, and NPC/CNT-900 samples exhibit two typical adsorption peaks at  $\sim 1350$  and  $\sim 1580$   $\text{cm}^{-1}$ . Generally, the former is associated with  $\text{sp}^3$ -hybridized disordered or defective carbon (D-band), and the latter is ascribed to  $\text{sp}^2$ -hybridized graphitic carbon (G-band). The relative intensity of  $I_D/I_G$  reflects the ratio of disordered carbon to

graphitic carbon. The  $I_D/I_G$  values of MoP@NPC/CNT-900, and NPC/CNT-900 are calculated to be about 3.02 and 3.23, respectively, indicating that the content of disordered carbon is reduced after the introduction of MoP. The higher graphitization degree of the hybrid is discussed to be caused by the catalytic effect of MoP on the graphitic carbon, which will be beneficial for accelerating the electron transfer.<sup>200,201</sup> In addition, some characteristic peaks located around  $1000\text{ cm}^{-1}$  are found in the Raman spectrum of MoP@NPC/CNT-900, which is indexed to the obtained MoP phase.<sup>202</sup>

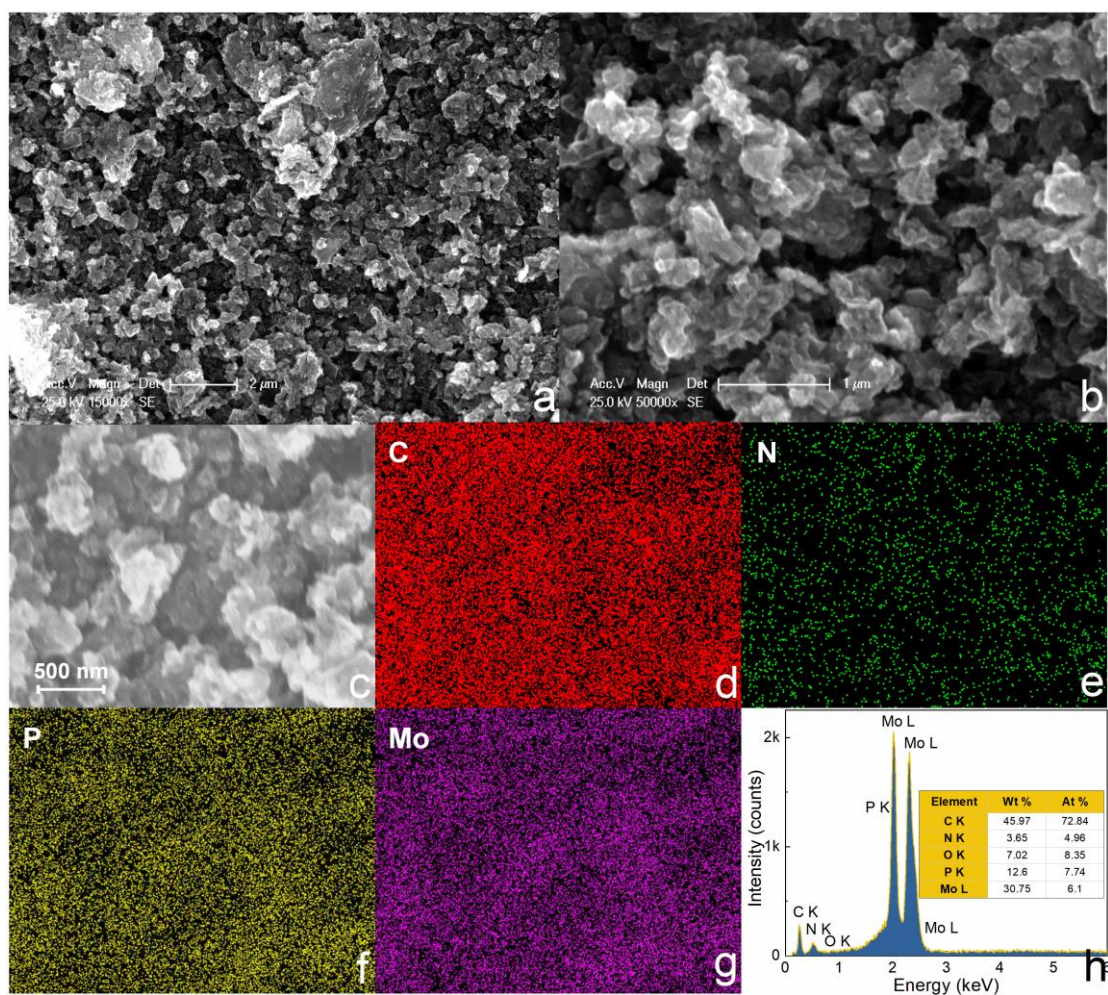


Figure 3.36 (a-c) SEM images, (d-g) elemental mapping images, and (h) the EDS spectrum analysis of MoP@NPC/CNT-900.

The morphologies and microstructures were disclosed by SEM and TEM. Figures 3.36a and 3.36b exhibit the SEM images of the as-prepared MoP@NPC/CNT-900 at different magnifications, showing the presence of 3D branched and interconnected amorphous particles. The special network is expected provide high amount of interfacial active sites and mass transfer channels for the electrocatalytic process. The morphology of the control samples, namely bare MoP-900 and NPC/CNT-900 are shown in Figure 3.37. In Figure 3.36d to 3.36h, the EDS element mapping and spectrum visualize the distribution of elements involved in MoP@NPC/CNT-900, demonstrating a homogenous

distribution of Mo, N, P, and C with the relative contents of 30.75, 3.65, 12.6, and 45.97 wt.%, respectively. The results confirm the uniformly dispersed MoP in N and P co-doped carbon matrix. The presence of O from the EDS analysis results from the partial surface oxidation of MoP.<sup>203,204</sup>

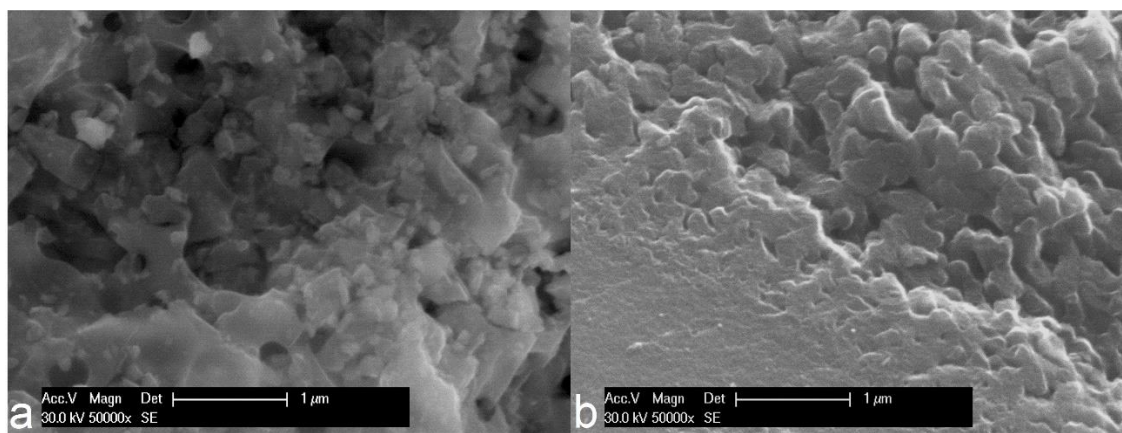


Figure 3.37 SEM images of (a) bare MoP-900 sample and (b) NPC/CNT-900 sample.

To further probe the detailed nanostructure of MoP@NPC/CNT-900, TEM was conducted and the results are displayed in Figure 3.38. It can be clearly seen that the hybrid compound has a well-defined nanomorphology with ultrasmall nanoparticles and entangled CNTs. In addition, the structure is highly porous (white area) and the particles (dark dots) are homogeneously dispersed in the substrate carbon framework. Importantly, Figures 3.38b and 3.38d reveal that the MoP nanoparticles with the diameter of ca. 5 nm are tightly anchored on the highly defective amorphous carbon matrix. Figure 3.38c and 3.38d provide the HRTEM images to verify the presence of CNTs and MoP. The lattice fringe around 0.346 nm can be assigned to the (001) lattice plane of carbon,<sup>205</sup> and the fringe spacing of the particles is about 0.279 nm, corresponding to (100) lattice plane of the hexagonal MoP.<sup>206,207</sup> In addition, a highly defective carbon shell is analyzed in Figure 3.38d, which is considered to be formed via a catalytic effect of the MoP core to accelerate crystalline carbon precipitation during pyrolysis.<sup>119</sup> Most importantly, the carbon shell layers not only can inhibit aggregation of the MoP particles, but also greatly enhance the electronic conductivity and improve the chemical stability of the hybrid nanomaterials during the electrolysis process. Besides, the homogeneously distributed MoP QDs in the carbon matrix also forms essential heterostructure interfacial between MoP and carbon to elevate the catalytical performance. Simultaneously, for a clearer observation of the element distribution in a more precise scale, TEM-EDS mapping was also performed and the results are shown in Figures 3.38e to 3.38i. The uniformly distribution of N, P and C confirms the existence of N and P dopants in the carbon matrix, which has been regarded as an effective strategy to improve the electronic conductivity for the electrocatalytic processes as well. Besides, as shown in Figures 3.38h and 3.38i, it can be assumed that Mo and P are agglomerated as the hexagonal MoP phase (Figure 3.38j), which also

coincides with the above mentioned XRD results. Such a plentiful nanostructure of MoP@NPC/CNT-900 not only greatly enhances the electrocatalytic properties by high conductivity derived from the CNTs and heteroatom dopants, but also promotes the synergistic effects between the defective carbon shell and MoP QDs to facilitate the electrocatalysis.<sup>208,209</sup>

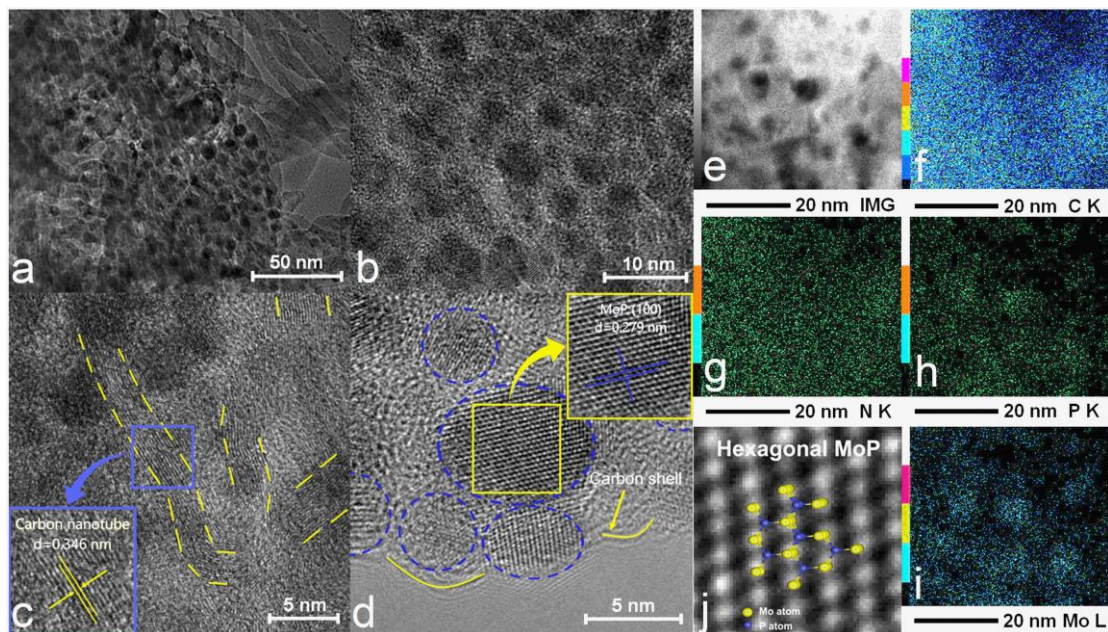


Figure 3.38 (a) Low-magnification TEM image, (b-d) high-resolution TEM images, (e-i) TEM elemental mapping images of C, N, P, and Mo of MoP@NPC/CNT-900, and (j) the hexagonal structure of MoP QDs.

XPS measurement was performed to disclose the electronic states and surface chemical composition of the MoP@NPC/CNT-900. The full-scan spectrum is shown in Figure 3.39a, confirming the existence of P, C, N, and Mo elements. Focusing on the deconvoluted spectrum of Mo 3d (Figure 3.39b), the peaks located at 228.0 and 231.5 eV demonstrate the characteristic doublets of Mo 3d<sub>5/2</sub> and 3d<sub>3/2</sub> for Mo<sup>δ+</sup> (0 < δ < 4), and is indexed to MoP.<sup>210,211</sup> The peaks centred at 236.1 and 233.0 eV are identified as Mo 3d<sub>3/2</sub> and 3d<sub>5/2</sub> for Mo<sup>6+</sup> indexed to MoO<sub>3</sub>, respectively. In addition, the peaks at 229.2 and 232.5 eV are ascribed to 3d<sub>5/2</sub> and 3d<sub>3/2</sub> for MoO<sub>2</sub>. These results are potentially related to the surface oxidation of metastable MoP species into MoO<sub>2</sub> and MoO<sub>3</sub> when exposed to the natural environment.<sup>212</sup> As exhibited in Figure 3.39c, the spectrum of P 2p can be deconvoluted into six peaks. The peaks located at 129.2 eV and 130.1 eV are ascribed to 2p<sub>3/2</sub> and 2p<sub>1/2</sub> coming from low-valence P in MoP. Electronic interaction between Mo and P atoms can effectively modify the d-band configuration of Mo, which is expected to alter the Mo-H bond strength during the H<sub>ads</sub> species desorption.<sup>203,213</sup> The four left peaks are indexed to 2p<sub>1/2</sub> and 2p<sub>3/2</sub> orbitals of P-C and P-O bonds. The strong electron interaction between the carbon shell and MoP, as well as the presence of P dopants in the carbon matrix, was confirmed by the clear P-C peak.<sup>165,214</sup> Meanwhile, the P-C bond is also confirmed by the C1s spectrum (Figure 3.39d), since the peaks at 284.5 and 284.8 eV are attributed to the bonding of sp<sup>2</sup> and sp<sup>3</sup> carbon. The

additional peaks appearing at 285.7, 286.8, 287.8, 289.4, and 291.0 eV are assigned to C-P, C-N, C–O, C=O, and  $\pi$ - $\pi^*$ , respectively, demonstrating that heteroatom N has been doped into the carbon matrix successfully.<sup>114,213,215-219</sup> The incorporation of both P and N atoms could effectively tailor the local electronic structure and improve the electrical conductivity of the carbon layer to create more active sites, thus facilitating the improvement of the electrocatalytic performance.<sup>220,221</sup> Furthermore, the types of the N atoms dopants are further clarified by the N 1s spectrum (Figure 3.39e), which is divided into several different type of N species including pyridinic-N, pyrrolic-N, and graphitic-N. Pyridinic-N is the dominant species in the MoP@NPC/CNT-900 sample.<sup>222-224</sup> Several studies and DFT calculations confirmed that the synergistic effect primarily results from the interaction of pyridinic-N (rather than pyrrolic-N or graphitic-N) with MoP, thereby increasing the electrocatalytic performance.<sup>40</sup> In addition, the peak located approximately at 394.5 eV is a representative signal of Mo 3p<sub>3/2</sub>.<sup>225</sup> The XPS spectrum of O 1s is also shown in Figure 3.39f, indicating the existence of oxidised molybdenum species (530.8 eV), O–H band (531.5 eV), and the phosphate group (532.9 eV) in the hybrids.<sup>210,226</sup>

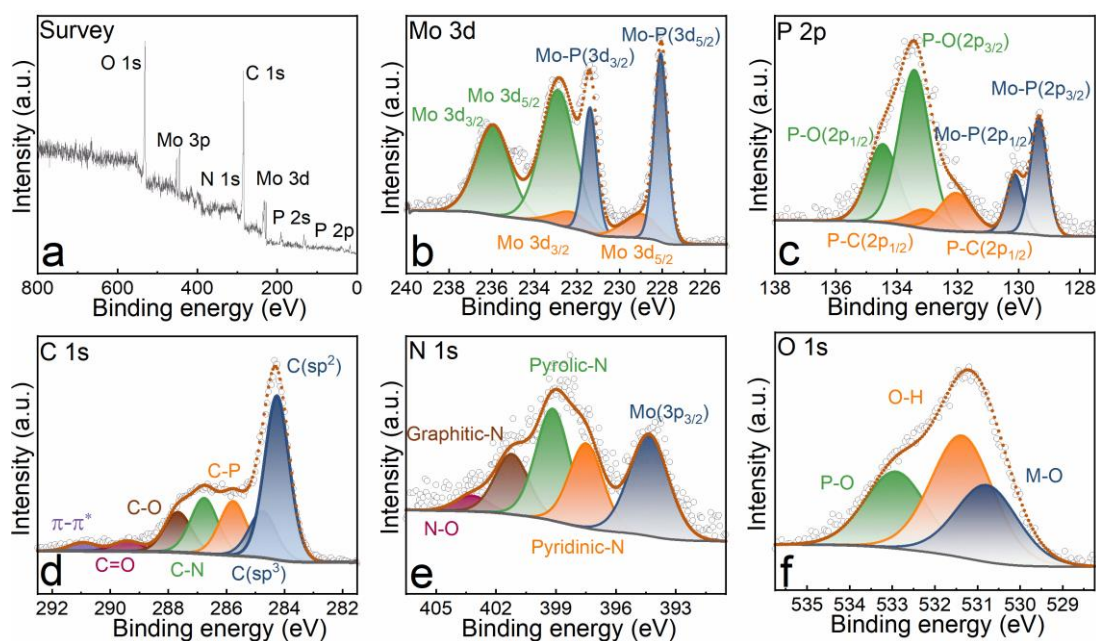


Figure 3.39 High-resolution X-ray photoelectron spectroscopy spectra of (a) survey spectrum, (b) Mo 3d, (c) P 2p, (d) C 1s, (e) N 1s, and (f) O 1s of MoP@NPC/CNT-900.

Furthermore, N<sub>2</sub> adsorption–desorption tests were performed to investigate the SSAs and porosity properties of the as-synthesized samples. The surface area is determined by the BET method and the pore size distribution calculated by non-local density functional theory (NLDFT) models. As displayed in Figure 3.40a, the N<sub>2</sub> sorption isotherms of pure NPC/CNT-900 and MoP@NPC/CNT-900 displayed characteristic H4 hysteresis loop features, indicating a mesopores structure. Compared with NPC/CNT-900, the MoP@NPC/CNT-900 is analyzed that there is a major decrease in SSA from (934.046 m<sup>2</sup> g<sup>-1</sup>) to (278.103 m<sup>2</sup> g<sup>-1</sup>) due to the introduction of MoP. Compared with the bare MoP sample, the BET



surface areas of the carbon containing samples (NPC/CNT-900 and MoP@NPC/CNT-900) are much higher, which further proves that carbon serves as a promising porous substrate to offer faster mass transport channels and expose abundant reaction active sites. In another view, the pore size distribution analysis of MoP@NPC/CNT-900 is shown in Figure 3.40b, which reveals an average pore diameter of 4.903 nm. After MoP loading, a decrease in pore size distribution is observed compared with NPC/CNT-900. The MoP loading causes partial reconstruction of the porous structure and may block the micropore opening which results in the creation of more mesopores and widening the average pore radii from 2.979 nm of NPC/CNT-900 to 4.903 nm of MoP@NPC/CNT-900. Besides, some of the mesopores result from the stacking of MoP QDs, as confirmed by the HR-TEM images. Such high surface area with abundant mesopores of the as-prepared MoP@NPC/CNT-900 can be predictably favourable for electrochemical catalytic reactions.

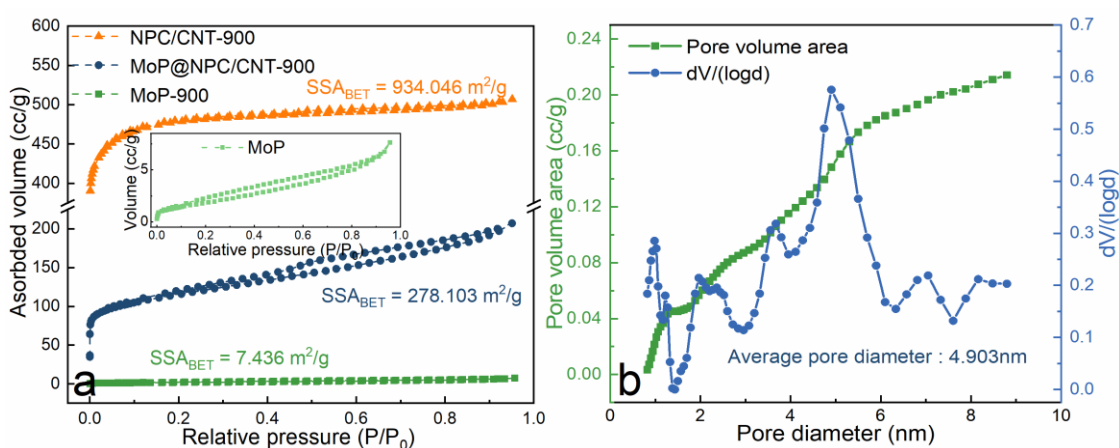


Figure 3.40  $N_2$  adsorption–desorption isotherms of MoP-900, NPC/CNT-900, and MoP@NPC/CNT-900, pore size distribution curve and pore volume area curve of MoP@NPC/CNT-900.

The catalytic HER activity of the synthesized materials were systematically evaluated by using a three-electrode cell in 0.5 M  $H_2SO_4$  solution. In order to investigate the influence of the MoP content, the HER performance of the samples with different MoP loadings and the control samples of bare MoP-900 and NPC/CNT-900 were characterized under the same condition. The representative polarization curves without  $iR$  corrections are exhibited in Figure 3.41a. Both NPC/CNT-900 and MoP-900 samples show negligible HER activity, whereas, the electrocatalytic HER performance is significantly improved after the incorporation of MoP species into the carbon substrate. Moreover, the increasing loading amount of MoP has a substantial influence on the catalytic properties, suggesting strong synergistic effects between the two different components. Among the catalysts, the MoP@NPC/CNT-900 gives the best activity and demonstrates an overpotential of 155 mV to deliver a current density of  $10 \text{ mA cm}^{-2}$ , which is much lower than that of 0.5MoP@NPC/CNT-900 (197 mV), 0.75MoP@NPC/CNT-900 (182 mV), bare NPC/CNT-900 and bare MoP-900. As expected, with further increasing of amount of

MoP, the overpotentials of 1.25MoP@NPC/CNT-900 (167 mV) and 1.5MoP@NPC/CNT-900 (171 mV) increase and result in an inferior HER performance compared with that of MoP@NPC/CNT-900. This finding is attributed to the improper proportion between MoP and carbon species, which influences the conductivity and intrinsic properties of the final material. This phenomenon is proved by the HR-TEM images as shown in Figure 3.42 and the XRD patterns in Figure 3.43, where higher MoP loading leads to severe aggregation and to an excess growth of the MoP nanospheric particles (the diameter becomes larger than 10 nm) and thus reduces the proportion of conductive carbon species, causing degradation of the catalytic performance.

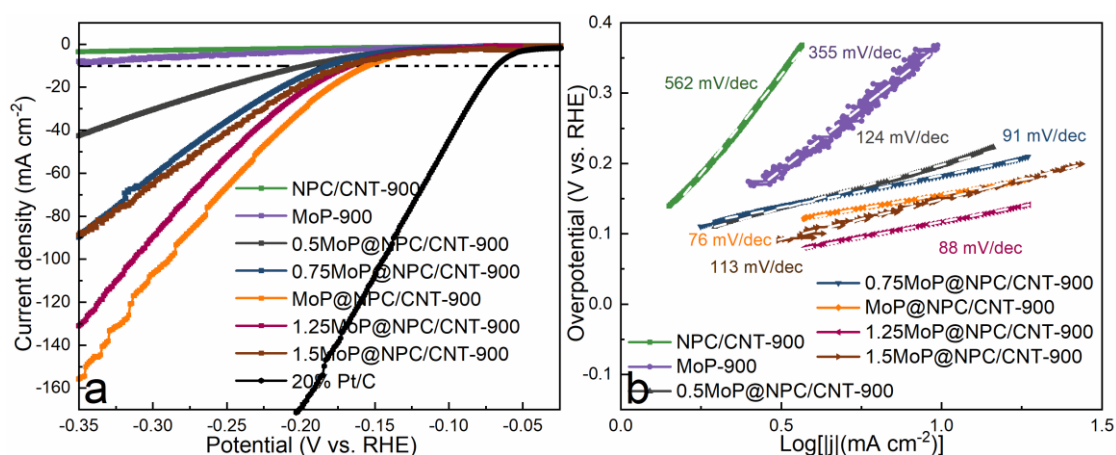


Figure 3.41 (a) Polarization curves and (b) Tafel plots of the samples annealed at 900 °C with various amounts of MoP, bare NPC/CNT, and bare MoP in 0.5 M H<sub>2</sub>SO<sub>4</sub>.

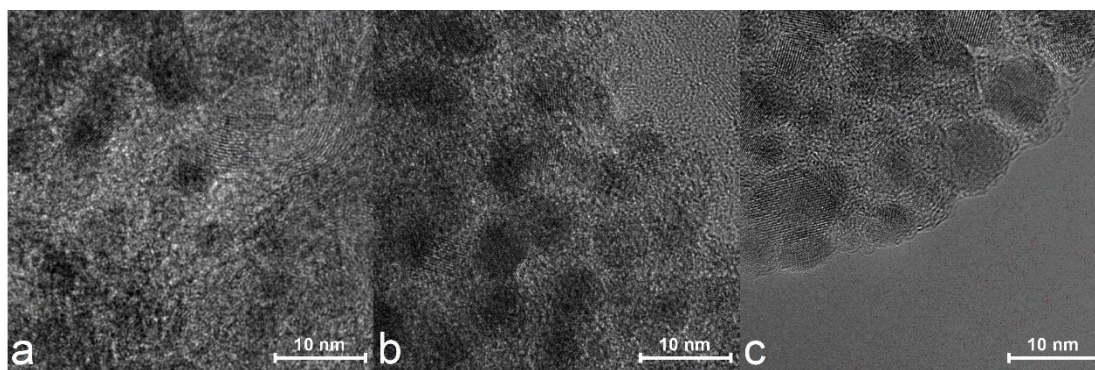


Figure 3.42 HR-TEM images of (a) 0.5MoP@NPC/CNT-900, (b) MoP@NPC/CNT-900, and (c) 1.5MoP@NPC/CNT-900.

Furthermore, the HER kinetics have been disclosed by corresponding Tafel plots. As well-known, a smaller value of the slope of the curve means a faster HER process. Thus, as displayed in Figure 3.41b, the MoP@NPC/CNT-900 sample shows an obviously lower Tafel slope of 76 mV dec<sup>-1</sup>, which is in the range between 40 and 120 mV dec<sup>-1</sup>, indicating that Volmer-Heyrovsky reaction mechanism dominates the reaction, in which the hydrogen desorption step is the rate-determining step.<sup>227-229</sup> In contrast,

higher Tafel slopes of 88, 91, 113, 124, 355 and 562  $\text{mV dec}^{-1}$  for 1.25MoP@NPC/CNT-900, 0.75MoP@NPC/CNT-900, 1.5MoP@NPC/CNT-900, 0.5MoP@NPC/CNT-900, MoP-900, and NPC/CNT-900 are obtained, respectively, indicating the superior catalytic kinetic performance of MoP@NPC/CNT-900 over that of all control samples.<sup>230</sup>

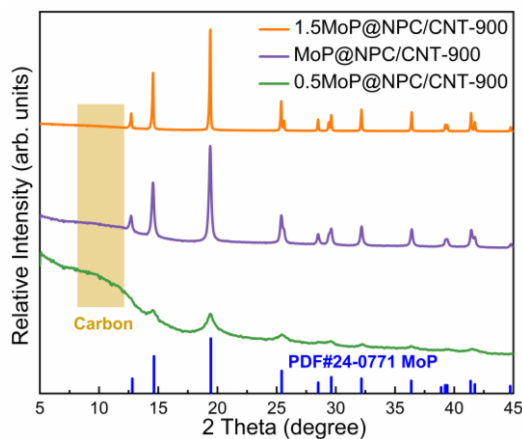


Figure 3.43 XRD patterns of 0.5MoP@NPC/CNT-900, MoP@NPC/CNT-900, and 1.5MoP@NPC/CNT-900.

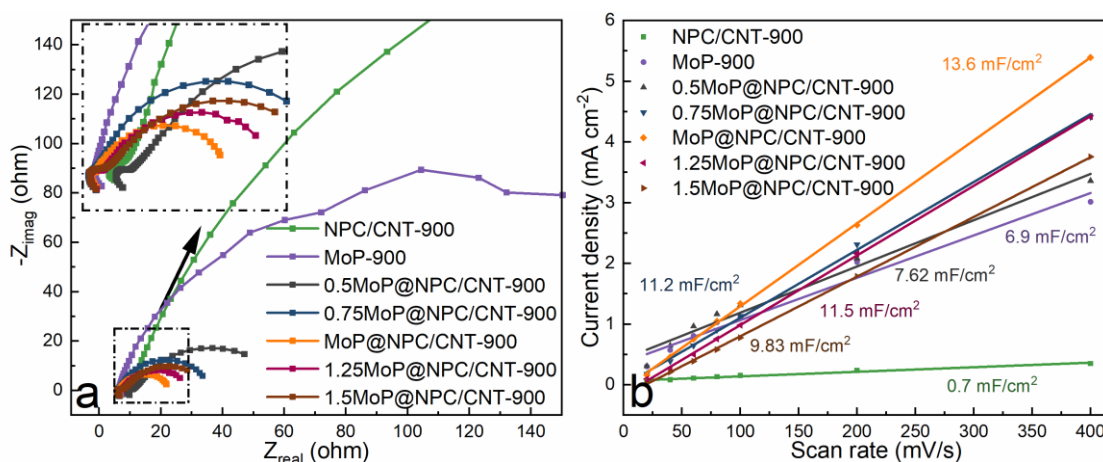


Figure 3.44 (a) EIS Nyquist plots (inset is the partially enlarged image) and (b) current as a function of scan rate of the samples annealed at 900 °C with varying amounts of molybdate salts, NPC/CNT-900, and MoP-900.

EIS measurements were conducted to study the electrode kinetics and the electrical conductivity at an overpotential of 40 mV from 1000 KHz to 1 Hz. It is well-known that  $R_{ct}$  is associated with the electrocatalytic kinetics at the electrocatalyst/electrolyte interface, and a smaller value indicates a faster electron transfer capacity of the material. According to the Nyquist plots shown in Figure 3.44a, the diameter of the arc notes represents the  $R_{ct}$  value. The  $R_{ct}$  values of the hybrid materials are obviously lower than that of bare NPC/CNT-900 and MoP-900, implying that interfacial charge-transfer performance of the electrodes can be greatly improved through combining MoP nanoparticles with NPC/CNT-900. Comparing the hybrid materials with different amounts of MoP, the one with MoP@NPC/CNT-900 shows the smallest  $R_{ct}$  value of all the samples, which suggests an excellent

ability of charge transfer and favourable HER kinetics at the interface between MoP@NPC/CNT-900 and electrolyte.

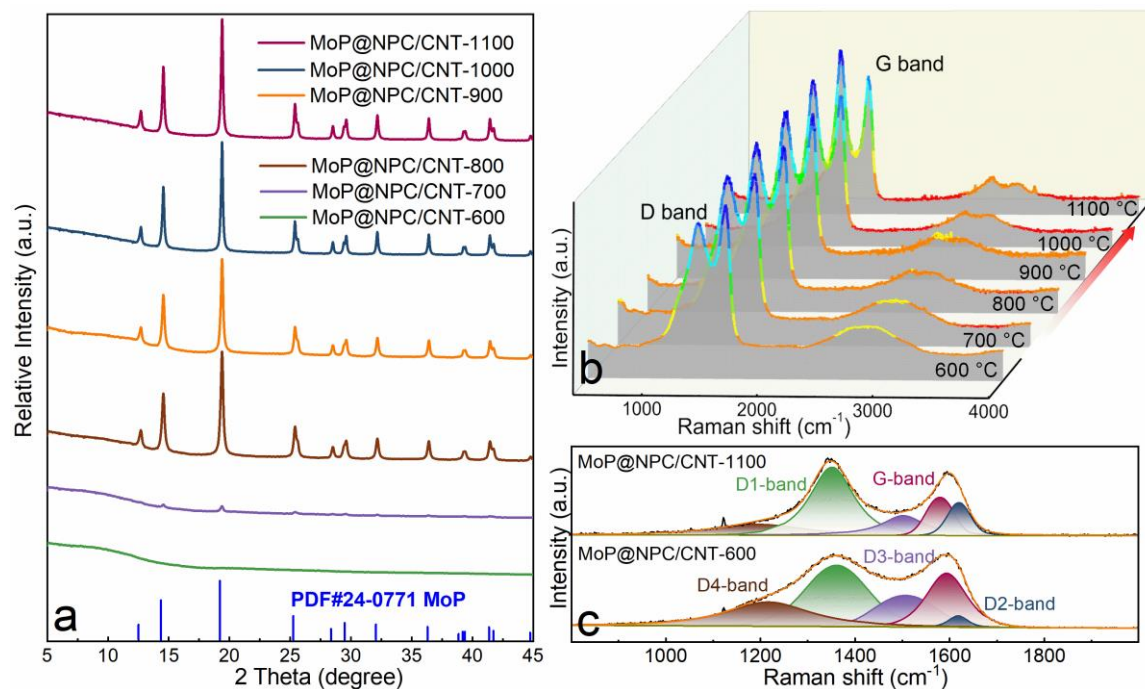


Figure 3.45 (a) XRD patterns and (b) Raman spectra of the MoP@NPC/CNT samples derived from different pyrolysis temperature, and (c) deconvolution of Raman spectra of samples MoP@NPC/CNT-600 and MoP@NPC/CNT-1100.

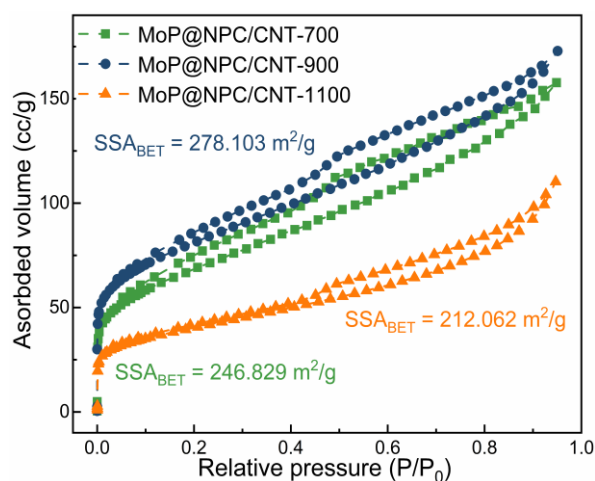


Figure 3.46  $N_2$  adsorption–desorption isotherms of MoP@NPC/CNT-700, MoP@NPC/CNT-900, and MoP@NPC/CNT-1100.

In general, the ECSA is effectively used to explore the electrocatalytically active surface area for electrocatalysts. The ECSAs are evaluated by calculating the  $C_{dl}$  from the cyclic voltammetry curves versus different scan rates in the non-Faradaic potential as depicted in Figure 3.44b. The slopes of the fitting plots correspond to the value of  $C_{dl}$  of each sample. The calculated  $C_{dl}$  value for

---

MoP@NPC/CNT-900 is  $13.6 \text{ mF cm}^{-2}$ , higher than those of 1.25MoP@NPC/CNT-900 ( $11.5 \text{ mF cm}^{-2}$ ), 0.75MoP@NPC/CNT-900 ( $11.2 \text{ mF cm}^{-2}$ ), 1.5MoP@NPC/CNT-900 ( $9.8 \text{ mF cm}^{-2}$ ), 0.5MoP@NPC/CNT-900 ( $7.6 \text{ mF cm}^{-2}$ ), MoP-900 ( $6.9 \text{ mF cm}^{-2}$ ), and NPC/CNT-900 ( $0.7 \text{ mF cm}^{-2}$ ). The analysed values prove that MoP@NPC/CNT-900 exposes more effective active sites at solid–liquid interface, resulting in the highest electrochemical HER activity.

To study the influence of the pyrolysis temperature and the formation mechanism, the optimum for MoP@NPC/CNT was investigated through a comparison of samples carbonized from  $600 \text{ }^{\circ}\text{C}$  to  $1100 \text{ }^{\circ}\text{C}$ , denoted as MoP@NPC/CNT-X (X referenced as the pyrolysis temperature). The XRD patterns of samples derived from different pyrolysis temperatures are shown in Figure 3.45a. Under a relatively low temperature, the MoP@NPC/CNT-600 shows no clear peaks of the molybdenum related phase (Figure 3.45a). Additionally, weak peaks originating from MoP (PDF#24-0771) for MoP@NPC/CNT-700 are detected, owing to the low crystallinity and incomplete transformation, which indicates that MoP phase start to form at around  $700 \text{ }^{\circ}\text{C}$ . When the temperature rose to  $800 \text{ }^{\circ}\text{C}$ , sharp MoP reflections are identified. With further increasing annealing temperature, MoP QDs nanospheres emerge as shown in the HR-TEM images (Figure 3.38a and 3.38b). However, a carbonization temperature above  $1000 \text{ }^{\circ}\text{C}$  destroys the porous carbon networks to some extent and causes heavy agglomeration of the MoP particles as well. Therefore, further  $\text{N}_2$  adsorption and desorption test proved the changes of carbon networks as shown in Figure 3.46. The BET surface area of MoP@NPC/CNT-1100 is greatly decreased compared with that of MoP@NPC/CNT-900, and the smaller BET surface area value of MoP@NPC/CNT-600 may be attributed to the incomplete decomposition of the carbon precursor and the incomplete escape of gaseous hydrocarbon species which are responsible for the formation of pores during the pyrolysis. Raman spectroscopy (Figure 3.45b) shows the transformation of the carbon species with increasing annealing temperature. The first-order Raman spectra of MoP@NPC/CNT-600 and MoP@NPC/CNT-1100 were fitted to sums of functions as D1-band, D2-band, D3-band, D4-band, and G-band shown in Figure 3.45c as the reference to track the changing trend of the series of samples.<sup>152,231</sup> According to the literature, the D3-band is confirmed related to amorphous carbon species, and the intensity clearly decreases as the temperature increasing from  $600$  to  $1100 \text{ }^{\circ}\text{C}$ . The D1-band is related to disordered graphitic lattices of  $\text{sp}^2\text{-sp}^3$  bonds. Compared with the MoP@NPC/CNT-1100 sample, the larger area of the fitted D1-band peak of MoP@NPC/CNT-600 agrees well with an incomplete decomposition of the carbon precursor. Moreover, the intensities of the D-band and D2-band are proportional to the grain boundaries, carbon vacancies, and hybridization caused by the heteroatom doping, which can give the clarification of the increasing D and D2-band with increasing carbonization temperature.<sup>232</sup>

Figure 3.47a exhibits the polarization curve of different samples annealed at different temperatures

to investigate the HER performance. It is obvious that the MoP@NPC/CNT-900 displays superior performance with an overpotential of 155 mV to obtain a current density of 10 mA cm<sup>-2</sup>. Comparatively, the MoP@NPC/CNT-800, MoP@NPC/CNT-1000, MoP@NPC/CNT-1100, and MoP@NPC/CNT-700 give larger overpotential values of 177, 172, 176, and 286 mV, respectively. The MoP@NPC/CNT-600 shows nearly no HER performance. Thus, the 900 °C is the optimal temperature to form a heteroatom-doped carbon supported proper size of MoP particles, which also promotes the favourable synergistic interactions for electrochemical reactions. Additionally, Tafel slopes were derived from the polarization curves as shown in Figure 3.47b, the material obtained at 900 °C presents the smallest value compared with samples obtained under different temperatures, indicating an enhanced electrocatalytic performance and a relatively rapid increasing hydrogen production rate with rising potential applied for the MoP@NPC/CNT-900 sample.

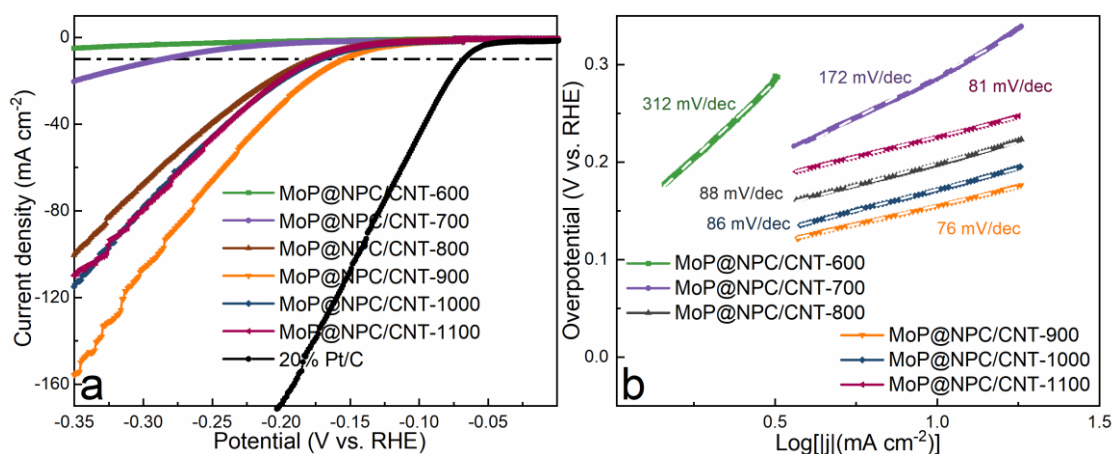


Figure 3.47 (a) Polarization curves and (b) Tafel plots of the MoP@NPC/CNT samples annealed at different temperatures in 0.5 M H<sub>2</sub>SO<sub>4</sub> electrolyte.

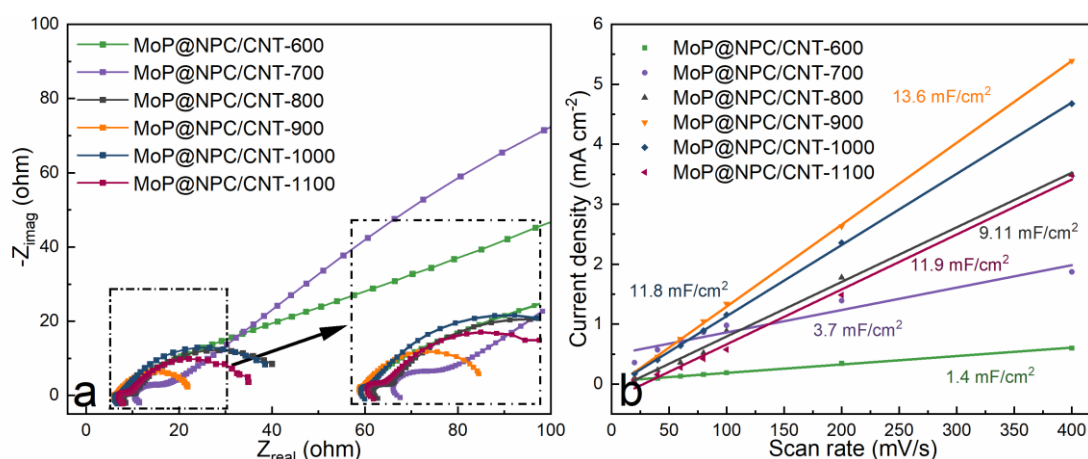


Figure 3.48 (a) EIS Nyquist plots (inset is the partially enlarged image) and (b) current as a function of scan rate for the MoP@NPC/CNT samples annealed at different temperatures in 0.5 M H<sub>2</sub>SO<sub>4</sub> electrolyte.

Additionally, the electrode kinetics have been also characterized by EIS. The Nyquist plots (Figure 3.48a)

reveals the resistances of charge transfer for different samples, likewise, the MoP@NPC/CNT-900 exhibits the smaller charge transfer resistance than those of the control samples, confirming that MoP@NPC/CNT-900 possesses a faster charge transfer capacity and a favourable kinetic regarding the HER process. Furthermore, the ECSA was evaluated by calculating  $C_{dl}$  (Figure 3.48b). Accordingly, the ECSA value of MoP@NPC/CNT-900 is the highest among all the samples, confirming that MoP@NPC/CNT-900 possesses more exposed electrocatalytically active sites and results in a higher electrochemical HER activity.

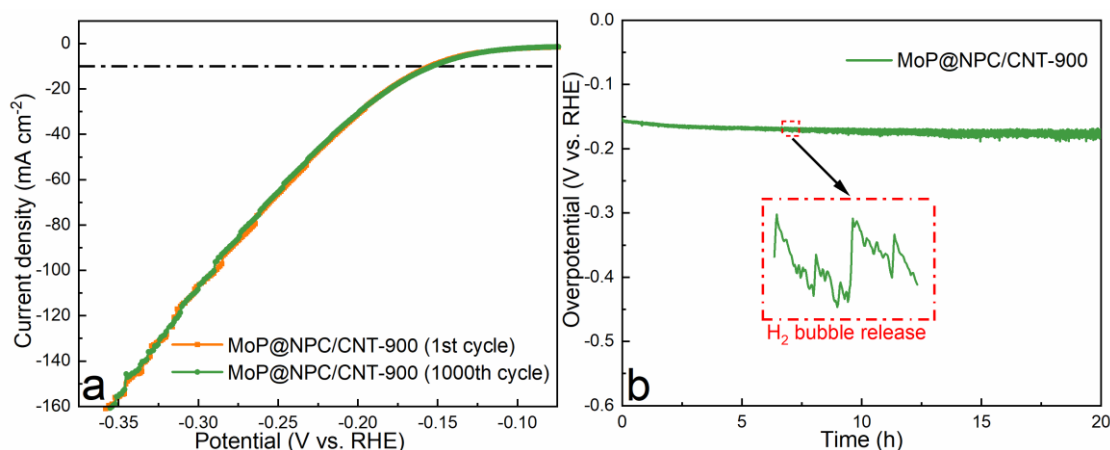


Figure 3.49 (a) Polarization curves of MoP@NPC/CNT-900 samples initially and after 1000 cycles, and (b) the time-dependent overpotential at constant current density input for 20 h in 0.5 M H<sub>2</sub>SO<sub>4</sub> electrolyte.

Durability is another vital criterion to assess the property of a catalyst. MoP@NPC/CNT-900 was first tested by performing continuous CV for 1000 cycles as shown in Figure 3.49a. The MoP@NPC/CNT-900 electrode exhibits an excellent durability, since the overpotential remains nearly unchanged to afford a current density of 10 mA cm<sup>-2</sup>, but to achieve a higher current density, the overpotential is slightly increased. Then, the stability of the catalyst was further checked for 20 h via a chronopotentiometry measurement. The overpotential required to drive the current density of 10 mA cm<sup>-2</sup> was observed to remain constant at ~160 mV for 20 h (Figure 3.49b). Both results demonstrate that the MoP@NPC/CNT-900 has superior HER stability under acidic electrolyte conditions.

Importantly, the HER performance for MoP@NPC/CNT-900 was also tested in 1.0 M KOH solution as shown in Figure 3.50. For comparison purposes, the samples annealed at different temperatures were tested under the same conditions. Likewise, the MoP@NPC/CNT-900 electrode displays the smallest overpotential of 131 mV to reach a current density of 10 mA cm<sup>-2</sup> and the smallest Tafel slope of 73 mV dec<sup>-1</sup> of all the control samples. As shown in Figure 3.51, the MoP@NPC/CNT-900 electrode exhibits lower  $R_{ct}$  value, indicating the faster charge-transport kinetics for the HER. Furthermore, MoP@NPC/CNT-900 has the highest  $C_{dl}$  value of 12.8 mF cm<sup>-2</sup>, which also reveals that more active sites are exposed at the surface. As a result, the alkaline electrocatalytic HER process is promoted.

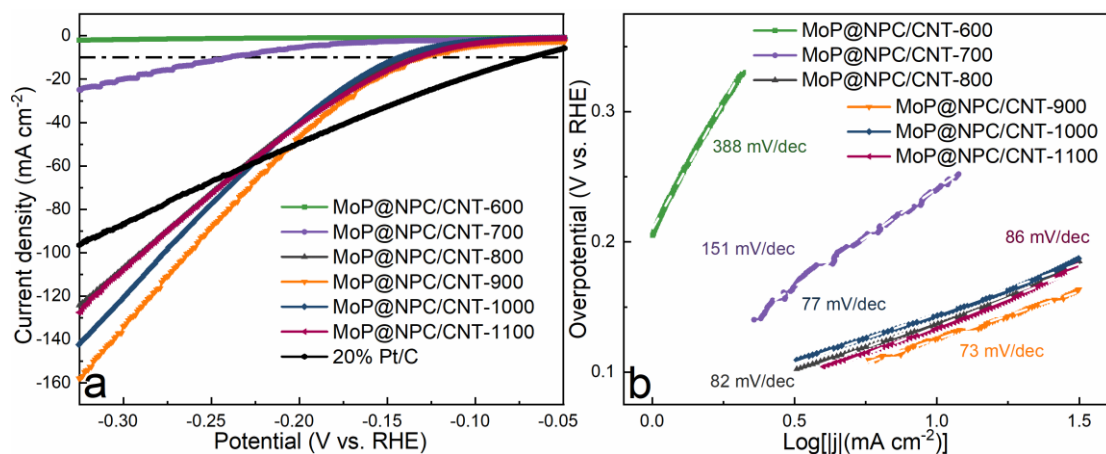


Figure 3.50 (a) Polarization curves and (b) Tafel plots of the MoP@NPC/CNT samples annealed at different temperatures in 1 M KOH electrolyte.

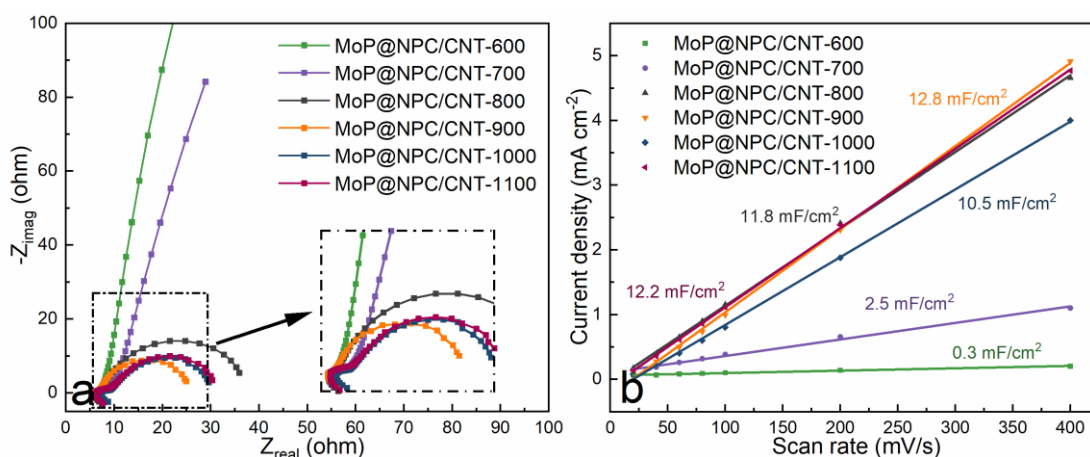


Figure 3.51 (a) EIS Nyquist plots (inset is the partially enlarged image) and (b) capacitive current as a function of scan rate the MoP@NPC/CNT samples annealed at different temperatures in 1 M KOH electrolyte.

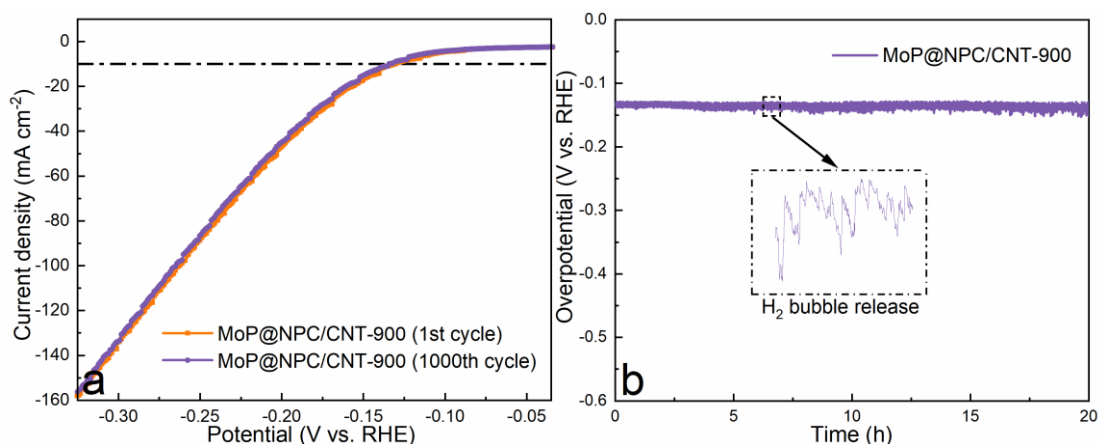


Figure 3.52 (a) Polarization curves of MoP@NPC/CNT-900 samples initially and after 1000 cycles, and (b) the time-dependent overpotential at constant current density input for 20 h in 1 M KOH electrolyte.

Lastly, MoP@NPC/CNT-900 also shows strong durability in the alkaline media as shown in Figure 3.52a



and 3.52b. The continuous CV test shows less than 10 mV decrease after 1000 cycles running. Simultaneously, the chronopotentiometry was also measured in alkaline solution at a constant current density ( $10 \text{ mA cm}^{-2}$ ). The electrode shows a super stable potential response for HER without significant degradation after 20 h continuous electrolysis. Overall, the as-prepared MoP@NPC/CNT-900 electrode exhibits a remarkable stable HER catalytic performance in both acidic and alkaline media.

Table 3.4 Summary of HER overpotentials at  $-10 \text{ mA cm}^{-2}$  of some reported MoP-based catalysts.

Materials	Overpotential <sup>a</sup> (acidic)	Overpotential <sup>b</sup> (alkaline)	Ref.
MoP@PC	258 mV	-	233
MoP@NC	96 mV	149 mV	234
MoP@NPC/rGO	218 mV	-	235
MoP@PC/rGO	234.6 mV	-	236
MoC-MoP/BCNC NFs	158 mV	137 mV	237
MoP@PC-CNTs	220 mV	-	238
Mo <sub>2</sub> C/MoP@NPC	160 mV	169 mV	239
Mo <sub>2</sub> C-MoP NPC/CFP-800	85 mV	146 mV	240
N/C/MoP	169 mV	-	241
CoMoP-0.05	215 mV	-	242
MoP/CF	200 mV	-	243
<b>MoP@NPC/CNT-900</b>	<b>155 mV</b>	<b>131 mV</b>	<b>This work</b>

<sup>a</sup> Overpotential at a current density of  $-10 \text{ mA cm}^{-2}$  (based on electrode geometric area) under 0.5 M H<sub>2</sub>SO<sub>4</sub>.

<sup>b</sup> Overpotential at a current density of  $-10 \text{ mA cm}^{-2}$  (based on electrode geometric area) under 1 M KOH.

The performance of the as-prepared MoP@NPC/CNT-900 is comparable to some of the reported MoP-based electrocatalysts as shown in Table 3.4. Such superior catalytic activity and durability is mainly ascribed to the following features: i) A highly porous structure of MoP@NPC/CNT-900 exposes more active sites and facilitates the reaction kinetic in a unique channel-rich structure. ii) As the active MoP compounds, phosphorus serves as the proton-acceptor and Mo acts as the hydride-acceptor to facilitate the HER catalytic activity. iii) The carbon framework confines the growth of MoP quantum dots (<10 nm), which shortens the charge transfer length during the electrocatalysis. iv) The combination of MoP and highly conductive carbon species (such as CNTs and P and N co-doped carbon) largely accelerates the electron transfer between the electrode and surface compounds, which significantly improves the HER performance. v) the excellent durability is attributed to the carbon layer confined nanostructure of the active MoP phase, avoiding the contact with the harsh electrolyte.



---

---

## 4 Conclusions and Outlook

---

In the present research work, single-source-precursors (SSPs) were obtained from a facile and efficient coordination-chemical modification strategy via a one-pot reaction between different molecules (tannic acid (TA), polyethylenimine (PEI), phytic acid (PA) and transition metal sources), and then followed by a pyrolysis process to fabricate transition metal compounds (TMCs) encapsulated by heteroatom doped and highly porous carbon as potential electrocatalysts. Compared with the traditional synthesis method, the advantages of this synthesis strategy are as follows: (i) It is a universal strategy for most of transition metal alloys (TMAs)/carbon hybrids and transition metal phosphides (TMPs)/carbon hybrids; (ii) The environmental friendly PA and TA serve as the phosphorus and carbon source, thus other dangerous and poisonous phosphorus and expensive carbon sources are avoided; (iii) The one-pot reaction enables ideal tuning of the homogeneous composition of the SSPs and the derived TMPs/TMAs carbon hybrid; (iv) The *in-situ* formation of multiplex carbon matrix derived from organic ligands prevents the agglomeration of TMCs particles, and the nanopores are *in-situ* generated without additional surfactants to expose more active sites. Based on the above metrics, the obtained electrocatalysts exhibit excellent electrocatalytic activity and stability for the HER and/or OER process.

The first part (Section 3.1) of the present research focused on *in-situ* formed metallic nanoparticles encapsulated by a carbon shell and embedded in a highly defective carbon and carbon nanotube composite support. The obtained FeNi@NC-900 hybrid nanocomposite has a low overpotential of 310 mV at a current density of 10 mA cm<sup>-2</sup> together with a low Tafel slope of 45 mV dec<sup>-1</sup>, low charge transfer resistance, high electrochemical active surface area (ECSA) and excellent durability. The *in-situ* formed active metallic nanoparticles are embedded in a highly defective carbon and carbon nanotube composite support, facilitating a fast electron transport and corrosion protection of the alloys under the alkaline electrolyte during OER.

The second part (Section 3.2) of the present research studied core-shell structured nanoparticles (binary transition metal phosphides as core and carbon as shell) dispersed in highly defective N and P co-doped carbon matrix (FeNiP@NPC). The compound FeNiP@NPC-900 displays promising electrocatalytic performance for both HER and OER, with a low overpotential of 191 mV and 278 mV, respectively. The impressive performance is attributed to the high electrochemical active surface area and abundant active sites exposure. Meanwhile, the FeNiP@NPC-900 exhibits strong durability and robustness in acid and alkaline electrolytes owing to the core-shell nanostructure. Compared with the monometallic phosphide samples (FeP@NPC and NiP@NPC), the robust heterointerface and synergetic effect of FeNiP@NPC between binary TMPs and defective-rich carbon ensure a fast reaction kinetic and charge transfer, which promote more effective hydrogen and oxygen evolution.

The third part (Section 3.3) investigated MoP quantum dots (QDs) encapsulated by N and P co-doped highly porous carbon and carbon nanotube matrix (MoP@NPC/CNT-900) synthesized via the facile annealing of well-designed single-source-precursors. The obtained MoP@NPC/CNT-900 hybrids show highly efficient electrocatalytic activity and long-term durability for HER in acidic and alkaline electrolytes, which can be ascribed to the synergistic effect between active MoP QDs and defective carbon. Moreover, the dual N and P doped carbon shell not only enhances the electronic conductivity of the material but also protects the MoP QDs from potential corrosion during the electrocatalytic process. This work proposes a feasible strategy to design and optimize MoP and carbon-based electrocatalysts by precisely tuning the single-source-precursor on a molecular level. The MoP@NPC/CNT-900 catalyst exhibits outstanding HER performance with a low overpotential of 155 mV and 131 mV at the current density of  $10 \text{ mA cm}^{-2}$ , Tafel slopes of  $76 \text{ mV dec}^{-1}$  and  $73 \text{ mV dec}^{-1}$ , in  $0.5 \text{ M H}_2\text{SO}_4$  and  $1.0 \text{ M KOH}$ , respectively, as well as robust long-term durability in both acidic and alkaline conditions.

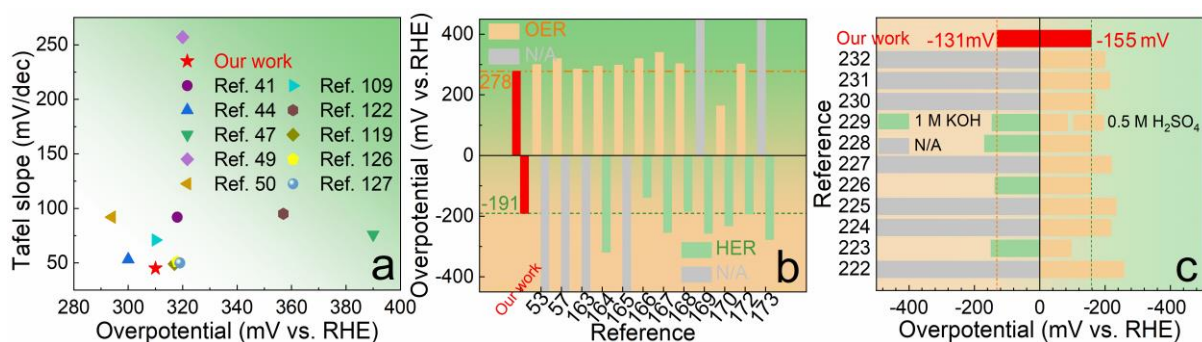


Figure 4.1 Comparative evaluations of our materials studied in above sections((a) Section 3.1, (b) Section 3.2, and (c) Section 3.3) with reported TMCs/carbon-based catalysts.

In summary, Comparative evaluations of our materials are shown in Figure 4.1. The present results not only show the innovative synthesis of outstanding TMCs/carbon hybrid electrocatalysts, but also broaden the insights into the design and electrocatalytic performance of TMCs encapsulated by a defective carbon nanocomposite shell. This facile and general process advances the development of transition metal-based hybrid material for potential energy storage and conversion in the near future.

---

---

## 5 References

---

- 1 Turner, J. A. Sustainable hydrogen production. *Science* **305**, 972-974 (2004).
- 2 Turner, J. A. A realizable renewable energy future. *Science* **285**, 687-689 (1999).
- 3 Zou, X. & Zhang, Y. Noble metal-free hydrogen evolution catalysts for water splitting. *Chemical Society Reviews* **44**, 5148-5180 (2015).
- 4 Kemppainen, E. *et al.* Scalability and feasibility of photoelectrochemical H<sub>2</sub> evolution: the ultimate limit of Pt nanoparticle as an HER catalyst. *Energy & Environmental Science* **8**, 2991-2999 (2015).
- 5 Chen, W.-F. *et al.* Recent developments in transition metal carbides and nitrides as hydrogen evolution electrocatalysts. *Chemical Communications* **49**, 8896-8909 (2013).
- 6 Pu, Z. *et al.* Transition-metal phosphides: activity origin, energy-related electrocatalysis applications, and synthetic strategies. *Advanced Functional Materials* **30**, 2004009 (2020).
- 7 Chen, Z. *et al.* Recent advances in transition metal-based electrocatalysts for alkaline hydrogen evolution. *Journal of Materials Chemistry A* **7**, 14971-15005 (2019).
- 8 Liu, P. F. *et al.* Activation strategies of water-splitting electrocatalysts. *Journal of Materials Chemistry A* **8**, 10096-10129 (2020).
- 9 Zhao, G. *et al.* Boosting electrochemical water oxidation: the merits of heterostructured electrocatalysts. *Journal of Materials Chemistry A* **8**, 6393-6405 (2020).
- 10 Wang, Y.-J. *et al.* Carbon-supported Pt-based alloy electrocatalysts for the oxygen reduction reaction in polymer electrolyte membrane fuel cells: particle size, shape, and composition manipulation and their impact to activity. *Chemical Reviews* **115**, 3433-3467 (2015).
- 11 Yan, Y. *et al.* Modification strategies on transition metal-based electrocatalysts for efficient water splitting. *Journal of Energy Chemistry* **58**, 446-462 (2021).
- 12 Yin, X. *et al.* Core-shell nanostructured electrocatalysts for water splitting. *Nanoscale* **12**, 15944-15969 (2020).
- 13 Wang, S. *et al.* Hydrogen production from water electrolysis: role of catalysts. *Nano Convergence* **8**, 1-23 (2021).
- 14 Li, W. *et al.* Integrated transition metal and compounds with carbon nanomaterials for electrochemical water splitting. *Journal of Materials Chemistry A* **9**, 3786-3827 (2021).
- 15 Skúlason, E. *et al.* Modeling the electrochemical hydrogen oxidation and evolution reactions on the basis of density functional theory calculations. *The Journal of Physical Chemistry C* **114**, 18182-18197 (2010).
- 16 Nørskov, J. K. *et al.* Trends in the exchange current for hydrogen evolution. *Journal of the Electrochemical Society* **152**, J23 (2005).
- 17 Strmcnik, D. *et al.* Design principles for hydrogen evolution reaction catalyst materials. *Nano Energy* **29**, 29-36 (2016).
- 18 Suen, N.-T. *et al.* Electrocatalysis for the oxygen evolution reaction: recent development and future perspectives. *Chemical Society Reviews* **46**, 337-365 (2017).
- 19 Fabbri, E. *et al.* Developments and perspectives of oxide-based catalysts for the oxygen evolution reaction. *Catalysis Science & Technology* **4**, 3800-3821 (2014).
- 20 Anantharaj, S. *et al.* Precision and correctness in the evaluation of electrocatalytic water splitting: revisiting activity parameters with a critical assessment. *Energy & Environmental Science* **11**, 744-771 (2018).
- 21 Lu, J. *et al.* Carbon-Encapsulated Electrocatalysts for the Hydrogen Evolution Reaction. *Electrochemical Energy Reviews* **2**, 105-127 (2018).
- 22 Huang, Z. *et al.* Cobalt phosphide nanorods as an efficient electrocatalyst for the hydrogen evolution reaction. *Nano Energy* **9**, 373-382 (2014).
- 23 Chang, B.-Y. *et al.* Electrochemical impedance spectroscopy. *Annual Review of Analytical Chemistry* **3**, 207-229 (2010).
- 24 Liu, Z. *et al.* A nitrogen-doped CoP nanoarray over 3D porous Co foam as an efficient bifunctional electrocatalyst for overall water splitting. *Journal of Materials Chemistry A* **7**,

- 13242-13248 (2019).
- 25 Ma, S.-Y. *et al.* Synthesis of low Pt-based quaternary PtPdRuTe nanotubes with optimized incorporation of Pd for enhanced electrocatalytic activity. *Journal of the American Chemical Society* **139**, 5890-5895 (2017).
- 26 Wei, C. *et al.* Approaches for measuring the surface areas of metal oxide electrocatalysts for determining their intrinsic electrocatalytic activity. *Chemical Society Reviews* **48**, 2518-2534 (2019).
- 27 Chen, Y.-Y. *et al.* Pomegranate-like N, P-doped Mo<sub>2</sub>C@C nanospheres as highly active electrocatalysts for alkaline hydrogen evolution. *ACS Nano* **10**, 8851-8860 (2016).
- 28 Zhang, L. *et al.* Fe<sub>3</sub>C nanorods encapsulated in N-doped carbon nanotubes as active electrocatalysts for hydrogen evolution reaction. *Electrocatalysis* **9**, 264-270 (2018).
- 29 Chen, Z. *et al.* Eutectoid-structured WC/W<sub>2</sub>C heterostructures: A new platform for long-term alkaline hydrogen evolution reaction at low overpotentials. *Nano Energy* **68**, 104335 (2020).
- 30 Shalom, M. *et al.* Nickel nitride as an efficient electrocatalyst for water splitting. *Journal of Materials Chemistry A* **3**, 8171-8177 (2015).
- 31 Yuan, W. *et al.* Interfacial engineering of cobalt nitrides and mesoporous nitrogen-doped carbon: toward efficient overall water-splitting activity with enhanced charge-transfer efficiency. *ACS Energy Letters* **5**, 692-700 (2020).
- 32 Li, G. *et al.* Plasma transforming Ni(OH)<sub>2</sub> nanosheets into porous nickel nitride sheets for alkaline hydrogen evolution. *ACS Applied Materials & Interfaces* **12**, 5951-5957 (2020).
- 33 Mishra, I. K. *et al.* Hierarchical CoP/Ni<sub>5</sub>P<sub>4</sub>/CoP microsheet arrays as a robust pH-universal electrocatalyst for efficient hydrogen generation. *Energy & Environmental Science* **11**, 2246-2252 (2018).
- 34 Ji, P. *et al.* Double metal diphosphide pair nanocages coupled with P-doped carbon for accelerated oxygen and hydrogen evolution kinetics. *ACS Applied Materials & Interfaces* **12**, 727-733 (2019).
- 35 Deng, J. *et al.* Triggering the electrocatalytic hydrogen evolution activity of the inert two-dimensional MoS<sub>2</sub> surface via single-atom metal doping. *Energy & Environmental Science* **8**, 1594-1601 (2015).
- 36 Voiry, D. *et al.* Enhanced catalytic activity in strained chemically exfoliated WS<sub>2</sub> nanosheets for hydrogen evolution. *Nature Materials* **12**, 850-855 (2013).
- 37 Zhang, G. *et al.* Iron-facilitated surface reconstruction to in-situ generate nickel-iron oxyhydroxide on self-supported FeNi alloy fiber paper for efficient oxygen evolution reaction. *Applied Catalysis B: Environmental* **286**, 119902 (2021).
- 38 Hou, G. *et al.* CoNi Nano-alloys Modified Yolk-shell Structure Carbon Cage via Saccharomyces as Carbon Template for Efficient Oxygen Evolution Reaction. *Applied Catalysis B: Environmental*, 121551 (2022).
- 39 Park, J.-H. *et al.* FeCo nanoparticles with different compositions as electrocatalysts for oxygen evolution reaction in alkaline solution. *Applied Surface Science* **589**, 153041 (2022).
- 40 Zhao, D. *et al.* Synergistically interactive pyridinic-N–MoP sites: identified active centers for enhanced hydrogen evolution in alkaline solution. *Angewandte Chemie* **132**, 9067-9075 (2020).
- 41 Deng, J. *et al.* Enhanced electron penetration through an ultrathin graphene layer for highly efficient catalysis of the hydrogen evolution reaction. *Angewandte Chemie International Edition* **54**, 2100-2104 (2015).
- 42 Chen, X. *et al.* A hierarchical architecture of Fe/Co/Ni-doped carbon nanotubes/nanospheres grafted on graphene as advanced bifunctional electrocatalyst for Zn-Air batteries. *Journal of Alloys and Compounds* **873**, 159833 (2021).
- 43 Shui, H. *et al.* In Situ Incorporation Strategy for Bimetallic FeCo-Doped Carbon as Highly Efficient Bifunctional Oxygen Electrocatalysts. *ChemElectroChem* **5**, 1401-1406 (2018).
- 44 Meng, H.-L. *et al.* Coordination regulated pyrolysis synthesis of ultrafine FeNi/(FeNi)<sub>9</sub>S<sub>8</sub> nanoclusters/nitrogen, sulfur-codoped graphitic carbon nanosheets as efficient bifunctional oxygen electrocatalysts. *Journal of Colloid and Interface Science* **610**, 573-582 (2022).

- 45 Lei, Y. *et al.* Electronic structure tuning of FeCo nanoparticles embedded in multi-dimensional carbon matrix for enhanced bifunctional oxygen electrocatalysis. *Journal of Alloys and Compounds* **853**, 157070 (2021).
- 46 Shah, S. A. *et al.* Thermal synthesis of FeNi@nitrogen-doped graphene dispersed on nitrogen-doped carbon matrix as an excellent electrocatalyst for oxygen evolution reaction. *ACS Applied Energy Materials* **2**, 4075-4083 (2019).
- 47 Najam, T. *et al.* Electron penetration from metal core to metal species attached skin in nitrogen-doped core-shell catalyst for enhancing oxygen evolution reaction. *Electrochimica Acta* **327**, 134939 (2019).
- 48 Yang, Y. *et al.* Non-precious alloy encapsulated in nitrogen-doped graphene layers derived from MOFs as an active and durable hydrogen evolution reaction catalyst. *Energy & Environmental Science* **8**, 3563-3571 (2015).
- 49 Cao, F. *et al.* Electrospinning synthesis of transition metal alloy nanoparticles encapsulated in nitrogen-doped carbon layers as an advanced bifunctional oxygen electrode. *Journal of Materials Chemistry A* **8**, 7245-7252 (2020).
- 50 Ge, R. *et al.* Electrocatalyst nanoarchitectonics with molybdenum-cobalt bimetallic alloy encapsulated in nitrogen-doped carbon for water splitting reaction. *Journal of Alloys and Compounds* **904**, 164084 (2022).
- 51 Wang, Y. *et al.* Hierarchical peony-like FeCo-NC with conductive network and highly active sites as efficient electrocatalyst for rechargeable Zn-air battery. *Nano Research* **13**, 1090-1099 (2020).
- 52 Han, Z. *et al.* Transitional metal alloyed nanoparticles entrapped into the highly porous N-doped 3D honeycombed carbon: A high-efficiency bifunctional oxygen electrocatalyst for boosting rechargeable Zn-air batteries. *International Journal of Hydrogen Energy* **46**, 19385-19396 (2021).
- 53 Ghouri, Z. K. *et al.* Theoretical and experimental investigations of Co-Cu bimetallic alloys-incorporated carbon nanowires as an efficient bi-functional electrocatalyst for water splitting. *Journal of Industrial and Engineering Chemistry* **96**, 243-253 (2021).
- 54 Liu, J. *et al.* N-doped hollow porous carbon spheres@CoCuFe alloy nanospheres as novel non-precious metal electrocatalysts for HER and OER. *International Journal of Hydrogen Energy* **47**, 5947-5960 (2022).
- 55 Liu, T. *et al.* Designing transition metal alloy nanoparticles embedded hierarchically porous carbon nanosheets as high-efficiency electrocatalysts toward full water splitting. *Journal of Colloid and Interface Science* **537**, 280-294 (2019).
- 56 Wang, S. *et al.* Trifunctional electrocatalyst of N-doped graphitic carbon nanosheets encapsulated with CoFe alloy nanocrystals: The key roles of bimetal components and high-content graphitic-N. *Applied Catalysis B: Environmental* **298**, 120512 (2021).
- 57 Zhang, Q. *et al.* CoNi based alloy/oxides@N-doped carbon core-shell dendrites as complementary water splitting electrocatalysts with significantly enhanced catalytic efficiency. *Applied Catalysis B: Environmental* **254**, 634-646 (2019).
- 58 Qiao, L. *et al.* Copper–nickel embedded into a nitrogen-doped carbon octahedron as an effective bifunctional electrocatalyst. *Inorganic Chemistry Frontiers* **5**, 2276-2283 (2018).
- 59 Lv, Y. *et al.* Homogeneously distributed NiFe alloy nanoparticles on 3D carbon fiber network as a bifunctional electrocatalyst for overall water splitting. *ChemElectroChem* **6**, 2497-2502 (2019).
- 60 Tan, S. *et al.* Carbon wrapped bimetallic NiCo nanospheres toward excellent HER and OER performance. *Journal of Alloys and Compounds* **889**, 161528 (2021).
- 61 Manzoor, S. *et al.* Nanopetals shaped CuNi alloy with defects abundant active surface for efficient electrocatalytic oxygen evolution reaction and high performance supercapacitor applications. *Journal of Energy Storage* **55**, 105488 (2022).
- 62 Liu, P. *et al.* Catalysts for hydrogen evolution from the [NiFe] hydrogenase to the Ni<sub>2</sub>P (001) surface: the importance of ensemble effect. *Journal of the American Chemical Society* **127**,

- 14871-14878 (2005).
- 63 Jiang, M. *et al.* Ion-biosorption induced core-shell Fe<sub>2</sub>P@carbon nanoparticles decorated on N, P co-doped carbon materials for the oxygen evolution reaction. *Inorganic Chemistry Frontiers* **8**, 2385-2394 (2021).
- 64 Peng, Z. *et al.* N-doped carbon shell coated CoP nanocrystals encapsulated in porous N-doped carbon substrate as efficient electrocatalyst of water splitting. *Carbon* **144**, 464-471 (2019).
- 65 Wei, P. *et al.* Construction of an N-decorated carbon-encapsulated W<sub>2</sub>C/WP heterostructure as an efficient electrocatalyst for hydrogen evolution in both alkaline and acidic media. *ACS Applied Materials & Interfaces* **13**, 53955-53964 (2021).
- 66 Zhang, X. *et al.* Double metal-organic frameworks derived Fe-Co-Ni phosphides nanosheets as high-performance electrocatalyst for alkaline electrochemical water splitting. *Electrochimica Acta* **367**, 137536 (2021).
- 67 Wang, C. *et al.* Alternative synthesis of cobalt monophosphide@C core-shell nanocables for electrochemical hydrogen production. *Journal of Power Sources* **286**, 464-469 (2015).
- 68 Xie, Y. *et al.* Hollow cobalt phosphide with N-doped carbon skeleton as bifunctional electrocatalyst for overall water splitting. *Inorganic Chemistry* **58**, 14652-14659 (2019).
- 69 Pan, Y. *et al.* Nickel phosphide nanoparticles-nitrogen-doped graphene hybrid as an efficient catalyst for enhanced hydrogen evolution activity. *Journal of Power Sources* **297**, 45-52 (2015).
- 70 He, P. *et al.* Carbon-incorporated nickel-cobalt mixed metal phosphide nanoboxes with enhanced electrocatalytic activity for oxygen evolution. *Angewandte Chemie International Edition* **56**, 3897-3900 (2017).
- 71 Huang, H. *et al.* Strongly coupled architectures of cobalt phosphide nanoparticles assembled on graphene as bifunctional electrocatalysts for water splitting. *ChemElectroChem* **3**, 719-725 (2016).
- 72 Zhai, M. *et al.* Transition-metal phosphide-carbon nanosheet composites derived from two-dimensional metal-organic frameworks for highly efficient electrocatalytic water-splitting. *ACS Applied Materials & Interfaces* **9**, 40171-40179 (2017).
- 73 Ding, Z. *et al.* Prussian blue analogue derived cobalt-nickel phosphide/carbon nanotube composite as electrocatalyst for efficient and stable hydrogen evolution reaction in wide-pH environment. *Journal of Colloid and Interface Science* **616**, 210-220 (2022).
- 74 Pu, Z. *et al.* Phytic acid-derivative transition metal phosphides encapsulated in N, P-codoped carbon: an efficient and durable hydrogen evolution electrocatalyst in a wide pH range. *Nanoscale* **9**, 3555-3560 (2017).
- 75 Gao, S. *et al.* General urea-assisted synthesis of carbon-coated metal phosphide nanoparticles for efficient hydrogen evolution electrocatalysis. *Electrochimica Acta* **199**, 99-107 (2016).
- 76 Pan, Y. *et al.* Carbon nanotubes decorated with nickel phosphide nanoparticles as efficient nanohybrid electrocatalysts for the hydrogen evolution reaction. *Journal of Materials Chemistry A* **3**, 13087-13094 (2015).
- 77 Liang, H. *et al.* Cobalt-nickel phosphides@carbon spheres as highly efficient and stable electrocatalyst for hydrogen evolution reaction. *Catalysis Communications* **124**, 1-5 (2019).
- 78 Kang, Q. *et al.* A universal strategy for carbon-supported transition metal phosphides as high-performance bifunctional electrocatalysts towards efficient overall water splitting. *ACS Applied Materials & Interfaces* **12**, 19447-19456 (2020).
- 79 Sun, X. *et al.* Novel transition-metal phosphides@N, P-codoped carbon electrocatalysts synthesized via a universal strategy for overall water splitting. *Journal of Alloys and Compounds* **932**, 167253 (2023).
- 80 Pu, Z. *et al.* Ultrasmall tungsten phosphide nanoparticles embedded in nitrogen-doped carbon as a highly active and stable hydrogen-evolution electrocatalyst. *Journal of Materials Chemistry A* **4**, 15327-15332 (2016).
- 81 Wei, X. *et al.* Carbon-incorporated porous honeycomb NiCoFe phosphide nanospheres derived from a MOF precursor for overall water splitting. *Chemical Communications* **55**, 10896-10899 (2019).



- 82 Deng, J. *et al.* Highly active and durable non-precious-metal catalysts encapsulated in carbon nanotubes for hydrogen evolution reaction. *Energy & Environmental Science* **7**, 1919-1923 (2014).
- 83 Hu, L. *et al.* Synthesis of FeCo nanocrystals encapsulated in nitrogen-doped graphene layers for use as highly efficient catalysts for reduction reactions. *Nanoscale* **7**, 450-454 (2015).
- 84 Zhang, Q. *et al.* Electronically modified atomic sites within a multicomponent Co/Cu composite for efficient oxygen electroreduction. *Advanced Energy Materials* **11**, 2100303 (2021).
- 85 Cao, S. *et al.* CoP microscale prism-like superstructure arrays on Ni foam as an efficient bifunctional electrocatalyst for overall water splitting. *Inorganic Chemistry* **59**, 8522-8531 (2020).
- 86 Wu, T. *et al.* Three-dimensional porous structural MoP<sub>2</sub> nanoparticles as a novel and superior catalyst for electrochemical hydrogen evolution. *Journal of Power Sources* **328**, 551-557 (2016).
- 87 Guan, J. *et al.* Synthesis of transition-metal phosphides from oxidic precursors by reduction in hydrogen plasma. *Journal of Solid State Chemistry* **182**, 1550-1555 (2009).
- 88 Zhu, Y.-P. *et al.* Ultrafine metal phosphide nanocrystals in situ decorated on highly porous heteroatom-doped carbons for active electrocatalytic hydrogen evolution. *ACS Applied Materials & Interfaces* **7**, 28369-28376 (2015).
- 89 Wang, X. *et al.* Chemical and morphological transformation of MOF-derived bimetallic phosphide for efficient oxygen evolution. *Nano Energy* **62**, 745-753 (2019).
- 90 Vittal, J. J. *et al.* Chemistry of metal thio- and selenocarboxylates: precursors for metal sulfide/selenide materials, thin films, and nanocrystals. *Accounts of Chemical Research* **39**, 869-877 (2006).
- 91 Malik, M. A. *et al.* Precursor chemistry for main group elements in semiconducting materials. *Chemical Reviews* **110**, 4417-4446 (2010).
- 92 Gautam, U. K. *et al.* Generation of onions and nanotubes of GaS and GaSe through laser and thermally induced exfoliation. *Journal of the American Chemical Society* **127**, 3658-3659 (2005).
- 93 Shen, G. *et al.* Vapor–solid growth of one-dimensional layer-structured gallium sulfide nanostructures. *ACS Nano* **3**, 1115-1120 (2009).
- 94 Thirumaran, S. in *Nanomaterials via Single-Source Precursors*. 107-121 (Elsevier, 2022).
- 95 Peng, Y. *et al.* Electrocatalysts based on metal@carbon core@shell nanocomposites: An overview. *Green Energy & Environment* **3**, 335-351 (2018).
- 96 Pavlenko, V. *et al.* A comprehensive review of template-assisted porous carbons: Modern preparation methods and advanced applications. *Materials Science and Engineering: R: Reports* **149**, 100682 (2022).
- 97 Tian, P. *et al.* In situ template reaction method to prepare three-dimensional interconnected Fe-N doped hierarchical porous carbon for efficient oxygen reduction reaction catalysts and high performance supercapacitors. *Journal of Power Sources* **448**, 227443 (2020).
- 98 Ge, D. *et al.* Metal-Organic Framework-Derived Atomically Dispersed Co-NC Electrocatalyst for Efficient Oxygen Reduction Reaction. *Catalysts* **12**, 1462 (2022).
- 99 Mohanty, B. *et al.* MoS<sub>2</sub> Quantum Dots as Efficient Electrocatalyst for Hydrogen Evolution Reaction over a Wide pH Range. *Energy & Fuels* **34**, 10268-10275 (2020).
- 100 Xu, Z. *et al.* Effect of particle size on the activity and durability of the Pt/C electrocatalyst for proton exchange membrane fuel cells. *Applied Catalysis B: Environmental* **111**, 264-270 (2012).
- 101 Wang, C. *et al.* Monodisperse Pt<sub>3</sub>Co nanoparticles as electrocatalyst: the effects of particle size and pretreatment on electrocatalytic reduction of oxygen. *Physical Chemistry Chemical Physics* **12**, 6933-6939 (2010).
- 102 Huang, L. *et al.* Phosphorus-bridged ternary metal alloy encapsulated in few-layered nitrogen-doped graphene for highly efficient electrocatalytic hydrogen evolution. *Journal of Materials Chemistry A* **10**, 7111-7121 (2022).
- 103 Nairan, A. *et al.* NiMo solid solution nanowire array electrodes for highly efficient hydrogen evolution reaction. *Advanced Functional Materials* **29**, 1903747 (2019).
- 104 Cai, J. *et al.* MoS<sub>2</sub>||CoP heterostructure loaded on N, P-doped carbon as an efficient

- trifunctional catalyst for oxygen reduction, oxygen evolution, and hydrogen evolution reaction. *International Journal of Hydrogen Energy* **46**, 34252-34263 (2021).
- 105 Liu, T. *et al.* Earthworm-like N, S-Doped carbon tube-encapsulated Co<sub>9</sub>S<sub>8</sub> nanocomposites derived from nanoscaled metal–organic frameworks for highly efficient bifunctional oxygen catalysis. *Journal of Materials Chemistry A* **6**, 5935-5943 (2018).
- 106 Chen, Y. N. *et al.* Carbon-based substrates for highly dispersed nanoparticle and even single-atom electrocatalysts. *Small Methods* **3**, 1900050 (2019).
- 107 Shen, L. *et al.* Confinement Effects in Individual Carbon Encapsulated Nonprecious Metal-Based Electrocatalysts. *Advanced Functional Materials* **32**, 2110851 (2022).
- 108 Yasin, G. *et al.* Tailoring of electrocatalyst interactions at interfacial level to benchmark the oxygen reduction reaction. *Coordination Chemistry Reviews* **469**, 214669 (2022).
- 109 Guo, W. *et al.* The strain effect on the electronic properties of the MoSSe/WSSe van der Waals heterostructure: a first-principles study. *Physical Chemistry Chemical Physics* **22**, 4946-4956 (2020).
- 110 Huang, Y. *et al.* Heterojunction architecture of N-doped WO<sub>3</sub> nanobundles with Ce<sub>2</sub>S<sub>3</sub> nanodots hybridized on a carbon textile enables a highly efficient flexible photocatalyst. *Advanced Functional Materials* **29**, 1903490 (2019).
- 111 Fan, L. *et al.* Green coating by coordination of tannic acid and iron ions for antioxidant nanofiltration membranes. *RSC Advances* **5**, 107777-107784 (2015).
- 112 Lee, Y. A. *et al.* Mussel-inspired surface functionalization of porous carbon nanosheets using polydopamine and Fe<sup>3+</sup>/tannic acid layers for high-performance electrochemical capacitors. *Journal of Materials Chemistry A* **5**, 25368-25377 (2017).
- 113 Fan, H. *et al.* Tannic acid-based multifunctional hydrogels with facile adjustable adhesion and cohesion contributed by polyphenol supramolecular chemistry. *ACS omega* **2**, 6668-6676 (2017).
- 114 Hegab, H. M. *et al.* Single-step assembly of multifunctional poly (tannic acid)–graphene oxide coating to reduce biofouling of forward osmosis membranes. *ACS applied materials & interfaces* **8**, 17519-17528 (2016).
- 115 Liu, G. *et al.* Preparation of ultrathin, robust membranes through reactive layer-by-layer (LbL) assembly for pervaporation dehydration. *Journal of Membrane Science* **537**, 229-238 (2017).
- 116 Erdem, P. *et al.* Preparation and characterization of tannic acid resin: study of boron adsorption. *Environmental Progress & Sustainable Energy* **32**, 1036-1044 (2013).
- 117 Zaaeri, F. *et al.* pH-responsive polymer in a core–shell magnetic structure as an efficient carrier for delivery of doxorubicin to tumor cells. *International Journal of Polymeric Materials and Polymeric Biomaterials* **67**, 967-977 (2017).
- 118 Lim, M.-Y. *et al.* Cross-linked graphene oxide membrane having high ion selectivity and antibacterial activity prepared using tannic acid-functionalized graphene oxide and polyethyleneimine. *Journal of Membrane Science* **521**, 1-9 (2017).
- 119 Kutteri, D. A. *et al.* Methane decomposition to tip and base grown carbon nanotubes and CO<sub>x</sub>-free H<sub>2</sub> over mono-and bimetallic 3d transition metal catalysts. *Catalysis Science & Technology* **8**, 858-869 (2018).
- 120 Ren, J.-T. *et al.* FeNi Nanoalloys Encapsulated in N-Doped CNTs Tangled with N-Doped Carbon Nanosheets as Efficient Multifunctional Catalysts for Overall Water Splitting and Rechargeable Zn–Air Batteries. *ACS Sustainable Chemistry & Engineering* **8**, 223-237 (2019).
- 121 Fan, W. *et al.* Binary Fe, Cu-doped bamboo-like carbon nanotubes as efficient catalyst for the oxygen reduction reaction. *Nano energy* **37**, 187-194 (2017).
- 122 Yang, F. *et al.* Chirality pure carbon nanotubes: Growth, sorting, and characterization. *Chemical Reviews* **120**, 2693-2758 (2020).
- 123 Jia, Y. *et al.* Defect graphene as a trifunctional catalyst for electrochemical reactions. *Advanced materials* **28**, 9532-9538 (2016).
- 124 Ismagilov, Z. R. *et al.* Structure and electrical conductivity of nitrogen-doped carbon nanofibers. *Carbon* **47**, 1922-1929 (2009).

- 125 Lee, A. Y. *et al.* Raman study of D\* band in graphene oxide and its correlation with reduction. *Applied surface science* **536**, 147990 (2021).
- 126 Yang, J. *et al.* Novel iron/cobalt-containing polypyrrole hydrogel-derived trifunctional electrocatalyst for self-powered overall water splitting. *Advanced Functional Materials* **27**, 1606497 (2017).
- 127 Wang, Z. *et al.* FeNi alloys encapsulated in N-doped CNTs-tangled porous carbon fibers as highly efficient and durable bifunctional oxygen electrocatalyst for rechargeable zinc-air battery. *Applied Catalysis B: Environmental* **263**, 118344 (2020).
- 128 Li, M. *et al.* A novel flower-like architecture of FeCo@NC-functionalized ultra-thin carbon nanosheets as a highly efficient 3D bifunctional electrocatalyst for full water splitting. *Journal of Materials Chemistry A* **5**, 5413-5425 (2017).
- 129 Yang, L. *et al.* Electrospun MOF-based FeCo nanoparticles embedded in nitrogen-doped mesoporous carbon nanofibers as an efficient bifunctional catalyst for oxygen reduction and oxygen evolution reactions in zinc-air batteries. *ACS Sustainable Chemistry & Engineering* **7**, 5462-5475 (2019).
- 130 Zhang, Y. *et al.* FeNi alloy nanoparticles embedded in electrospun nitrogen-doped carbon fibers for efficient oxygen evolution reaction. *Journal of Colloid and Interface Science* **578**, 805-813 (2020).
- 131 Yang, L. *et al.* Biomass-derived FeNi alloy and nitrogen-codoped porous carbons as highly efficient oxygen reduction and evolution bifunctional electrocatalysts for rechargeable Zn-air battery. *Energy Storage Materials* **12**, 277-283 (2018).
- 132 Tu, Y. *et al.* Structural and electronic optimization of graphene encapsulating binary metal for highly efficient water oxidation. *Nano Energy* **52**, 494-500 (2018).
- 133 Li, G.-L. *et al.* Micelle-template synthesis of a 3D porous FeNi alloy and nitrogen-codoped carbon material as a bifunctional oxygen electrocatalyst. *Electrochimica Acta* **331**, 135375 (2020).
- 134 Zhang, X. *et al.* FeNi cubic cage@N-doped carbon coupled with N-doped graphene toward efficient electrochemical water oxidation. *ACS Sustainable Chemistry & Engineering* **6**, 8266-8273 (2018).
- 135 Zhang, X. *et al.* FeNi nanoparticles embedded porous nitrogen-doped nanocarbon as efficient electrocatalyst for oxygen evolution reaction. *Electrochimica Acta* **321**, 134720 (2019).
- 136 Gao, Y. *et al.* Template-free synthesis of biomass-derived hierarchically mesoporous carbon with ultra-small FeNi nanoparticles for oxygen evolution reaction. *International Journal of Hydrogen Energy* **44**, 27806-27815 (2019).
- 137 Ren, J.-T. *et al.* Binary FeNi phosphides dispersed on N, P-doped carbon nanosheets for highly efficient overall water splitting and rechargeable Zn-air batteries. *Chemical Engineering Journal* **389**, 124408 (2020).
- 138 Lu, M. *et al.* Trimetallic Nanoparticles Encapsulated into Bamboo-Like N-Doped Carbon Nanotubes as a Robust Catalyst for Efficient Oxygen Evolution Electrocatalysis. *ChemNanoMat* **6**, 1496-1501 (2020).
- 139 Li, D. *et al.* A review on advanced FeNi-based catalysts for water splitting reaction. *Energy & Fuels* **34**, 13491-13522 (2020).
- 140 Gu, X. *et al.* Surface structure regulation and evaluation of FeNi-based nanoparticles for oxygen evolution reaction. *Applied Catalysis B: Environmental* **297**, 120462 (2021).
- 141 Guo, P. *et al.* Multifunctional bayberry-like composites consisting of CoFe encapsulated by carbon nanotubes for overall water splitting and zinc-air batteries. *Journal of Materials Chemistry A* **9**, 21741-21749 (2021).
- 142 Lv, Y. *et al.* Nanofiltration membranes via co-deposition of polydopamine/polyethylenimine followed by cross-linking. *Journal of Membrane Science* **476**, 50-58 (2015).
- 143 Zeng, X. *et al.* Fabrication of superhydrophilic PVDF membranes by one-step modification with eco-friendly phytic acid and polyethyleneimine complex for oil-in-water emulsions separation. *Chemosphere* **264**, 128395 (2021).

- 144 Li, S. *et al.* Layer-by-layer self-assembly of organic-inorganic hybrid intumescent flame retardant on cotton fabrics. *Fibers and Polymers* **20**, 538-544 (2019).
- 145 Xiao, Y. *et al.* Self-Foaming Metal-Organic Gels Based on Phytic Acid and Their Mechanical, Moldable, and Load-Bearing Properties. *Chemistry—A European Journal* **27**, 8791-8798 (2021).
- 146 Zhang, H. *et al.* Effective Dual Polysulfide Rejection by a Tannic Acid/Fe(III) Complex-Coated Separator in Lithium-Sulfur Batteries. *ACS Appl Mater Interfaces* **10**, 12708-12715 (2018).
- 147 Wang, L. *et al.* Phase-Modulation of Iron/Nickel Phosphides Nanocrystals “Armored” with Porous P-Doped Carbon and Anchored on P-Doped Graphene Nanohybrids for Enhanced Overall Water Splitting. *Advanced Functional Materials* **31**, 2010912 (2021).
- 148 Kwong, W. L. *et al.* Scalable two-step synthesis of nickel-iron phosphide electrodes for stable and efficient electrocatalytic hydrogen evolution. *The Journal of Physical Chemistry C* **121**, 284-292 (2017).
- 149 Chen, C. *et al.* Tuning morphology, defects and functional group types in hard carbon via phosphorus doped for rapid sodium storage. *Carbon* **183**, 415-427 (2021).
- 150 Ma, X. *et al.* Phosphorus and nitrogen dual-doped few-layered porous graphene: a high-performance anode material for lithium-ion batteries. *ACS Applied Materials & Interfaces* **6**, 14415-14422 (2014).
- 151 Claramunt, S. *et al.* The importance of interbands on the interpretation of the Raman spectrum of graphene oxide. *The Journal of Physical Chemistry C* **119**, 10123-10129 (2015).
- 152 López-Díaz, D. *et al.* Evolution of the Raman spectrum with the chemical composition of graphene oxide. *The Journal of Physical Chemistry C* **121**, 20489-20497 (2017).
- 153 Wang, Y. *et al.* Effect of Pr addition on the properties of Ni/Al<sub>2</sub>O<sub>3</sub> catalysts with an application in the autothermal reforming of methane. *International Journal of Hydrogen Energy* **39**, 778-787 (2014).
- 154 Amin, A. M. *et al.* Review of methane catalytic cracking for hydrogen production. *International Journal of Hydrogen Energy* **36**, 2904-2935 (2011).
- 155 Homma, Y. *et al.* Role of transition metal catalysts in single-walled carbon nanotube growth in chemical vapor deposition. *The Journal of Physical Chemistry B* **107**, 12161-12164 (2003).
- 156 Long, X. *et al.* Graphitic phosphorus coordinated single Fe atoms for hydrogenative transformations. *Nature Communications* **11**, 1-12 (2020).
- 157 Seo, B. *et al.* Shape effects of nickel phosphide nanocrystals on hydrogen evolution reaction. *CrystEngComm* **18**, 6083-6089 (2016).
- 158 Yang, J. *et al.* Novel Fe<sub>2</sub>P/graphitized carbon yolk/shell octahedra for high-efficiency hydrogen production and lithium storage. *Journal of Materials Chemistry A* **4**, 9923-9930 (2016).
- 159 Chen, W. *et al.* FeNiP nanoparticle/N, P dual-doped carbon composite as a trifunctional catalyst towards high-performance zinc-air batteries and overall water electrolysis. *Nanoscale* **13**, 17136-17146 (2021).
- 160 Guo, J. *et al.* Self-Supported FeNiP Nanosheet Arrays as a Robust Bifunctional Electrocatalyst for Water Splitting. *ACS Applied Energy Materials* (2022).
- 161 Mo, R. *et al.* Graphene layers-wrapped FeNiP nanoparticles embedded in nitrogen-doped carbon nanofiber as an active and durable electrocatalyst for oxygen evolution reaction. *Electrochimica Acta* **290**, 649-656 (2018).
- 162 Chen, W. *et al.* Heteroatom-doped carbon materials: synthesis, mechanism, and application for sodium-ion batteries. *Small Methods* **3**, 1800323 (2019).
- 163 Du, Y. *et al.* N-doped carbon coated FeNiP nanoparticles based hollow microboxes for overall water splitting in alkaline medium. *International Journal of Hydrogen Energy* **43**, 22226-22234 (2018).
- 164 Xu, Y. *et al.* Facile preparation of self-assembled Ni/Co phosphates composite spheres with highly efficient HER electrocatalytic performances. *Applied Surface Science* **509**, 145383 (2020).
- 165 Shin, H. J. *et al.* Highly active and stable electrocatalytic transition metal phosphides (Ni<sub>2</sub>P and FeP) nanoparticles on porous carbon cloth for overall water splitting at high current density. *International Journal of Energy Research* **44**, 11894-11907 (2020).

- 166 Chen, Z. *et al.* N, P-co-doped carbon coupled with CoP as superior electrocatalysts for hydrogen evolution reaction and overall water splitting. *International Journal of Hydrogen Energy* **44**, 24342-24352 (2019).
- 167 Li, W. *et al.* 3D hollow Co–Fe–P nanoframes immobilized on N, P-doped CNT as an efficient electrocatalyst for overall water splitting. *Nanoscale* **11**, 17031-17040 (2019).
- 168 Sheng, Q. *et al.* Understanding the Reduction of Transition-Metal Phosphates to Transition-Metal Phosphides by Combining Temperature-Programmed Reduction and Infrared Spectroscopy. *Angew Chem Int Ed Engl* **60**, 11180-11183 (2021).
- 169 Sun, M. *et al.* Earth-rich transition metal phosphide for energy conversion and storage. *Advanced Energy Materials* **6**, 1600087 (2016).
- 170 Berhault, G. *et al.* In situ XRD, XAS, and magnetic susceptibility study of the reduction of ammonium nickel phosphate  $\text{NiNH}_4\text{PO}_4 \cdot \text{H}_2\text{O}$  into nickel phosphide. *Inorganic Chemistry* **48**, 2985-2992 (2009).
- 171 Li, Y. *et al.*  $\text{MoS}_2$  nanoparticles grown on graphene: an advanced catalyst for the hydrogen evolution reaction. *Journal of the American Chemical Society* **133**, 7296-7299 (2011).
- 172 Lu, J. *et al.* Carbon-encapsulated electrocatalysts for the hydrogen evolution reaction. *Electrochemical Energy Reviews* **2**, 105-127 (2019).
- 173 Hu, Q. *et al.* Recent progress in the hybrids of transition metals/carbon for electrochemical water splitting. *Journal of Materials Chemistry A* **7**, 14380-14390 (2019).
- 174 Wang, M. *et al.* Metal–organic framework derived carbon-confined  $\text{Ni}_2\text{P}$  nanocrystals supported on graphene for an efficient oxygen evolution reaction. *Chemical Communications* **53**, 8372-8375 (2017).
- 175 Wang, H. *et al.* Self-assembled  $\text{Ni}_2\text{P}/\text{FeP}$  heterostructural nanoparticles embedded in N-doped graphene nanosheets as highly efficient and stable multifunctional electrocatalyst for water splitting. *Electrochimica Acta* **318**, 449-459 (2019).
- 176 Yang, Q. *et al.*  $\text{FeNi}_3/\text{Ni}_2\text{P}$  heterojunction encapsulated in N-doped carbon nanotubes as an effective electrocatalyst for oxygen evolution reaction. *International Journal of Hydrogen Energy* **46**, 39736-39742 (2021).
- 177 Pu, Z. *et al.* General strategy for the synthesis of transition-metal phosphide/N-doped carbon frameworks for hydrogen and oxygen evolution. *ACS Applied Materials & Interfaces* **9**, 16187-16193 (2017).
- 178 Streckova, M. *et al.* Nanoarchitectonics of binary transition metal phosphides embedded in carbon fibers as a bifunctional electrocatalysts for electrolytic water splitting. *Journal of Alloys and Compounds* **923**, 166472 (2022).
- 179 Sun, X. *et al.* Novel transition-metal phosphides@N, P-codoped carbon electrocatalysts synthesized via a universal strategy for overall water splitting. *Journal of Alloys and Compounds*, 167253 (2022).
- 180 Jin, L. *et al.* General method for synthesizing transition-metal phosphide/N-doped carbon nanomaterials for hydrogen evolution. *Langmuir* **35**, 9161-9168 (2019).
- 181 Fan, X. *et al.* Covalent porphyrin framework-derived  $\text{Fe}_2\text{P}@/\text{Fe}_4\text{N}$ -coupled nanoparticles embedded in N-doped carbons as efficient trifunctional electrocatalysts. *ACS Applied Materials & Interfaces* **9**, 32840-32850 (2017).
- 182 Zhang, R. *et al.* FeP embedded in N, P dual-doped porous carbon nanosheets: an efficient and durable bifunctional catalyst for oxygen reduction and evolution reactions. *Journal of Materials Chemistry A* **4**, 18723-18729 (2016).
- 183 Tong, J. *et al.* Porous Nitrogen Self-Doped Carbon Wrapped Iron Phosphide Hollow Spheres as Efficient Bifunctional Electrocatalysts for Water Splitting. *ChemElectroChem* **6**, 3437-3444 (2019).
- 184 Gong, Y. *et al.* Confinement of transition metal phosphides in N, P-doped electrospun carbon fibers for enhanced electrocatalytic hydrogen evolution. *Journal of Alloys and Compounds* **875**, 159934 (2021).
- 185 Sierra-Trejo, P. V. *et al.* Arsenic Sorption on Chitosan-Based Sorbents: Comparison of the Effect

- of Molybdate and Tungstate Loading on As(V) Sorption Properties. *Journal of Polymers and the Environment* **28**, 934-947 (2020).
- 186 Advani, J. H. *et al.* Chitosan supported molybdate nanoclusters as an efficient catalyst for oxidation of alkenes and alcohols. *Cellulose* **27**, 8769-8783 (2020).
- 187 Wang, C. *et al.* Formation of Mo-Polydopamine Hollow Spheres and Their Conversions to MoO<sub>2</sub>/C and Mo<sub>2</sub>C/C for Efficient Electrochemical Energy Storage and Catalyst. *Small* **13** (2017).
- 188 Wichard, T. *et al.* Storage and bioavailability of molybdenum in soils increased by organic matter complexation. *Nature Geoscience* **2**, 625-629 (2009).
- 189 Yoo, S. *et al.* Ammonia Gas Detection by Tannic Acid Functionalized and Reduced Graphene Oxide at Room Temperature. *Journal of Nanomaterials* **2014**, 1-6 (2014).
- 190 Lin, H. *et al.* Enhanced thermal conductivity of PLA-based nanocomposites by incorporation of graphite nanoplatelets functionalized by tannic acid. *Journal of Applied Polymer Science* **135** (2018).
- 191 Jin, Y.-N. *et al.* Underwater superoleophobic coatings fabricated from tannic acid-decorated carbon nanotubes. *RSC Advances* **5**, 16112-16115 (2015).
- 192 Chen, Y. *et al.* Single-Source-Precursor Derived Transition Metal Alloys Embedded in Nitrogen-doped Porous Carbons as Efficient Oxygen Evolution Electrocatalysts. *ChemPlusChem* (2022).
- 193 Huang, Q. *et al.* Preparation of polyethylene polyamine@tannic acid encapsulated MgAl-layered double hydroxide for the efficient removal of copper (II) ions from aqueous solution. *Journal of the Taiwan Institute of Chemical Engineers* **82**, 92-101 (2018).
- 194 Xu, G. *et al.* Tannic acid anchored layer-by-layer covalent deposition of parasin I peptide for antifouling and antimicrobial coatings. *RSC Advances* **6**, 14809-14818 (2016).
- 195 Zhang, T. *et al.* A phosphorus-, nitrogen-and carbon-containing polyelectrolyte complex: preparation, characterization and its flame retardant performance on polypropylene. *RSC Advances* **4**, 48285-48292 (2014).
- 196 Wang, P.-J. *et al.* Facile fabrication of biobased PNC-containing nano-layered hybrid: Preparation, growth mechanism and its efficient fire retardancy in epoxy. *Polymer Degradation and Stability* **159**, 153-162 (2019).
- 197 Andriopoulou, C. *et al.* Tuning the configuration of dispersed oxometallic sites in supported transition metal oxide catalysts: A temperature dependent Raman study. *Catalysis Today* **336**, 74-83 (2019).
- 198 Li, G. *et al.* Carbon-tailored semimetal MoP as an efficient hydrogen evolution electrocatalyst in both alkaline and acid media. *Advanced Energy Materials* **8**, 1801258 (2018).
- 199 Burns, S. *et al.* On the use of methane as a reductant in the synthesis of transition metal phosphides. *Catalysis Communications* **8**, 931-935 (2007).
- 200 Xu, Y. *et al.* Nanostructures Ni<sub>2</sub>P/MoP@N-doping porous carbon for efficient hydrogen evolution over a broad pH range. *Electrochimica Acta* **363**, 137151 (2020).
- 201 Nguyen, C. *et al.* Efficient and stable hybrid electrocatalyst of mixed MnP-MoP nanoparticles-N, P-codoped graphene for hydrogen evolution reaction. *Colloids and Surfaces A: Physicochemical and Engineering Aspects* **593**, 124609 (2020).
- 202 Yang, W. *et al.* Hierarchical MoP Hollow Nanospheres Anchored on a N, P, S-Doped Porous Carbon Matrix as Efficient Electrocatalysts for the Hydrogen Evolution Reaction. *ChemSusChem* **12**, 4662-4670 (2019).
- 203 Song, H. *et al.* Designed controllable nitrogen-doped carbon-dots-loaded MoP nanoparticles for boosting hydrogen evolution reaction in alkaline medium. *Nano Energy* **72**, 104730 (2020).
- 204 Yang, L. *et al.* Co-N-doped MoO<sub>2</sub> nanowires as efficient electrocatalysts for the oxygen reduction reaction and hydrogen evolution reaction. *Nano Energy* **41**, 772-779 (2017).
- 205 Dutta, S. *et al.* An Intriguing Pea-Like Nanostructure of Cobalt Phosphide on Molybdenum Carbide Incorporated Nitrogen-Doped Carbon Nanosheets for Efficient Electrochemical Water Splitting. *ChemSusChem* **11**, 3956-3964 (2018).
- 206 Li, X. *et al.* Crystalline MoP-amorphous MoS<sub>2</sub> hybrid for superior hydrogen evolution reaction. *Journal of Solid State Chemistry* **290**, 121564 (2020).

- 207 Tian, Q. *et al.* Design of charge transfer channels: defective TiO<sub>2</sub>/MoP supported on carbon cloth for solar-light-driven hydrogen generation. *Inorganic Chemistry Frontiers* **8**, 2017-2026 (2021).
- 208 Jaiswal, A. *et al.* Iron/Iron carbide (Fe/Fe<sub>3</sub>C) encapsulated in S, N codoped graphitic carbon as a robust HER electrocatalyst. *Energy & Fuels* **35**, 16046-16053 (2021).
- 209 Liu, Z. *et al.* Manganese Oxide/Iron Carbide Encapsulated in Nitrogen and Boron Codoped Carbon Nanowire Networks as Accelerated Alkaline Hydrogen Evolution and Oxygen Reduction Bifunctional Electrocatalysts. *ACS Applied Materials & Interfaces* **14**, 13280-13294 (2022).
- 210 Li, S. *et al.* Binary Metal Phosphides with MoP and FeP Embedded in P,N-Doped Graphitic Carbon As Electrocatalysts for Oxygen Reduction. *ACS Sustainable Chemistry & Engineering* **7**, 11872-11884 (2019).
- 211 Li, J. *et al.* Template-free fabrication of MoP nanoparticles encapsulated in N-doped hollow carbon spheres for efficient alkaline hydrogen evolution. *Chemical Engineering Journal* **416**, 127677 (2021).
- 212 Yang, J. *et al.* Functional mesoporous poly (ionic liquid) s-derived ultrafine MoP modified N, P-codoped carbon for stable hydrogen production in alkaline media. *Journal of Alloys and Compounds* **929**, 167254 (2022).
- 213 Rawal, S. *et al.* Synthesis and electrochemical study of phosphorus-doped porous carbon for supercapacitor applications. *SN Applied Sciences* **3** (2021).
- 214 Yun, W. H. *et al.* Ni-Fe phosphide deposited carbon felt as free-standing bifunctional catalyst electrode for urea electrolysis. *Scientific Reports* **11**, 1-10 (2021).
- 215 Deng, Y. *et al.* Hierarchically open-porous carbon networks enriched with exclusive Fe-N<sub>x</sub> active sites as efficient oxygen reduction catalysts towards acidic H<sub>2</sub>-O<sub>2</sub> PEM fuel cell and alkaline Zn-air battery. *Chemical Engineering Journal* **390**, 124479 (2020).
- 216 Li, J. *et al.* Highly N,P-doped carbon dots: Rational design, photoluminescence and cellular imaging. *Microchimica Acta* **184**, 2933-2940 (2017).
- 217 Wang, H. *et al.* Fluorescently tuned nitrogen-doped carbon dots from carbon source with different content of carboxyl groups. *APL Materials* **3** (2015).
- 218 Chiang, C. *et al.* in *Fillers and Reinforcements for Advanced Nanocomposites*. 253-272 (Elsevier, 2015).
- 219 Biesinger, M. C. Accessing the robustness of adventitious carbon for charge referencing (correction) purposes in XPS analysis: Insights from a multi-user facility data review. *Applied Surface Science* **597**, 153681 (2022).
- 220 Choi, C. H. *et al.* Phosphorus-nitrogen dual doped carbon as an effective catalyst for oxygen reduction reaction in acidic media: effects of the amount of P-doping on the physical and electrochemical properties of carbon. *Journal of Materials Chemistry* **22**, 12107-12115 (2012).
- 221 Niu, H.-J. *et al.* Assembled hollow spheres with CoFe alloyed nanocrystals encapsulated in N, P-doped carbon nanovesicles: An ultra-stable bifunctional oxygen catalyst for rechargeable Zn-air battery. *Journal of Power Sources* **475**, 228594 (2020).
- 222 Yu, B. *et al.* MoP QDs@graphene as highly efficient electrocatalyst for polysulfide conversion in Li-S batteries. *Journal of Materials Science & Technology* **90**, 37-44 (2021).
- 223 Jiang, Z.-J. *et al.* Co nanoparticles coupling induced high catalytic activity of nitrogen doped carbon towards hydrogen evolution reaction in acidic/alkaline solutions. *Electrochimica Acta* **342**, 136076 (2020).
- 224 Osadchii, D. Y. *et al.* Revisiting Nitrogen Species in Covalent Triazine Frameworks. *Langmuir* **33**, 14278-14285 (2017).
- 225 Ji, W. *et al.* Partially nitrated molybdenum trioxide with promoted performance as an anode material for lithium-ion batteries. *Journal of Materials Chemistry A* **2**, 699-704 (2014).
- 226 Ge, R. *et al.* Hierarchical molybdenum phosphide coupled with carbon as a whole pH-range electrocatalyst for hydrogen evolution reaction. *Applied Catalysis B: Environmental* **260**, 118196 (2020).

- 227 Li, G. *et al.* Cobalt–Cobalt Phosphide Nanoparticles@Nitrogen-Phosphorus Doped Carbon/Graphene Derived from Cobalt Ions Adsorbed Saccharomycete Yeasts as an Efficient, Stable, and Large-Current-Density Electrode for Hydrogen Evolution Reactions. *Advanced Functional Materials* **28**, 1801332 (2018).
- 228 Lv, Z. *et al.* Designed synthesis of WC-based nanocomposites as low-cost, efficient and stable electrocatalysts for the hydrogen evolution reaction. *CrystEngComm* **22**, 4580-4590 (2020).
- 229 Liu, T. *et al.* Recycling valuable cobalt from spent lithium ion batteries for controllably designing a novel sea-urchin-like cobalt nitride-graphene hybrid catalyst: Towards efficient overall water splitting. *Journal of Energy Chemistry* **62**, 440-450 (2021).
- 230 Liang, K. *et al.* S-doped MoP nanoporous layer toward high-efficiency hydrogen evolution in pH-universal electrolyte. *ACS Catalysis* **9**, 651-659 (2018).
- 231 Choudhary, H. K. *et al.* Effect of morphology and role of conductivity of embedded metallic nanoparticles on electromagnetic interference shielding of PVDF-carbonaceous-nanofiller composites. *Carbon* **164**, 357-368 (2020).
- 232 Ding, Y. *et al.* Tuning of Reciprocal Carbon-Electrode Properties for an Optimized Hydrogen Evolution. *ChemSusChem* **14**, 2547-2553 (2021).
- 233 Li, J.-S. *et al.* Confined molybdenum phosphide in P-doped porous carbon as efficient electrocatalysts for hydrogen evolution. *ACS Applied Materials & Interfaces* **10**, 17140-17146 (2018).
- 234 Pi, C. *et al.* In situ formation of N-doped carbon-coated porous MoP nanowires: a highly efficient electrocatalyst for hydrogen evolution reaction in a wide pH range. *Applied Catalysis B: Environmental* **263**, 118358 (2020).
- 235 Li, J.-S. *et al.* Highly efficient hydrogen evolution electrocatalysts based on coupled molybdenum phosphide and reduced graphene oxide derived from MOFs. *Chemical Communications* **53**, 12576-12579 (2017).
- 236 Li, J.-S. *et al.* Reduced graphene oxide-supported MoP@P-doped porous carbon nano-octahedrons as high-performance electrocatalysts for hydrogen evolution. *ACS Sustainable Chemistry & Engineering* **6**, 10252-10259 (2018).
- 237 Chen, N. *et al.* Heterostructured MoC-MoP/N-doped carbon nanofibers as efficient electrocatalysts for hydrogen evolution reaction. *Electrochimica Acta* **299**, 708-716 (2019).
- 238 Li, J.-S. *et al.* Pomegranate-like molybdenum phosphide@phosphorus-doped carbon nanospheres coupled with carbon nanotubes for efficient hydrogen evolution reaction. *Carbon* **139**, 234-240 (2018).
- 239 Chi, J.-Q. *et al.* Nitrogen, phosphorus dual-doped molybdenum-carbide/molybdenum-phosphide-@-carbon nanospheres for efficient hydrogen evolution over the whole pH range. *Journal of Colloid and Interface Science* **513**, 151-160 (2018).
- 240 Liu, T. *et al.* Molybdenum carbide/phosphide hybrid nanoparticles embedded P, N co-doped carbon nanofibers for highly efficient hydrogen production in acidic, alkaline solution and seawater. *Electrochimica Acta* **281**, 710-716 (2018).
- 241 Wang, C. *et al.* Open N-doped carbon coated porous molybdenum phosphide nanorods for synergistic catalytic hydrogen evolution reaction. *Nano Research* **15**, 1824-1830 (2022).
- 242 Wang, D. *et al.* Hydrogen evolution catalyzed by cobalt-promoted molybdenum phosphide nanoparticles. *Catalysis Science & Technology* **6**, 1952-1956 (2016).
- 243 Cui, W. *et al.* MoP nanosheets supported on biomass-derived carbon flake: One-step facile preparation and application as a novel high-active electrocatalyst toward hydrogen evolution reaction. *Applied Catalysis B: Environmental* **164**, 144-150 (2015).



---

---

## Curriculum Vitae

---

### PERSONAL DATA

---

Name	Yongchao Chen
Date of Birth	20.11.1992
Nationality	China

### EDUCATION

---

11/2019–07/2023	Ph.D. Candidate in Materials Science <b>Technical University of Darmstadt</b> , Darmstadt, Germany
09/2016–01/2019	M.Sc. in Chemical Engineering <b>Northeastern University</b> , Shenyang, China
09/2012–06/2016	B. Eng. in Chemical Engineering <b>Shenyang University of Chemical Technology</b> , Shenyang, China

### RESEARCH EXPERIENCE

---

Since 01/2021	Research Project: <i>Single-source-precursor approach derived transition metal compounds-carbon hybrids for electrochemical applications</i>
11/2019–11/2020	Research Project: <i>Polymer-derived silica-based nanomaterial with selective catalytic reduction properties for denitrification</i>
09/2017–01/2019	Research Project: <i>Research on kaolinite transformation under calcification-carbonation process</i>
09/2015–05/2016	Research Project: <i>The effect of anions based on 1-Butyl-3-methylimidazole for the separation of methanol-ethyl acetate azeotropic mixture</i>



---

---

## Publications

---

### Statement of personal contribution

The personal contribution of the author himself to the following research articles is listed.

**Chen, Y.**, Tian, C., Jiang, T., Maheu, C., Hofmann, J. P., Molina-Luna, L., Riedel, R. & Yu, Z. Single-Source-Precursor Derived Transition Metal Alloys Embedded in Nitrogen-Doped Porous Carbons as Efficient Oxygen Evolution Electrocatalysts. *ChemPlusChem* 87, e202200338 (2022). © Wiley

The inception of this publication originated from Yongchao Chen. After brainstorming ideas and refining the research question, he designed the methodology, which was then reviewed and approved by Prof. Ralf Riedel and Prof. Zhaoju Yu. Yongchao Chen carried out the sample preparation and characterizations, including but not limited to the synthesis, pyrolysis, various characterization included in the publication. Meanwhile, Chuanmu Tian and Dr. Clément Maheu conducted the X-ray photoelectron spectroscopy (XPS) characterization. Chuanmu Tian gave the instruction for the electrochemical setups and Tianshu Jiang performed the Transmission electron microscopy (TEM) characterization. Following the data collection and analysis was done by Yongchao Chen and responsible for writing the manuscript. Prof. Jan P. Hofmann and Prof. Leopoldo Molina-Luna gave input and feedback regarding XPS and TEM, respectively. After the review and revision of Prof. Ralf Riedel, Prof. Zhaoju Yu, and Prof. Jan P. Hofmann, the manuscript was ultimately approved by all authors and submitted for publication.

**Chen, Y.**, Jiang, T., Tian, C., Zhan, Y., Kempf, A., Molina-Luna, L., Hofmann, J. P., Riedel, R. & Yu, Z. Single-Source-Precursor Derived Binary FeNi Phosphide Nanoparticles Encapsulated in N, P Co-Doped Carbon as Electrocatalyst for HER and OER. *Energy Technology*, 2300233 (2023). © Wiley

The inception of this publication originated from Yongchao Chen. The designed methodology was then reviewed and approved by Prof. Ralf Riedel and Prof. Zhaoju Yu. Yongchao Chen carried out the sample preparation and characterizations except XPS and TEM. Chuanmu Tian and Tianshu Jiang conducted XPS and TEM characterization, respectively. The data collection and analysis were done by Yongchao Chen and he was responsible for writing the manuscript. The Raman analyses and manuscript were discussed with Alexander Kempf and Dr. Ying Zhan. Prof. Jan P. Hofmann and Prof. Leopoldo Molina-Luna provided input and feedback regarding XPS and TEM, respectively, during the revision process. After the review and revision of Prof. Ralf Riedel, Prof. Zhaoju Yu and Prof. Jan P. Hofmann, the manuscript was ultimately approved by all authors and submitted for publication.

**Chen, Y.**, Jiang, T., Tian, C., Zhan, Y., Adabifiroozjaei, E., Kempf, A., Molina-Luna, L., Hofmann, J. P., Riedel, R. & Yu, Z. Molybdenum Phosphide Quantum Dots Encapsulated by P/N-Doped Carbon for Hydrogen Evolution Reaction in Acid and Alkaline. *ChemSusChem*, e202300479 (2023). © Wiley

The idea behind this publication originated from Yongchao Chen. Then the designed methodology was reviewed and approved by Prof. Ralf Riedel and Prof. Zhaoju Yu. Yongchao Chen carried out the sample preparation and characterizations except XPS and TEM. Chuanmu Tian and Tianshu Jiang conducted XPS and TEM characterization, respectively. The data collection and analysis were performed by Yongchao Chen and he was responsible for writing the manuscript. The manuscript proofreading was provided by Alexander Kempf and Dr. Ying zhan. Prof. Jan P. Hofmann and Prof. Leopoldo Molina-Luna provided input and feedback regarding XPS and TEM, respectively, during writing the manuscript and during the revision process. After the final review and revision of Prof. Ralf Riedel, Prof. Zhaoju Yu and Prof. Jan P. Hofmann, the manuscript was ultimately approved by all authors and submitted for publication. Dr. Adabifiroozjaei Esmail conducted the TEM characterization for the second-round peer review.

### Signature of co-authors

The signatures of the co-authors are listed.

Ralf Riedel		Zhaoju Yu	
Jan P. Hofmann		Leopoldo Molina-Luna	
Tianshu Jiang		Chuanmu Tian	
Ying Zhan		Alexander Kempf	
Clément Maheu		Esmail Adabifiroozjaei	